Combustion aerosols from potassium-containing fuels

Nielsen, Lars Balzer

Publication date:
1998

Document Version
Publisher's PDF, also known as Version of record

Combustion aerosols from potassium-containing fuels

Lars Balzer Nielsen
1998

The Aerosol Laboratory
Department of Chemical Engineering
Technical University of Denmark
DK-2800 Lyngby

Aerosolgruppen
Institut for Kemiteknik
Danmarks Tekniske Universitet
2800 Lyngby

DISCLAIMER

Portions of this document may be illegible in electronic image products. Images are produced from the best available original document.

Preface

This dissertation is a partial fulfillment of the requirements of the Ph.D.-degree. The work has been carried out at the Aerosol Laboratory, Department of Chemical Engineering, Technical University of Denmark with Dr. Hans Livbjerg as supervisor.

This work could not have been completed without the inspiration, guidance, and constructive criticism of Hans Livbjerg throughout the entire period of the Ph.D.-study. I would also like to express my sincere thanks to my colleagues, past and present, Kurt A. Christensen, Tue Johannessen, and Sune K. Andersen, for helpful discussions, comments, and for providing an inspiring and pleasant environment. The invaluable assistance of Karin Petersen is also gratefully acknowledged. Finally, I would like to thank the M.Sc. students Lars S. Jensen, Carsten Pedersen, and Martin Røkke for valuable contributions to the field investigation. The critical reading of the thesis by Lone Brøndsted is also warmly appreciated.

The participants in the field investigation from I/S Midtkraft and the CHEC group at the Department of Chemical Engineering, Technical University of Denmark are acknowledged for letting us be a part of this investigation. The assistance in performing electron microscopy and chemical analyses on the particles by Inger Søndergaard at the Department of Process Technology and Allan Henschel at the Department of Physics is also gratefully acknowledged.

This work has been supported by a grant from the Research Program of the Ministry of Energy (EFP 94).

Lars Balzer Nielsen

Lyngby, Denmark
February 1998

Summary

The scope of the work presented in this thesis is the formation and evolution of aerosol particles in the submicron range during combustion processes, in particular where biomass is used alone or co-fired with coal. An introduction to the formation processes of fly ash in general and submicron aerosol in particular during combustion is presented, along with some known problems related to combustion of biomass for power generation.

The work falls in two parts. The first is the design of a laboratory setup for investigation of homogeneous nucleation and particle dynamics at high temperature. The central unit of the setup is a laminar flow aerosol condenser (LFAC), which essentially is a 173 cm long tubular furnace with an externally cooled wall. Furthermore, the first part of the furnace serves as a saturator, where a carrier gas is saturated with the condensing component. The second part of the LFAC is a condenser where cooling takes place. The cooling causes condensible species in the gas phase to condense on the tube wall, on existing particles, or to form new particles by homogeneous nucleation. The setup has been optimized and characterized with respect to saturation, stabilization time, and cooling rates. The system also enables the addition of a laboratory generated aerosol in order to facilitate studying the influence of seed nuclei on the condensation processes. The effluent aerosol is analyzed using a scanning mobility particle sizer (SMPS) system, which yields the number size distribution in the range from 0.014 to 0.8 μm.

The LFAC has been used to study the formation of submicron aerosol formed when a gas containing from 70 to 240 ppm of KCl is cooled at an average rate from 200 to 600 K/s. Between $3 \cdot 10^6$ and $3 \cdot 10^7$ particles/cm^3 at 20°C are readily formed having geometric mean diameters from 0.1 to 0.35 μm. The number concentration of particles formed depends on the temperature at which homogeneous nucleation takes place. The size of the particles increases with increasing KCl concentration and decreasing cooling rate. The homogeneous nucleation of KCl can be completely suppressed by the addition of a laboratory generated aerosol in a concentration of approximately 10^5 particles/cm^3.

A mathematical model is presented which describes the formation and evolution of the aerosol in the LFAC, where the rate of formation of new nuclei is calculated using the so-called classical theory. The model includes mass and energy conservation equations and an expression for the description of particle growth by diffusion. The resulting set of nonlinear second-order partial differential equations are solved numerically using the method of orthogonal collocation. The model is implemented in the FORTRAN code MONAERO, and the results of the simulations correspond well to the experimental results in the case where no seed nuclei are present. When seed nuclei are present, the simulations and experiments are in reasonable agreement.

The second part of this thesis describes a comprehensive investigation of submicron aerosol formation during co-firing of coal and straw carried out at a 380 MW_{Th} pulverized coal unit at Studstrup Power Plant, Århus. Three types of coal are used, and total boiler load and straw input is varied systematically. Straw contains large amounts of potassium, which is released during combustion. Submicron aerosol is sampled between the two banks of the economizer at a flue gas temperature of 350°C using a novel ejector probe, which dilutes the sample at high temperature. The dilution prevents condensation of water vapor and minimizes particle

coagulation. The aerosol is characterized using the SMPS system and a Berner-type low pressure impactor. The chemical composition of the particles collected in the impactor is determined using chemical analysis and energy-dispersive x-ray analysis (EDX). The morphology of the particles is investigated with electron microscopy.

The flue gas is found to contain between $4 \cdot 10^7$ and $9 \cdot 10^7$ particles/cm^3 at 20°C, and the geometric mean diameter of the particles is from 0.04 to 0.09 μm. The main constituents of the aerosol determined by EDX are the elements Si, Al, Fe, K, Ca, S, and P. The small particles, i.e. with diameters less than 1 μm, are enriched in Ca, S, and P. The concentration of potassium decreases with decreasing particle size, probably as a result of a high-temperature reaction with the Si and Al of the larger particles. No chlorine is found in the particles collected, probably because the KCl present in the gas phase at high temperature is converted to K_2SO_4 by the sulphation reaction. An important conclusion is that the number and mass concentration of submicron aerosol are insignificantly changed by co-firing of straw under the conditions investigated.

Resumé (Summary in Danish)

Emnet for dette arbejde er dannelsen af submikrone aerosolpartikler i forbindelse med forbrændingsprocesser, med særlig vægt på forhold hvor biomasse anvendes som brændsel, alene eller ved samfyring med kul. Der gives en introduktion til dannelsesmekanismerne for flyveaske i forbrændingsprocesser i almindelighed, og den submikrone fraktion i særdeleshed. Der gøres også rede for kendte problemer ved anvendelse af halm som brændsel til energiproduktion.

Det udførte arbejde består af to dele. Den første omhandler design af en laboratorieopstilling til undersøgelse af homogen nukleering og partikeldynamik ved høj temperatur. Systemet består af en såkaldt laminar flow aerosol kondenser (LFAC), som er en 173 cm lang rørovn i hvis første del en bæregas mættes med den komponent der undersøges. Den anden del af ovnen udgør kondensersektionen, hvor der påtrykkes en faldende temperaturprofil på rørvæggen. Denne afkøling medfører en kondensation af den undersøgte komponent, der kan kondensere på rørvæggen, på partikler i gasfasen eller danne nye partikler ved homogen nukleering. Opstillingen er karakteriseret med hensyn til krævede stabiliseringstider, mætningsforhold og afkølingshastighed. Systemet tillader også tilsætning af en laboratorieskabt aerosol, hvorved det er muligt at studere fremmede kims indflydelse på kondensationsprocesserne. Aerosolpartiklerne karakteriseres ved målinger i udgangen ved hjælp af et scanning mobility particle sizer (SMPS) system, som måler partiklernes antals-størrelsesfordeling i intervallet 0.014-0.8 μm.

Opstillingen anvendes til at undersøge dannelsen af en submikron aerosol ved afkøling af KCl-dampe i en koncentration fra 70 til 240 ppm. Den gennemsnitlige afkølingshastighed er mellem 200 og 600 K/s. Der er målt partikelkoncentrationer på mellem $3 \cdot 10^6$ og $3 \cdot 10^7$ partikler/cm^3 ved 20°C med geometrisk middeldiameter fra 0.1 til 0.35 μm. Koncentrationen af submikrone partikler afhænger først og fremmest af den temperatur, ved hvilken den homogene nukleering foregår. Partiklernes størrelse forøges med stigende startkoncentration af KCl i gassen og aftagende afkølingshastighed. Den homogene nukleering af KCl kan undertrykkes fuldstændigt ved tilsætning af fremmede kim i en koncentration på omtrent 10^5 partikler/cm^3.

Der er udviklet en matematisk model som beskriver dannelse og udvikling af aerosolen i forsøgsudstyret, hvor dannelseshastigheden af nye kim er beskrevet ved den såkaldte klassiske teori. Modellen inkluderer ligninger for masse- og energibevarelse, og tillige et udtryk for partikelvækst ved diffusion. Det resulterende sæt af ikke-lineære anden ordens partielle differentialligninger løses ved ortogonal kollokation. Modellen er implementeret i programmet MONAERO. Resultater af simuleringer viser en god overensstemmelse med de målte resultater, når der ikke tilsættes fremmede kim til bæregassen, mens der ved kimtilsætning er en rimelig overensstemmelse mellem beregnede og målte resultater.

Afhandlingens anden del beskriver en omfattende undersøgelse af forbrændingsaerosoler ved samfyring af halm og kul på Studstrupværkets 380 MW_{Th} kulfyrede kedel. I undersøgelsen er der anvendt tre forskellige kultyper, og totallast og halmandel er varieret systematisk. Halm indeholder en stor mængde kalium som frigives under forbrænding. Der er taget prøver mellem to rækker i kedlens economizer-sektion, hvor røggastemperaturen er ca. 350°C. Der er til dette formål designet en ny ejektorprobe, som fortynder gasprøven ved høj temperatur, hvorved problemer med kondensation af røggassens vandindhold og koagulering af partikler undgås.

Aerosolen karakteriseres ved hjælp af SMPS-målinger og en Berner lavtryksimpaktor. De partikler der opsamles analyseres for deres kemiske sammensætning ved hjælp af kemiske analyser af den vandopløselige del og energidispersiv røntgenanalyse (EDX). Partiklernes morfologi undersøges ved elektronmikroskopi. En meget vigtig konklusion der kan drages ud fra disse målinger er, at antals- og massekoncentrationen af den submikrone aerosol ikke forøges væsentligt ved tilsatsfyring med halm ved de undersøgte betingelser.

Feltmålingerne har vist, at røggassen indeholder mellem $4 \cdot 10^7$ og $9 \cdot 10^7$ partikler/cm^3 ved 20°C med geometrisk middeldiameter fra 0.04 til 0.09 µm. Hovedbestanddelen af partiklerne bestemt ved EDX udgøres af grundstofferne Si, Al, Fe, K, Ca, S og P. Ca, S og P opkoncentreres på de submikrone partikler. Derimod mindskes koncentrationen af kalium jo mindre partiklerne er, sandsynligvis som følge af en reaktion med større partiklers inhold af Si og Al. Der er ikke fundet klor i partiklerne, hvilket indikerer at KCl, som findes i gasfasen ved høj temperatur, omdannes til K_2SO_4 via en sulfatiseringsreaktion.

Table of contents

List of symbols

The following symbols are used in the text most frequently.

c	Molar concentration [moles/m^3]
$\hat{C}$	Specific heat capacity [J kg^{-1} K^{-1}]
C^*	Collision rate [s^{-1}]
d	Particle diameter [m]
D/Dt	Substantial derivative
D	Diffusion coefficient [m^2/s]
G	Mass velocity [kg m^{-2} s^{-1}]
ΔG	Change in Gibbs free energy [J]
ΔH_c	Partial molar enthalpy of condensation [J/mole]
I	Aerosol condensation rate [kg/s]
J	Homogeneous nucleation rate [m^{-3} s^{-1}]
k_B	Boltzmann's constant = $1.380 \cdot 10^{-23}$ J/K
Kn	Knudsen number
L	Tube length [m]
m	Particle mass [kg]
M	Molecular weight [kg/mole]
N	Cluster concentration [m^{-3}]
N_A	Avogadro's number = $6.022 \cdot 10^{23}$ mole^{-1}
p	Pressure [Pa]
q	Number of molecules
Q	Volumetric flow rate [m^3/s]
r	Radius [m]
R	Tube radius [m]
Re	Reynolds number
R_g	Gas constant = 8.314 [J mole^{-1} K^{-1}]
s	Aerosol condensation rate [mole m^{-3} s^{-1}]
S	Saturation ratio
t	Time [s]
T	Temperature [K]
v	velocity [m/s]
y	mole fraction in the gas phase
z	Axial coordinate [m]
Z	Zeldovich non-equilibrium factor

Greek

α	Sticking coefficient
μ	Viscosity [kg m^{-1} s^{-1}]
ρ	Density [kg m^{-3}]
σ	Surface tension [N m^{-1}]
Φ	Number concentration [m^{-3}]
φ	Number size distribution function [m^{-3} kg^{-n}]

Subscripts

ae	Aerodynamic
cr	Critical
g	Gas
i	For component *i*
p	Particle
Sat	Saturator section

Abbreviations

CPC	Condensation particle counter
DMA	Differential mobility analyzer
EDX	Energy-dispersive x-ray analysis
LFAC	Laminar flow aerosol condenser
NAA	Neutron activation analysis
SMPS	Scanning mobility particle sizer

1. Introduction

The Danish government has for some years encouraged the use of biomass for energy generation, since combustion of biomass does not lead to a net emission of CO_2, and is therefore useful as a means to decreasing the total atmospheric CO_2 level. The Danish government has passed legislation that means that CO_2-emission must be reduced by 20% compared with the 1988 level by the year 2005. One means to achieve this is large-scale combustion of biomass, and consequently the Danish electric utility groups ELKRAFT and ELSAM are obliged to use 1,200,000 tonnes of straw and 200,000 tonnes of wood chips annually for energy production by the year 2000 (Clausen and Rasmussen, 1993, Sander, 1997). The fulfilment of this obligation is to be reached by co-firing of coal and straw in pulverized coal-fired units, grate-firing of wood chips and straw supplying steam to a coal-fired plant, and co-firing of coal, straw, and wood chips in circulating fluid bed combustors.

This strategy is however not without problems, since combustion of many biomass fuels leads to an increased deposition of corrosive species on heat transfer surfaces inside the boiler. Another potential problem is an increased production of submicron aerosol, as measurements of aerosols from combustion of straw, which is the main biomass fuel in Denmark, have shown. These measurements revealed an average submicron aerosol concentration of 800 mg/Nm^3 upstream from the particulate matter removal device (Christensen, 1995). These particles were furthermore of a size which makes them difficult to remove as discussed below, which will increase the cost of cleaning the gas prior to emission significantly. An important element in the official Danish energy policy for utilization of biomass is large-scale co-combustion of straw and coal in utility boilers. At present, there is no knowledge of the consequences of implementing this strategy with regard to particulate emission.

1.1 Aerosol sources and human exposure

An aerosol is a suspension of particles in a fluid. Ambient air to which humans are exposed always contains particles varying in concentration and composition. This aerosol has many sources, both natural and anthropogenic (i.e., man-made). Natural sources include direct emission of sea salt, rock and soil dust, biological material, and volcanic material, as well as gas-to-particle conversion of SO_2, nitrogen oxides (NO_x), and volatile organic compounds (VOCs). Anthropogenic emissions can also be divided in direct emissions (e.g., from combustion, biomass burning, and industrial processes) and secondary particle formation from gas-to-particle conversion similar to that from natural sources (Wolf and Hidy, 1997). The total emission of particles to the atmosphere has been estimated by several investigators. According to these, natural emissions are in the range 1000-13000 Tg/year, and anthropogenic emissions in the range

1000-3500 Tg/year (Wolf and Hidy, 1997). The estimates are not directly comparable, since the investigators cited have different definitions of which particle sizes are to be included.

The actual exposure of an individual to airborne particles is influenced by several factors. One is the size of the emitted particles. Transport processes are strongly dependent on particle size, and a distinction between fine-mode and coarse-mode particles is usually made. The fine mode is that fraction of the particles having aerodynamic diameters d_{ae} of less than 2.5 μm, and the coarse mode as particles with d_{ae} greater than 2.5 μm. Coarse-mode particles are not transported far from their source, so only persons close by are exposed to them. Particles from natural sources usually fall in the coarse mode. Fine-mode particles, on the other hand, can be transported far from their origin, and can therefore effect much larger numbers of individuals. The composition of the fine fraction at a given test site does however show significant spatial variation (Harrison and Jones, 1995, Monn et al., 1995).

Aerosols have received much interest in recent years due to indications that they have a profound impact on public health. One such indication is the recent proposal of a correlation between submicron particle concentration and mortality (Dockery et al., 1993, Friedlander and Lippmann, 1994). The precise cause for this increase in mortality with increasing aerosol concentration is not known, but combustion-generated particles have been suggested as the culprit (Chemical and Engineering news, p.9, Aug. 2, 1995). Furthermore, it has for some time been known that fine-mode particles produced in combustion processes are enriched by potentially harmful trace elements (Linak and Peterson, 1986, Kauppinen and Pakkanen, 1990, Obernberger et al., 1997). Finally, submicron particles are known to penetrate deeply into the human lung. These facts have resulted in a significant change in the attitude towards aerosol emission in the United States, as indicated by the announcement of a new standard for particulate matter (PM) under the national ambient air quality standards. By this standard, the concentration of particles of diameter less than 2.5 μm ($PM_{2.5}$) must not exceed an annual average of 15 μg/m^3 (USEPA, 1997).

Submicron aerosols are also an important factor for visibility degradation and have long residence times in the atmosphere compared with larger particles (Friedlander, Chp.5). For all the above mentioned reasons, the main focus in this work is on the fine-mode particles.

1.2 Particle formation in coal combustion

An important contributor to submicron aerosol loading in ambient air is the combustion of fossil fuels. Coal, which is the most important of these, contains 2 to 30 percent non-combustible material, part of which vaporizes in the furnace and subsequently condenses to produce particulate fly ash. The main constituents of the fly ash are Al, Ca, Fe, Mg, and Si. The

submicron fraction is typically 1 percent of the total fly ash mass. Although the demands for removal of particulate matter have increased dramatically in recent years, the capture of fine-mode particles is still challenging because most particulate matter removal devices show a minimum in efficiency for particles with diameters from 0.1 to 1 μm (McCain et al., 1975, McElroy et al., 1982).

The coal used in a typical suspension-fired boiler is crushed to obtain particles with an average diameter of approximately 50 μm, and injected into the boiler with primary air in the burners, which may be placed on one wall, on opposing sides or in the corners of the boiler. The particles are ignited and the flame temperature in the near-burner section peaks at 2000 K or more. The heat transferred to the water tube walls by radiation and convection in the furnace generates steam at high temperature and pressure. The flue gas is further cooled by convection as it passes through the boiler. A particulate matter removal device, e.g., an electrostatic precipitator or a baghouse filter, is usually placed upstream of the stack.

Numerous investigators have collected and analyzed fly ash both in the field (e.g., McCain et al., 1975, Markowski and Filby, 1985, Kauppinen and Pakkanen, 1990, Kauppinen et al. 1996), and in the laboratory (Flagan and Taylor, 1981, Quann et al., 1990). When the fly ash mass distribution is plotted, two distinct peaks are usually revealed. One is in the submicron range and has its maximum around a diameter of 0.1 μm (Damle et al., 1982). This is the previously mentioned fine mode. The second, larger peak is the coarse mode, which consists of particles with diameters of 2-50 μm.

To explain the characteristics of the fly ash it is necessary to investigate the fate of an individual coal particle after injection into the boiler. The formation mechanisms for both fine and coarse mode particles have been known for some time and are presented in figure 1.1 (Flagan and Friedlander, 1978, Neville and Sarofim, 1982, Quann and Sarofim, 1982).

A coal particle is injected into the boiler and heated by radiation and mixing with hot gases. First volatile organic compounds originally present in the coal or produced by pyrolysis are released, and the remaining char shrinks as it burns. The non-combustible material in coal is present as small inclusions or bound to organic structures (Flagan and Friedlander, 1978). The inclusions melt and coalesce as the carbonaceous char burns. Finally, the char breaks up and burns out to leave the mineral matter which constitutes the coarse mode fly ash, which is mainly transported with the flue gas through the boiler, where part of it is deposited on heat exchanger surfaces. The composition of the coarse mode fly ash is strongly dependent on the composition of the fuel and on the combustion conditions. Other coarse-mode fly ash formation processes are shedding of surface particles and fracturing of mineral grains (Baxter et al., 1997). The number of particles

formed from a given coal particle depends on coal rank and individual coal particle size (Baxter 1992).

The fine mode particles are believed to be produced by a completely different mechanism. They consist mainly of oxides or sulphates of aluminum, calcium, iron, magnesium, and silicon, although their composition is also dependent of coal composition and rank (Quann et al., 1990). When the coal particle burns, temperatures exceeding the flame temperature are reached in the interior of the char. Since the concentration of oxygen is low near the burning particle, reducing conditions prevail, and refractory elements such as Al, Ca, Fe, Mg, and Si are released as reduced species. As these leave the particle by convection and diffusion, they encounter the higher oxygen

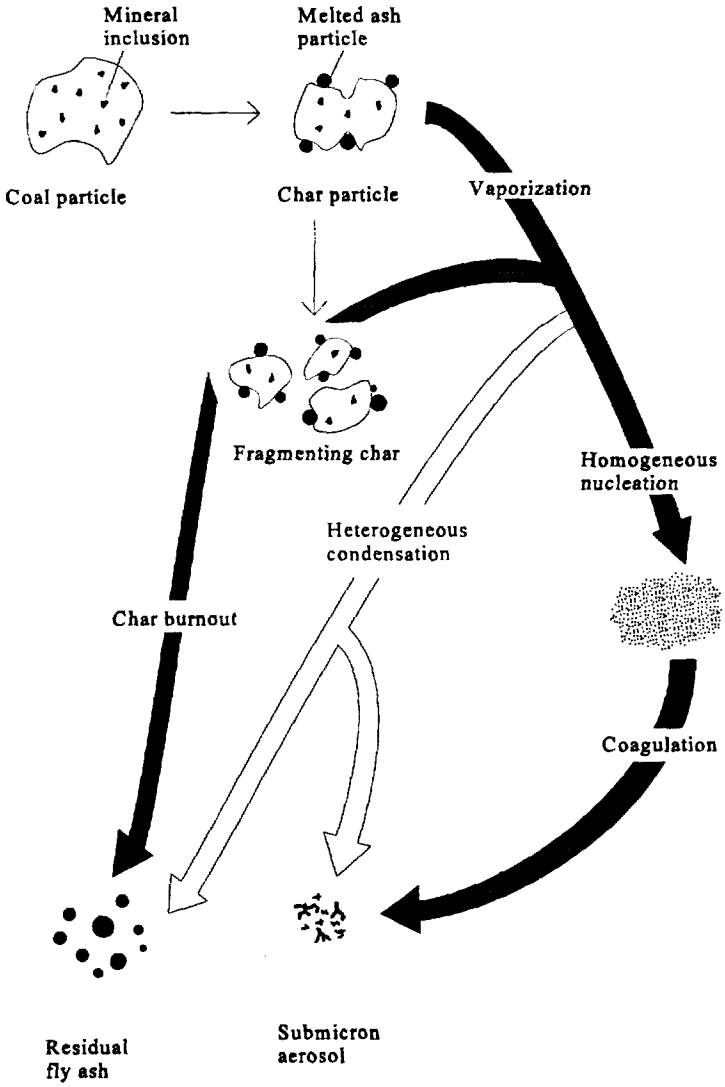

***Figure 1.1** Schematic of formation mechanisms in fly ash formation. Adapted from Helble et al., 1986.*

concentration in the bulk phase of the flue gas, where they are reoxidized. This causes an extremely high degree of supersaturation, which results in homogeneous nucleation of the refractory species (Senior and Flagan, 1982). Some investigators believe the homogeneous nucleation of iron and magnesium is the first step, since these oxides are found in the core region of the submicron particles (Neville and Sarofim, 1982). A layer of SiO_2 is found deposited on the core, apparently formed by heterogeneous nucleation of SiO_2, which appears later in the formation process since the oxidation of SiO to SiO_2 is relatively slow. Subsequently, more volatile compounds of Na, As, and Sb condense on the SiO_2 surface as the flue gas is cooled. Some organically bound inorganic material and very small mineral inclusions may be transported to the bulk phase of the flue gas by convection without evaporation and contribute to the fine mode (Baxter et al., 1997).

Kauppinen et al. (1996) have investigated the morphology of the fine mode particles by electron microscopy. They find the submicron particles to consist of agglomerated primary particles, which are 20 to 60 nanometers in diameter. The primary particles are proposed to be formed from sintering of homogeneously nucleated particles with diameters from 5-10 nanometers. As the flue gas cools, the sintering rate decreases and colliding particles form agglomerates. This mechanism is confirmed by calculations by Lehtinen et al. (1996).

1.3 Particle formation in straw combustion

Potential biomass fuels include residual products such as wood waste, nut shells, and various straw types (e.g., from cereal, rice, or oil seed rape), as well as crops grown solely with energy production in mind. Previous experience with combustion of some biomass fuels, including straw, has revealed severe problems with slagging, fouling, and particulate matter emission (Miles et al., 1996). These problems are closely linked to the chemical composition of the biomass ash. The ash content of biomass fuels is usually 5-10 % of total mass, and in some biomass fuels the alkali level, especially of potassium, is very high, e.g. 1.5 % in wheat straw (Christensen, 1995, Miles et al., 1996). This can be compared with coal, which typically contains less than 0.1 % potassium (Linak and Peterson, 1986). The alkali content of both coal and biomass can vary greatly depending on coal rank and origin, and on biomass source, growth conditions, and leaching by rain. As the alkali salts are present as simple salts or bound in the organic matrix, 15-40 % of the potassium in the biomass fuels can readily be volatilized, and as much as 60-90 % is reactive in typical combustion conditions. This is significantly more than in coal, where potassium is less reactive as it is often bound in refractory minerals, such as illite (Miles et al., 1996). The high alkali content is problematic as these elements contribute to the forming of sticky deposits in the boilers on metal and refractory surfaces by lowering the melting point of the fly ash.

In the following, the focus will be on straw combustion, since this is the main biomass fuel in Denmark. The formation mechanisms of fly ash in straw combustion are less thoroughly investigated than those of coal combustion. Field studies of aerosols from combustion of pure straw in a stoker-type boiler have revealed that the submicron particles consist almost entirely of K_2SO_4 and KCl. Furthermore, electron microscopy reveals that the particles are formed by only a few agglomerated primary particles (Christensen, 1995). There are two putative formation routes for this submicron aerosol. One is homogeneous nucleation of the potassium salts as the alkali-containing flue gas cools. The other is heterogeneous nucleation of potassium salts on particles formed at high temperature, as in coal combustion. Christensen (1995) has carried out calculations which indicate that the first route can explain the observed variations in aerosol concentration and size, as well as the distribution of chlorine and sulphur between stack gas and particle phase. The rate of sulphation in the gas phase of KCl to K_2SO_4 according to the net reaction

$$2KCl + H_2O + SO_2 + \tfrac{1}{2}O_2 \rightharpoonup K_2SO_4 + HCl \qquad \textbf{(1.1)}$$

is crucial for the composition of the particles as well as the gas phase, and is close to equilibrium at temperatures above 900 °C. However, this theory has yet to be confirmed by measurements under more controlled conditions.

A better understanding of the aerosol formation mechanisms in straw combustion is necessary if particulate matter emission and fouling problems are to be avoided, particularly in view of the Danish plans for large-scale use of straw in conventional coal-fired plants.

2. Design of a laminar flow aerosol condenser

The goal of the laboratory work is to provide new insight in the particle formation processes which occur when straw is burned in power generation furnaces. This first part of a greater investigation comprises the particle formation from pure KCl.

When studying homogeneous nucleation, a number of different experimental methods may be applied. Many early studies were made using the diffusion cloud chamber, in which a vapour is evaporated and diffuses to a cooled collecting plate. The temperature gradient causes supersaturation at some position in the chamber where homogeneous nucleation occurs (see e.g. Katz, 1970, Kacker and Heist, 1985, Smolík and Žmídal, 1993). Another instrument is the expansion cloud chamber, in which supersaturation is achieved by expanding a saturated gas rapidly and adiabatically (Sharaf and Dobbins, 1982, Schmitt et al., 1983, Wagner and Strey, 1984). Both of these methods have been used to investigate liquids at temperatures below 500 K. A third possible experimental setup is the laminar flow aerosol condenser (LFAC), in which a carrier gas is saturated with the component to be investigated. Sufficient time is allowed to develop the laminar flow profile of the saturated gas, which subsequently is subjected to a controlled drop in temperature. The sudden cooling causes a supersaturation of the condensible component, sufficiently high to enable homogeneous nucleation. The aerosol formed by this process is analyzed at the condenser outlet (Nguyen et al., 1987, Anisimov et al., 1994).

The LFAC was chosen in this work, since it allows continuous operation at high temperature, as well as facile introduction of seed nuclei to investigate the influence of heterogeneous nucleation on the aerosol characteristics. Thus, by comparing the effluent aerosol with results based on a detailed mathematical model, the LFAC is well suited to investigate aerosol dynamics in many applications. It has previously been used at the Aerosol Laboratory to examine the homogeneous nucleation of sulphuric acid (Simonsen, 1993).

The laminar flow aerosol condenser used in this study is a tubular furnace, see figure 2.1, in which two Al_2O_3-tubes are placed, one inside the other. In the furnace nine heating zones can be controlled individually.

Carrier gas enters the inner tube upstream of the furnace and passes a packing of porous α-alumina pellets immediately before entering the larger tube. The pores of the pellets contain solid crystals of the component to be investigated. The crystals evaporate, and carrier gas saturation is secured by appropriate selection of the residence time in the pellet packing. The temperature in the three uppermost heating zones, in which the inner tube is placed, is constant. The remaining six sections provide a controlled cooling of the gas at a selectable rate.

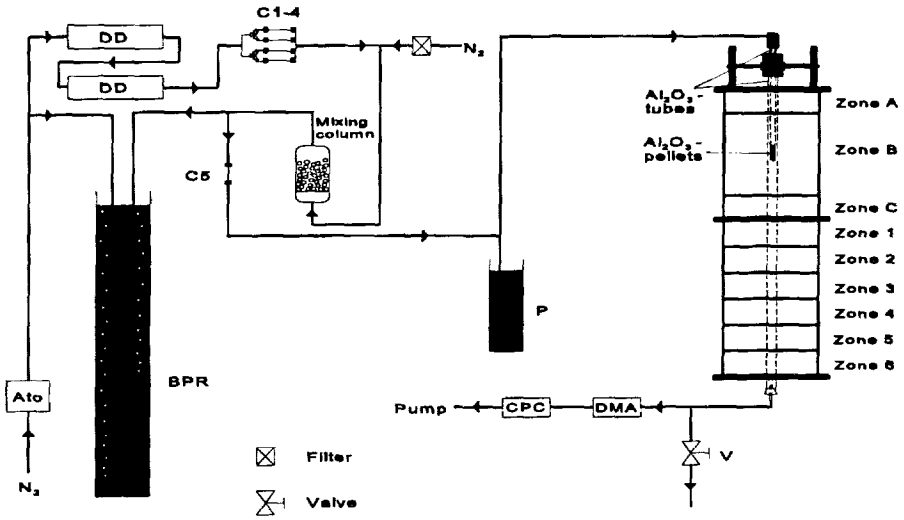

Figure 2.1 *Laboratory setup.* ***Ato****: Atomizer,* ***BPR****: Back-pressure regulator,* ***C1-C4, C5****: Capillary tubes 1-5,* ***CPC****: Condensation particle counter,* ***DD****: Diffusion drier,* ***DMA****: Differential mobility analyzer,* ***P****: Pressure indicator,* ***V****: Valve.*

The effluent aerosol is analyzed at the tube outlet with the scanning mobility particle sizer (SMPS) system or in some cases a Berner-type low pressure cascade impactor (BLPI). The SMPS system consists of a condensation particle counter (CPC) and a differential mobility analyzer (DMA). In some experiments the carrier gas is sampled upstream from the furnace inlet.

2.1 Tubular furnace

The furnace was built according to my specifications by Scandia-Ovnen A/S. It was further reconstructed by the workshop at the Department of Chemical Engineering in order to obtain a more smooth transition from the saturator to the condenser section. It can be viewed as having two parts: A saturator section consisting of the three uppermost heating sections (zones A, B, and C), and a condenser section consisting of the remaining six sections (zones 1-6), cf. figure 2.1. The total length of the furnace is 173 cm. The inner diameter of the furnace was selected to be 40 mm, which allows a 200 cm Al_2O_3 tube (Friatec Gmbh.) with outer diameter of 30 mm and inner diameter of 24 mm to extend through both saturator and condenser sections. A second 100 cm Al_2O_3 tube with outer diameter of 20 mm and inner diameter of 14 mm is placed inside the larger tube, and the carrier gas enters the furnace through this tube. These dimensions are selected so that even at elevated temperature the Reynolds number *Re* never exceeds 200 in the outer tube and 400 in the inner tube, respectively, and the flow is therefore well below the limit for laminar flow (e.g. Bird et al., p. 47). The estimated length required to build up a parabolic velocity profile is $0.035 \cdot D \cdot Re$, where D is the tube diameter. This corresponds to approximately 14 cm in the outer tube of the condenser.

The purpose of the saturator section is to heat the carrier gas to the saturation temperature, and to maintain this temperature as the gas is saturated with the component of interest. The length of tube the gas has to pass through in order to attain the saturation temperature can be estimated from a simple model of heat conduction in a laminar flow with constant tube wall temperature. The resulting cup-mix gas temperature is shown in figure 2.2 for a constant wall temperature of 750°C and a gas flow of 4 l/min at 20°C.

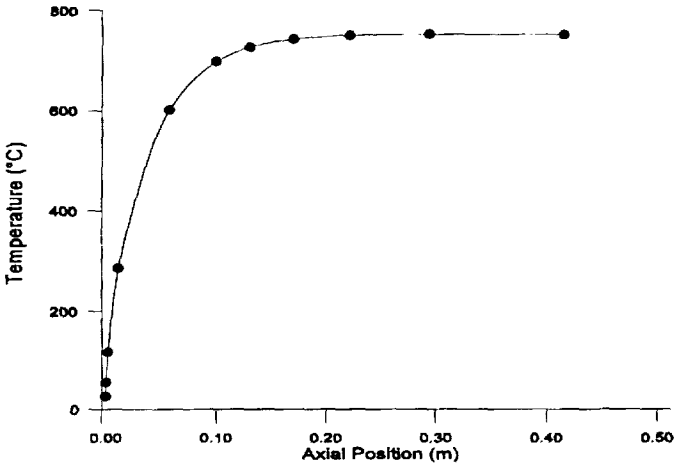

Figure 2.2 *Calculated cup-mix gas temperature in laminar flow with constant wall temperature of 750°C. Gas flow 4 l/min at 20°C*

The end of the inner Al_2O_3 tube is positioned at the midpoint of zone B in the saturator section (cf. figure 2.1). A packing of porous α-alumina pellets (kindly supplied by Haldor Topsøe A/S) is placed on a wire netting inside the tube. Prior to the experiment, crystals of KCl have been deposited in the pore system of the pellets, cf. section 3.1. The amount of pellets the gas needs to pass through in order to reach saturation can be estimated from a model, which assumes that the inner tube and pellets can be viewed as an isothermal packed column with spherical packing elements and plug flow. The model is further described in appendix A, and as seen in figure 2.3 the saturation ratio of KCl reaches 0.99 after approximately 15 cm, assuming a pellet size of 5 mm and a gas flow of 4 l/min. Increasing pellet size and gas flow also leads to an increase in the residence time necessary to reach satisfactory saturation. The porous α-alumina pellets are somewhat irregular in shape, but the largest dimension never exceeds 5 mm. The flow in all experiments is 4 l/min, and the minimum amount of pellets is 10 g of pellets, corresponding to a packing 8 cm in length. Measured particle size distributions were unaffected by doubling the amount of pellets to 20 g, and it is concluded from experiments that 10 g of pellets is sufficient, however, 20 g are used in most experiments. The total length of the saturator section was chosen to be 76 cm, which leaves a comfortable margin of safety for heating and saturation.

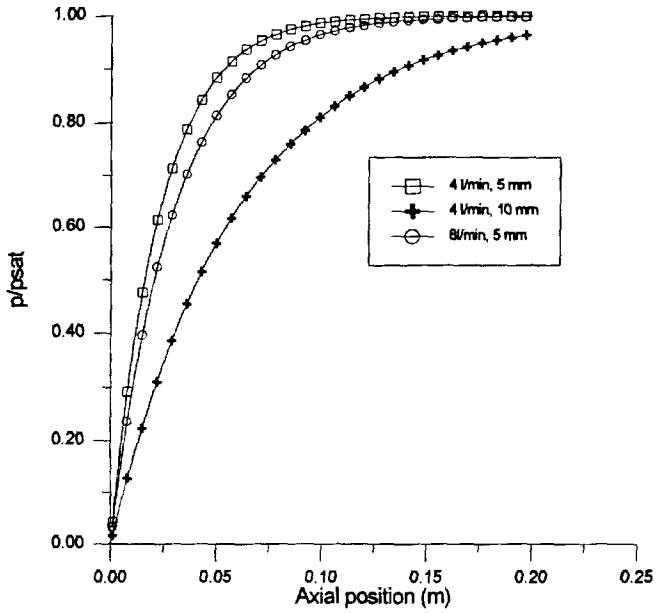

Figure 2.3 *Calculated saturation ratio of KCl as a function of axial position in packing of porous pellets. Temperature 800 °C.*

The temperatures of the condenser zones 1-6 in figure 2.1 are set to produce a well-defined temperature profile in the alumina tube. With measurements of the inner wall temperature (cf. chapter 3), the gas temperature at any position in the condenser can be calculated. Homogeneous nucleation of KCl is expected to commence when the hot, KCl-saturated gas during cooling reaches a temperature of approximately 650°C (Christensen, 1995 Ch. 19). The furnace was therefore designed to attain a flexible cooling rate in the temperature interval from 800 to 500°C, with particular emphasis on obtaining a fast, controllable cooling to simulate the conditions in the heat exchanger section of a utility boiler. The temperature profile realised in the furnace is described in the following chapter. The plug-flow residence time in the condenser section is approximately 2.5 seconds with a gas flow of 4 l/min at 20°C, hence the influence of coagulation is assumed negligible under the conditions used in the present work.

2.2 Diffusion drier

Seed nuclei are in some cases added to the carrier gas to investigate the influence of heterogeneous nucleation on the aerosol characteristics. A six-jet atomizer (TSI Inc., model 3076) produces a droplet-containing gas stream. A fraction of this stream is dried in two serial diffusion driers and diluted with dry nitrogen, before mixing with the carrier gas in a small column packed with 4 mm glass Raschig rings, cf. figure 2.1.

The diffusion drier (figure 2.4) is a straight cylindrical tube packed with molecular sieve drying particles (CECA, zeolite 3 Å) in an annulus. The gas from the atomizer flows through a concentrical wire netting tube in the cylinder. The flow is laminar, and water vapor diffuses

through the wire netting to the drying agent. The diffusion drier was used in a previous study, where the water content of the effluent gas was found to be negligible for a gas flow of 1000 cm^3/min (Simonsen, 1993 chapter 11).

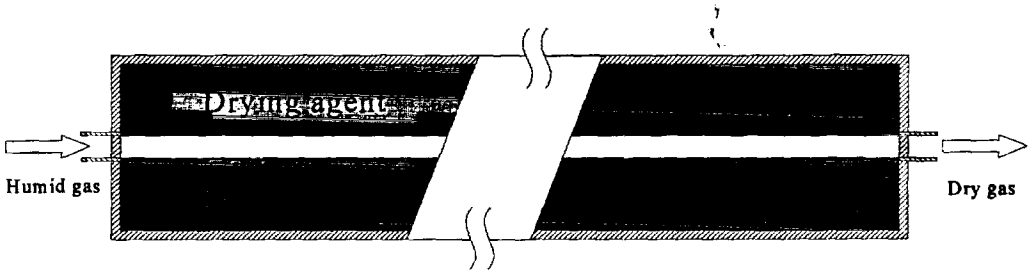

Figure 2.4 *Schematic cross-section of diffusion drier. The gas flows through a wire netting tube as water vapor diffuses to the drying agent.*

2.3 Flow control

The purpose of the flow control system is to produce a constant inlet stream containing seed particles. Variation of the inlet number concentration of nuclei over a range of several orders of magnitude should furthermore be possible. This is achieved by leading the dried seed nuclei gas stream from the diffusion driers to one of four different capillary tubes, C1-C4 in figure 2.1. The gas flow Q through a capillary tube is determined by the gas viscosity μ, tube length L, radius r, and the pressure drop Δp, as indicated by the Poiseuille law (see e.g. Bird et al. (1960) p 45):

$$Q = \frac{\pi \Delta p r^4}{8 \mu L} \qquad (2.1)$$

The four capillary tubes have different length and radius, but fixed Δp (and μ). Δp is fixed as the difference in pressure determined by the length of submersion of two glass tubes in the hydrostatic back-pressure regulator BPR on figure 2.1. The capillary tubes C1-C4 thus yield different flow rates of undiluted aerosol. The total flow to the furnace is controlled by the capillary tube C5. Increasing the dilution flow of nitrogen to more than 4 l/min upstream from C5 will not increase the flow to the furnace, since the upstream pressure is determined by the position of the shortest glass tube in the BPR. The pressure downstream from C5 is measured by separate glass tube in water, P.

2.4 The SMPS system

In this study, the aerosol is mainly characterized using the SMPS system, which consists of a differential mobility analyzer (DMA) (TSI Inc. model 3071 or 3071a) and a condensation particle counter (CPC) (TSI Inc. model 3022). The DMA charges the entering polydisperse aerosol particles and subsequently separates them in an electric field. The CPC causes the nearly monodisperse aerosol particles to grow by condensation of n-butanol on the particle surfaces. The increase in size allows the CPC to count the particles using an optical method.

In all experiments, the flows are as follows: Polydisperse 0.3 l/min, sheath air 3.0 l/min, monodisperse 0.3 l/min, and excess air 3.0 l/min. The measuring range with these flows is 0.014 - 0.81 μm. Critical orifices are used to control the flow rates where possible. CO1 and CO2 are capillary tubes in which the flow is critical due to the operating downstream pressure of approximately 0.15 bar. The aerosol flow from the furnace is distributed to the SMPS according to figure 2.5. Sheath air is usually drawn from the sample stream and filtered in a cotton pre-filter and an Absolife 0.6 μm high efficiency membrane filter (Gelman Sciences), which eliminates the influence of variations in upstream pressure. It also lowers the residence time in the tubing from furnace to SMPS.

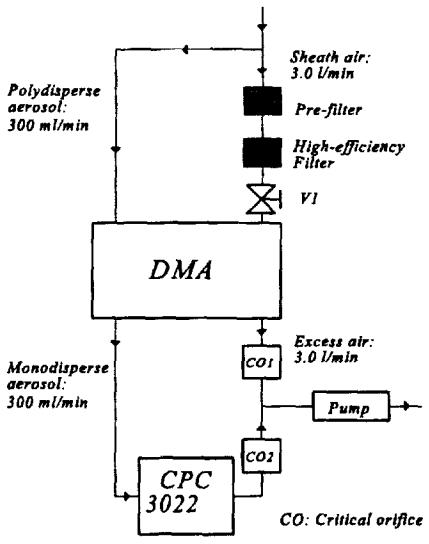

***Figure 2.5** The flows of the SMPS with the CPC 3022. The valve V1 is a part of the DMA.*

2.5 Aerosol sampling

In most experiments, the aerosol is sampled through a 1/4" tube placed in a plug at the condenser tube outlet. Thus, the entire flow is collected in this tube and a cup-mix size distribution is obtained. The 0.3 l/min polydisperse stream which the SMPS system needs is withdrawn from this 1/4" tube. Stainless steel or electrically conducting plastic tubing (TYGON®) is used throughout the entire setup to minimize particle loss due to electrostatic forces exerted by electrical charges at the tube wall.

3. A mathematical model for the laminar flow aerosol condenser

The interpretation of results from the laminar flow aerosol condenser (LFAC) requires a detailed mathematical model which includes mass and energy balances in addition to equations governing aerosol formation and growth. In this chapter such a model is described. It was first developed by Ole Simonsen, who investigated binary homogeneous nucleation in the sulphuric acid-water system (Simonsen, 1993). A one-component model was also developed, which has been modified in this work to investigate the homogeneous nucleation of potassium chloride. By changing the component-specific parameters of the model, it can readily be applied to describe the homogeneous nucleation of other components.

The LFAC described in the preceding chapter is essentially a tube with an externally cooled wall. The equations which describe momentum, mass, and energy conservation in such a system with laminar flow are well known. This work follows the notation from Bird et al. (1960). The gas flowing through the LFAC contains inert and condensible components, as well as seed particles which act as condensation nuclei.

A number of assumptions are made at the outset:

- The LFAC is assumed to operate at steady state.
- The laminar velocity profile is fully developed at the condenser inlet
- Axial diffusion is negligible
- The gas phase can be assumed to be ideal
- The mole fraction of the condensing component is small

3.1 Transport equations

Cylindrical coordinates are used throughout this chapter with r the radial coordinate and z the axial. The temperature and thus the density of the gas ρ_g will change both in axial and radial direction as the gas is cooled. The velocity profile therefore deviates from the parabolic. Therefore the assumption is made that the mass velocity G, defined as

$$G = \rho_g v_z \tag{3.1}$$

where v_z is the linear axial velocity, remains parabolic. Radial components are thus neglected, and G can be calculated as

$$G = 2 G_0 (1 - (r/R)^2) \tag{3.2}$$

where G_0 is the mean mass velocity, and R the radius of the tube.
The mass balance equation for component i at steady state is (Bird et al., 1960)

$$\frac{1}{r}\frac{\partial}{\partial r}(rN_{ir}) + \frac{\partial N_{iz}}{\partial z} = -s_{im} \tag{3.3}$$

where N_{ir} and N_{iz} are the molar fluxes in radial and axial direction, respectively, and s_{im} the rate of aerosol condensation of component i. For diluted vapor components the molar average velocity is equal to the mass average velocity, and by neglecting axial diffusion the mass balance becomes

$$\frac{1}{r}\frac{\partial}{\partial r}(-rcD_{il}\frac{\partial y_i}{\partial r}) + \frac{\partial}{\partial z}(y_i c v_z) = -s_{im} \tag{3.4}$$

where D_{il} is the binary vapor/inert diffusion coefficient, y_i the mole fraction of component i, and c the total concentration. Inserting the total mass balance, where the condensation of diluted vapors has been neglected yields

$$-\frac{D_{il}}{r}\frac{\partial y_i}{\partial r} + (1-b_i)\frac{D_{il}}{T}\frac{\partial T}{\partial r}\frac{\partial y_i}{\partial r} - \frac{D_{il}}{p}\frac{\partial p}{\partial r}\frac{\partial y_i}{\partial r} - D_{il}\frac{\partial^2 y_i}{\partial r^2} + v_z\frac{\partial y_i}{\partial z} = -s_{im} \tag{3.5}$$

where it has been used that the total concentration can be written as

$$c = c_0\frac{T}{T_0}\frac{p}{p_0} \tag{3.6}$$

T is the gas temperature and p the pressure, with subscript 0 referring to inlet conditions. The approximation

$$D_{il} = B_i T^{b_i} \Rightarrow \frac{dD_{il}}{dT} = b_i\frac{D_{il}}{T} \tag{3.7}$$

where B_i and b_i are component-specific constants has also been inserted.

The energy balance is made with the assumption that the heat content of the aerosol is negligible compared to that of the gas, and that all condensation heat is released in the gas phase. The energy balance for a n-component system is then (Bird et al., 1960)

$$\rho_g \hat{C}_p\frac{DT}{Dt} = -(\nabla\cdot\boldsymbol{q}) - (\tau:\nabla v) + \sum_{i=1}^{n_i}(\boldsymbol{j}_i\cdot\boldsymbol{g}_i) + \left(\frac{\partial\ln(1/\rho_g)}{\partial\ln T}\right)_{p,y_i}\frac{Dp}{Dt} + \sum_{i=1}^{n}(-\Delta H_{ci})s_{im} \tag{3.8}$$

Here $\hat{C}_p$ is the specific heat capacity at constant pressure, D/Dt the substantial derivative, $\boldsymbol{q}$ the energy flux, $\boldsymbol{j}_i$ the mass flux relative to mass average velocity, and ΔH_{ci} the partial molar enthalpy of condensation. A number of simplifications are now applied: As previously mentioned, the

system is at steady state. Furthermore, the pressure gradients are assumed negligible, as is axial heat conduction. Only conductive flux is considered for the heat flux q. Assuming finally that the thermal conductivity k is a function of temperature only, the energy balance can be simplified to

$$\rho_0 \frac{T_0}{T} \hat{C}_p v_z \frac{\partial T}{\partial z} = \frac{k}{r}\frac{\partial T}{\partial r} + \frac{dk}{dT}\frac{\partial T}{\partial r}\frac{\partial T}{\partial r} + k\frac{\partial^2 T}{\partial r^2} + \sum_{i=1}^{n} (-\Delta H_{ci}) s_{im} \tag{3.9}$$

It has been used that the ideal gas density can be calculated as

$$\rho_g = \rho_0 \frac{T_0}{T}\frac{p}{p_0} \tag{3.10}$$

3.2 Boundary conditions

The initial conditions for z=0 are

$$T_{(z=0)} = T_0 \quad and \quad y_{i,(z=0)} = y_{i0} \tag{3.11}$$

The boundary conditions at the tube center, r=0, are given by the symmetry conditions

$$\left(\frac{\partial y_i}{\partial r}\right)_{r=0} = 0 \quad and \quad \left(\frac{\partial T}{\partial r}\right)_{r=0} = 0 \tag{3.12}$$

At the wall, r=R, the temperature is given as a function of axial position only, and the mole fraction of component i is given by the equilibrium vapor pressure at the wall temperature T_w.

3.3 Aerosol dynamics

It now remains to quantify the term s_{im}, i.e. the aerosol condensation rate, in equations (3.5) and (3.9). The following assumptions are made for the aerosol:

- The seed particles are spherical
- All particles are small enough to safely neglect gravitational sedimentation
- Residence time in the LFAC is sufficiently low to safely neglect agglomeration
- The aerosol moves convectively with the gas, and Brownian diffusion is negelected

The residence time in the condenser is estimated to approximately 2.5 seconds in chapter 2, which means that agglomeration is only important if the particle concentration is extremely high, e.g. above 10^9 cm^{-3}. The condensation rate therefore only includes aerosol condensational growth and homogeneous nucleation.

The expression for rate of condensation of component *i* on a particle is size-dependent. Very small particles obey the laws of the kinetic gas theory, the so-called Knudsen theory, while continuum mechanics describe the behavior of large particles. The dynamics of aerosols is therefore divided into three regimes; the Knudsen, the transition, and the continuum regime. To determine the appropriate regime the Knudsen number *Kn* is calculated, given by

$$Kn = \frac{2l}{d_p} \quad , \quad l = 2D_{il}\sqrt{\frac{\pi M_i}{8R_g T}} \tag{3.13}$$

In this equation l is the mean free path of the gas, and d_p the particle diameter. The size regimes are now determined approximately as follows:

	$Kn > 10$	: Knudsen regime
$0.1 \leq$	$Kn \leq 10$	: Transition regime
	$Kn < 0.1$	: Continuum regime

The aerosol condensation rate of component i on a single particle in the continuum range I_{Ci} is based on the steady state Maxwellian flux expressions, in this case including the Kelvin effect (Seinfeld, 1986).

$$I_{Ci} = \frac{dm_i}{dt} = \frac{2\pi d_p D_{il}(T_{av}) M_i}{R_g T}(p_i - p_{id}(T_d)) \quad , i = 1,n \tag{3.14}$$

where m_i is the particle mass, D_{il} the diffusion coefficient of i in the inert gas, T_d the particle temperature, T_{av} the average temperature $T_{av}=(T_d+T)/2$, M_i the molecular weight, R_g the gas constant, p_i the vapor pressure, and p_{id} the vapor pressure over the particle given by the Kelvin equation

$$\ln\left(\frac{p_{id}}{p_{i\infty}}\right) = \frac{4\sigma M_i}{R_g T \rho_l d_p} \tag{3.15}$$

in which σ is the surface tension, $p_{i\infty}$ the vapor pressure over an infinite plane, and ρ_l the density of the particle. The vapor pressure over a particle is thus greater than the vapor pressure over a plane surface.

In the Knudsen regime the growth rate I_{Kni} is calculated from kinetic gas theory (Friedlander, 1977):

$$I_{Kni} = \frac{dm_i}{dt} = \frac{\alpha_i \pi d_p^2 N_A M_i}{k_B T} \sqrt{\frac{R_g T}{2\pi M_i}} (p_i - p_{id}(T_d)) \quad , i = 1,n \tag{3.16}$$

in which α_i is the sticking or accommodation coefficient, stating the probability that a molecule which strikes the particle sticks to the surface, N_A Avogadro's number, and k_B the Boltzmann constant.

To obtain a growth expression I_i valid in the entire size range an interpolation expression which shows the correct asymptotic behavior is used (Seinfeld, 1986):

$$I_i = \frac{dm_i}{dt} = F(Kn_i) I_{Ci} \tag{3.17}$$

In this work the Dahneke interpolation formula is used (Dahneke, 1983):

$$F(Kn_{Di}) = \frac{1 + Kn_{Di}}{1 + 2\,Kn_{Di}(1 + Kn_{Di})/\alpha_i} \tag{3.18}$$

Where Kn_{Di} is the Knudsen number according to (3.13).

The particle temperature T_d in equation (3.14) and (3.16) is unknown, and must be found be found by an iterative procedure. This is described in detail by Simonsen (1993). The difference between T and T_d, caused by condensation or evaporation, is however often negligible.

Homogeneous nucleation may occur when the gas becomes supersaturated with respect to component i, i.e. when the saturation ratio defined as $S_i = p_i / p_{i\infty}(T)$ exceeds unity. In any vapor an equilibrium number of molecular clusters of gaseous molecules exist, the concentration of which increases when the saturation ratio increases, e.g. as a consequence of rapid cooling. If the saturation ratio is sufficiently high, large numbers of stable nuclei are formed by homogeneous nucleation. In this work only homomolecular homogeneous nucleation is considered, i.e. nucleation of pure species i, and the so-called classical theory is applied to calculate the rate J of homogeneous nucleation.
The change in Gibbs free energy caused by the formation of a single spherical particle of pure i with diameter d_p, which contains q molecules of i is

$$\Delta G = -q k_B T \ln S_i + \pi d_p^2 \sigma_i \tag{3.19}$$

The equilibrium cluster concentration N_i^e is assumed to follow a Boltzmann distribution:

$$N_i^e(q) = N_i(1)\exp\left[-\frac{\Delta G}{k_B T}\right] \tag{3.20}$$

where ΔG is given by (3.19) and $N_i(1)$ by $N_i(1)=p_i/k_B T$. When $S_i>1$, ΔG has a maximum for $q=q^*$, the so-called critical cluster size, which is found by setting the derivative of equation (3.19) with respect to q equal to zero.
The homogeneous nucleation rate J can now be stated as the product of three factors (Seinfeld, 1986):

$$J = C^* Z N^e(n_{1c}) \tag{3.21}$$

Here C^* is the growth rate of the critical cluster, Z the Zeldovich non-equilibrium factor and $N^e(n_{1c})$ the equilibrium concentration of clusters having the critical size. For growth by single molecule addition the three factors are given by

$$C^* = \frac{\alpha_i \pi d_{cr}^2 p_1}{k_B T}\sqrt{\frac{R_g T}{2\pi M_1}} \tag{3.22}$$

$$Z = \frac{2M_1}{\pi d_{cr}^2 N_A \rho_l}\left(\frac{\sigma}{k_B T}\right)^{1/2} \tag{3.23}$$

$$N^e = \frac{p_1}{k_B T}\exp\left(-\frac{\Delta G_{cr}}{k_B T}\right) = \frac{p_1}{k_B T}\exp\left(-\frac{16\pi\sigma^3 M_1^2}{3N_A^2\rho_l^2(k_B T)^3(\ln S_1)^2}\right) \tag{3.24}$$

where d_{cr} is the critical cluster diameter.

The aerosol condensation rate for component i can now be summarized as the sum of the aerosol growth rate and the nucleation rate. It is found in terms of the steady state n-component size distribution $\varphi(m_1,\ldots,m_n,T,r,z)$ by integrating the growth term and adding newly formed particles:

$$s_{im} = \int_0^{\infty} \frac{\varphi}{M_i} I_i \, dT_d dm_1 + \frac{n_{ic}}{N_A} J(r,z) \qquad (3.25)$$

growth nucleation

The aerosol is described by a population balance (e.g. Friedlander, 1978), where the number and properties of the particles are characterized by a population density function $\varphi(x,y,z,e_1,e_2,\cdots,e_n,t)$ where x,y, and z are the coordinates in a relevant coordinate system, $e_1,e_2,\cdots,e_n$ properties describing the particles and t the time. The number of particles in a volume element $\Delta x\ \Delta y\ \Delta z$ is defined as

$$\varphi \Delta x \Delta y \Delta z \Delta e_1 \cdots \Delta e_n \qquad (3.26)$$

Integration over all coordinates and properties yields the total number of particles Φ_e at time t:

$$\Phi_e = \int_x \int_y \int_z \int_{e_1} \cdots \int_{e_n} \varphi \, dx \, dy \, dz \, de_1 \cdots de_n \qquad (3.27)$$

3.4 Numerical solution

Equations (3.5) and (3.9) are simplified using the approximation of constant mass velocity, equation (3.1), and further by introducing appropriate dimensionless variables. The set of nonlinear second order differential equations are transformed to a set of ordinary differential equations by discretization of the radial cylindrical coordinate using the method of orthogonal collocation (Villadsen and Michelsen, 1978). The aerosol dynamics is handled using a sectional method, in which the continuous size distribution is divided into a number of size classes in which the particles are assumed to have identical properties (Gelbard, 1980). The solution uses the so-called moving sectional method (Gelbard, 1990), where, with sufficiently fine discretization, the continuous size distribution is represented by a number of monodisperse sections. The equations are integrated axially by a third order semi-implicit Runge-Kutta method in small Δz steps. In each step the mean rate of homogeneous nucleation is calculated. New size sections are added if the concentration of newly formed nuclei is above a specified limit. The size of the homogeneously nucleated particles is increased by 10 % to initiate growth. For further details on the numerical solution and the validation of the model the reader is referred to Simonsen (1993).

The numerical solution has been implemented in the computer code MONAERO.FOR in ANSI FORTRAN language. It is similar to the code of the same name used by Simonsen (1993), except in the following:

Component-specific parameters have been changed to reflect the shift in condensing component from sulphuric acid to potassium chloride. The physical properties of KCl and the carrier gas used in this work are shown in appendix B. Furthermore the wall temperature is now specified by the user as N piecewise linear functions. Therefore the input files have been changed to include wall temperature profile data. After integration is completed, the original program reported only the total number concentration, and the fraction of condensing component condensed on the tube wall. In addition to this, the output routines now calculate the average number size distribution and the mean particle size. Numerical parameters critical for the accuracy of the simulations are N_{col}, the number of collocation points, and Δz_{min}, the minimal step length in the axial direction. In this work, it is found that increasing N_{col} above six does not lead to a significant change in the integrated result. Likewise, the minimal step length needs to be $5 \cdot 10^{-4}$ or less to produce a stable integrated result. Increasing the demands for numerical accuracy only leads to a prohibitive simulation time.

4. Homogeneous nucleation of KCl

In chapter 1 KCl was identified as an important component in particle formation in combustion systems where straw is used as a fuel, since a large fraction of the total potassium in the gas phase will be in the form of KCl at high temperature, i.e. above 1100°C (Christensen, 1995). Furthermore, the nucleation of KCl is expected to take place at an easily attainable temperature of approximately 6-700°C (Christensen, 1995). Finally, KCl is readily soluble in water and therefore well suited for our method of gas phase saturation (cf. section 4.1). KCl was therefore selected as the component to investigate.

4.1 Experimental procedure

The design of the experimental apparatus is described in detail in chapter 2. The central unit of the setup is the 173 cm long tubular furnace, in which two concentric α-alumina tubes are placed. The outlet of the inner tube is at a distance of 40 cm from the inlet. Prior to the experiment 20 g of porous $\frac{1}{16}''$ α-alumina pellets are prepared by placing them in a boiling, saturated aqueous solution of KCl (Suprapure, Merck). After soaking for one hour, the pellets are removed, rinsed briefly with water to remove KCl crystals on the surface, and dried overnight at 100°C. The amount of KCl deposited in the pore system of the porous pellets is estimated by an approximate measurement of the pore volume: 10 g of clean, dry pellets are weighed, and submerged in deionized water until no more bubbles are released from the pellets. The pellets are dried with tissue paper and weighed again. The mass increase of the pellets is assumed to correspond to the amount (i.e. volume) of water deposited in the pore system. Assuming furthermore that the pore system of the pellets used in the experiments contain an aqueous solution of KCl at 50°C, the mass of KCl deposited can be estimated. Using this method, it is calculated that the prepared pellets contain sufficient KCl to saturate a gas flow of 4 l/min at 20°C for more than four hours at a saturator temperature of 750°C. The equilibrium vapor pressure of KCl is calculated by the expression given in appendix B.

Before mounting the α-alumina tubes, the furnace is locked in the horizontal position. Both tubes are placed in the air-cooled mounting unit, see figure 4.1, with the upper end of the smaller tube protruding from the mounting unit. The prepared Al_2O_3 pellets are weighed and subsequently placed on a stainless steel wire netting in the bottom end of the inner tube. A type K stainless steel jacket thermocouple is placed in the pellet layer. The high temperature and presence of KCl corrodes the thermocouple, which needs to be replaced after approximately 10-15 experiments. The tubes are inserted in the furnace, and the mounting unit secured at the top of the furnace. Gas leakage is prevented by sealing with Viton® O-rings. Nitrogen is supplied to the system through the inner tube.

The furnace is placed in the upright position, and the furnace power and the cooling air to the mounting unit turned on. Stabilization of the selected temperatures is ensured by allowing two hours of heating without gas flow followed by an additional two hours with a flow of filtered N_2 at the desired rate. Steady-state operation is confirmed by monitoring outlet size distribution from the time the carrier gas is turned on, as well as by monitoring the pellet temperature.

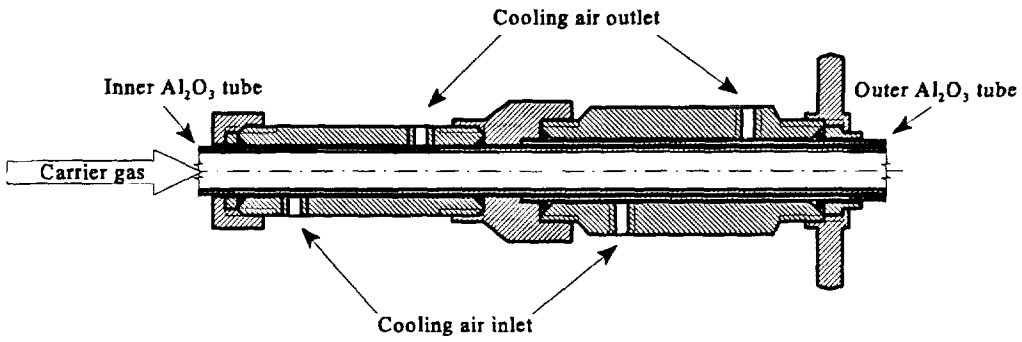

Figure 4.1 *Cross-section of mounting unit*

The SMPS system is turned on, and all flows in the system checked with a bubble flow meter (Hewlett-Packard). Data are collected on a PC. An average of 15-20 SMPS measurements can be made in one day. After the furnace temperature has reached the selected temperature, which usually is above 700°C in the saturator section, the Al_2O_3 tubes break if an attempt to move them in the axial direction is made.

Some of the gaseous KCl will condense on the externally cooled inner wall of the larger Al_2O_3 tube. The amount of KCl condensed on the wall is an important parameter for describing the condensation processes in the furnace, and is determined after each experiment without seed particles. In experiments without seed nuclei several different inlet concentrations are used in each run, and the amount of KCl on the wall can therefore not be referred to a specific set of operational parameters. Wall condensation is therefore not determined in this type of experiments.

After each experiment without seed nuclei the furnace is allowed to cool, the tubes are removed from the furnace and the pellets are weighed again. The outer Al_2O_3 tube is rinsed once with 200 ml of ultra-pure water and twice with 100 ml. The three samples are combined, and the conductivity of the solution measured. Wall deposition is then determined by comparing the measured conductivity with a laboratory standard. The conductivity of a fourth set of washing water and washing water from the inner Al_2O_3 tube are both negligible.

In experiments with addition of seed nuclei, the aerosol is sampled both upstream and downstream from the furnace. Inlet size distributions are measured immediately upstream from the furnace by disconnecting the seed feed from the furnace. The capillary flow control of the seed feed is sensitive to changes in pressure. When the seed-containing carrier gas is purged directly to ambient pressure the downstream pressure from the capillary tube C5 changes, cf. figure 2.1, since there is a finite pressure drop of 20-30 cm water over the furnace. By closing the valve V in figure 2.1, only 3.3 l/min is sampled by the SMPS system, and the surplus gas is forced through the tube P, the outlet of which is placed at exactly the position indicated prior to disconnection. The downstream pressure is then unchanged, and the flow through C5 the same as during outlet measurements.

Measuring the seed particle size distribution upstream from the furnace does not yield a sufficiently precise characterization of the conditions at the condenser inlet, since some particles are likely to be lost as the carrier gas passes through the pellet layer placed at the outlet of the inner tube. The penetration of seed nuclei through the pellets is therefore measured under conditions without KCl in the furnace. All other experimental parameters are otherwise identical to conditions where the actual seed nuclei experiments are performed. The experimental setup used is similar to that used in penetration measurements performed on the ejector probe (cf. chapter 5), and is described further in appendix D. The measurements yield the fraction of particles of all the size sections measured by the SMPS which pass through the pellet layer. An example of the measured penetration is shown in figure 4.2.

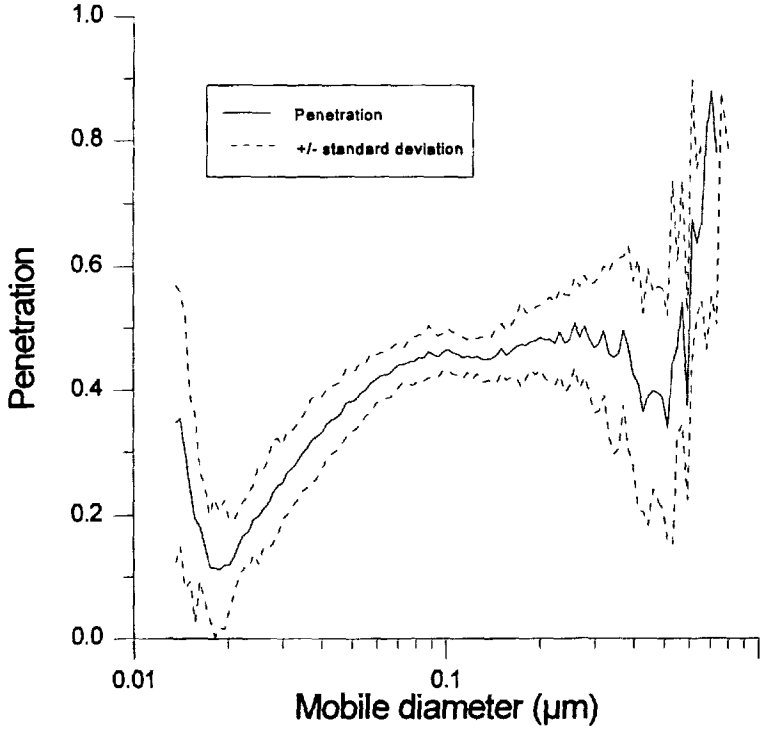

***Figure 4.2** Penetration of seed nuclei through the pellet layer of the LFAC. Saturator temperature 722°C.*

4.2 Wall temperature profiles

By selecting different temperature settings in zones 1-6 in figure 2.1, the wall temperature profile in the condenser section can be varied within wide limits. The inner wall temperature is measured by a type K thermocouple mounted on a 200 cm ceramic rod. The smaller of the two Al_2O_3 tubes is not mounted during these measurements. The point of measurement is insulated by a block of porous ceramic material (Super-isol, Skamol) and pressed against the tube wall, see figure 4.3.

The thermocouple is inserted from the outlet end of the outer Al_2O_3-tube, and allowed to attain thermal equilibrium before reading the temperature. This procedure is repeated at regular intervals along the inner tube wall. The profile is measured with a flow of 4 l/min of pure N_2 through the furnace without the inner tube.

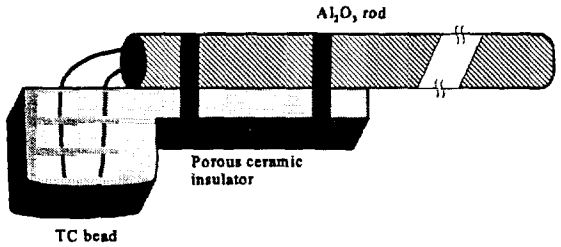

Figure 4.3 *Schematic of wall temperature thermocouple (TC).*

After meticulous testing the upper and lower limits of operation for the condenser section is found to be an average cooling rate of 625 K/s (profile 1) and 200 K/s (profile 3), respectively (figure 4.4). A third intermediate cooling rate of 330 K/s (profile 2) is also used. An attempt to increase the cooling rate above 625 K/s has the effect of inactivating the heating elements in the condenser section, leading to an unacceptably long period of stabilization. If the cooling rate is selected at a value lower than 200 K/s, the inner wall temperature profile deviates from the desired linear form as the temperature drops more sharply in the sections between the heating elements than in the heating elements themselves. This tendency is visible in profile 3, figure 4.4. The above mentioned settings for the temperature zones in the condenser section, termed profile 1, 2, and 3, were consistently used throughout this work.

The present investigation of homogeneous nucleation of pure KCl includes nine sets of experiments under conditions without seed particles and six with seed particles. The two main parameters determining aerosol formation and growth are the saturator temperature T_{sat}, which determines the concentration of KCl in the gas phase, and the temperature profile, i.e. the cooling rate. These parameters are varied according to table 4.1. Saturator temperatures of 709°C, 722°C, and 751°C are used, corresponding to KCl saturation concentrations of 85, 119, and 241 ppm

(mol/mol), respectively (cf. appendix B). These concentrations are within the limits of the field measurements of pure straw combustion, where the concentration of K is in the interval from 13 to 424 ppm with an average value of 200 ppm (Christensen, 1995). The highest saturator temperature is not used in experiments with seed nuclei, since heterogeneous condensation causes the seed particles to grow to sizes above the SMPS detection limit of 0.81 μm.

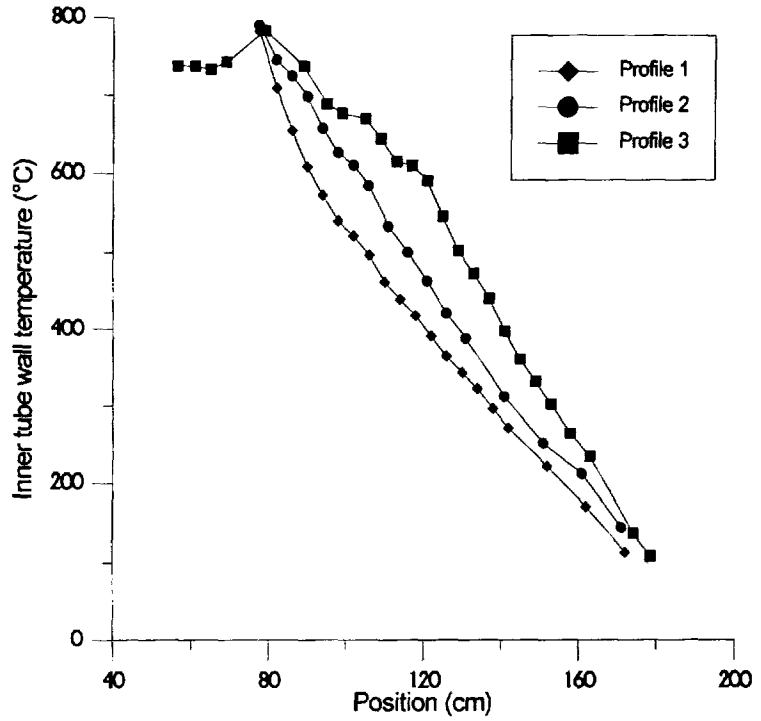

Figure 4.4 *Measured inner wall temperature profiles in the condenser. Gas flow 4 l/min. These three profiles are used throughout this study.*

***Table 4.1** Summary of experimental conditions*

Case	Saturator temperature	Temperature profile	cooling rate
1	709°C	1	635 K/s
2	737°C	1	635 K/s
3	751°C	1	635 K/s
4	709°C	2	330 K/s
5	722°C	2	330 K/s
6	751°C	2	330 K/s
7	709°C	3	200 K/s
8	722°C	3	200 K/s
9	751°C	3	200 K/s

4.3 Experimental results: No seed nuclei

It was very quickly verified that KCl nucleates readily under the selected experimental conditions. For each set of operational parameters (case 1-9 of table 4.1) simulations with the FORTRAN code MONAERO (cf. chapter 3) have been performed. The input for the simulations is discussed in detail in section 4.4. In the following, the experimental results from case one through nine are shown graphically in figure 4.5 to 4.13 along with results of the simulations. The particles formed are first described by number size distributions obtained with the scanning mobility particle sizer (SMPS) system. The area under the number size distribution curve is equal to the total number concentration (particles/cm^3) in the corresponding size range.

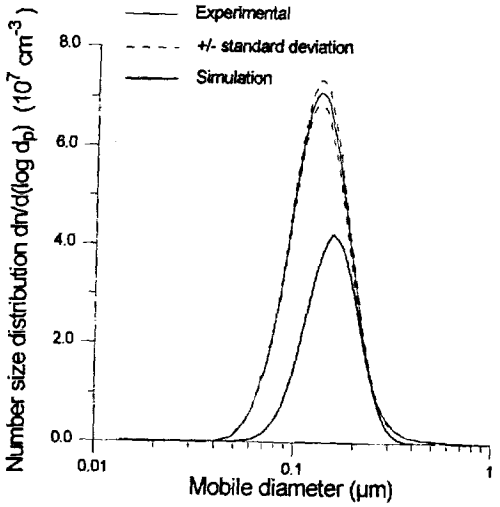

Figure 4.5 *Average number size distribution for case 1, table 4.1. Wall temperature profile 1, T_{sat} 709°C. Gas flow 4 l/min at 20°C.Average of 8 SMPS measurements.*

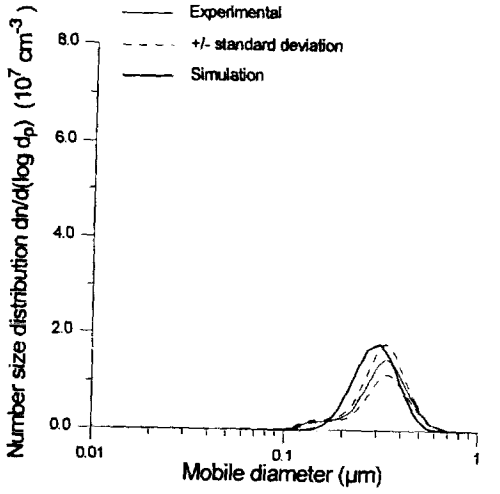

Figure 4.6 *Average number size distribution for case 2, table 4.1. Wall temperature profile 1, T_{sat} 737°C. Gas flow 4 l/min at 20°C. Average of 12 SMPS measurements.*

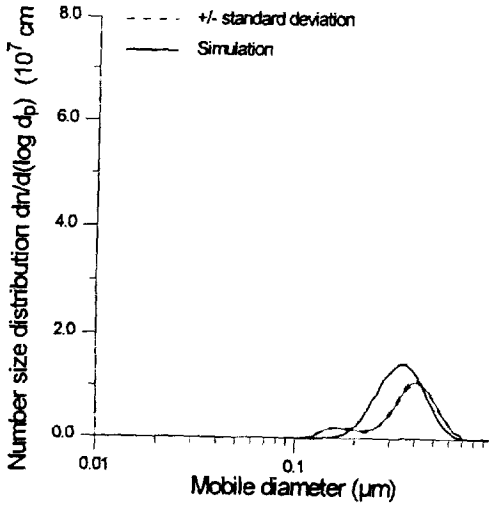

Figure 4.7 *Average number size distribution for case 3, table 4.1. Wall temperature profile 1, T_{sat} 751°C. Gas flow 4 l/min at 20°C. Average of 9 SMPS measurements.*

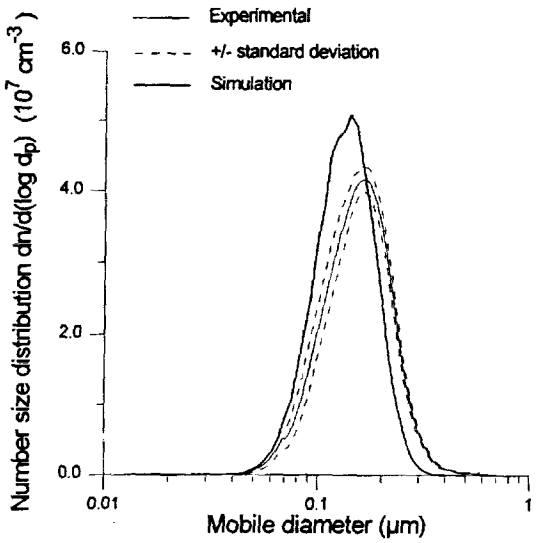

Figure 4.8 *Average number size distribution for case 4, table 4.1. Wall temperature profile 2, T_{sat} 709°C. Gas flow 4 l/min at 20°C. Average of 10 SMPS measurements.*

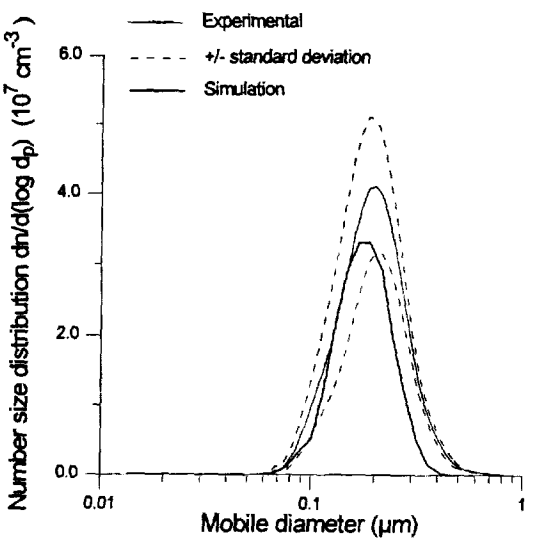

Figure 4.9 *Average number size distribution for case 5, table 4.1. Wall temperature profile 2, T_{sat} 722°C. Gas flow 4 l/min at 20°C. Average of 14 SMPS measurements.*

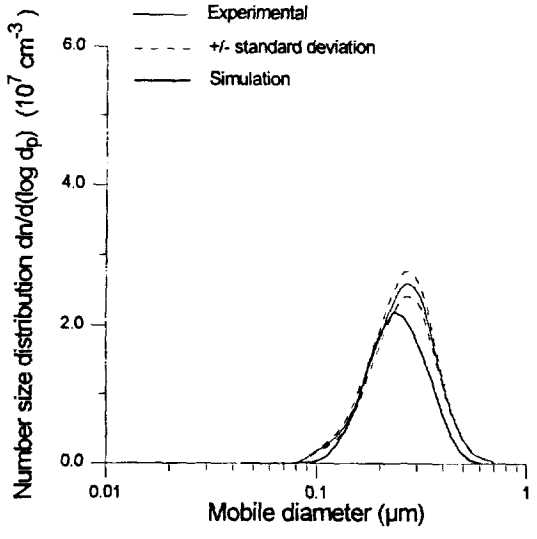

Figure 4.10 *Average number size distribution for case 6, table 4.1. Wall temperature profile 2, T_{sat} 751°C. Gas flow 4 l/min at 20°C. Average of 9 SMPS measurements.*

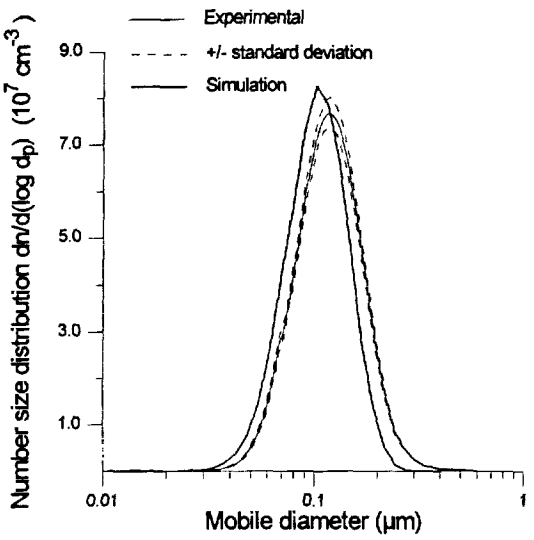

Figure 4.11 *Average number size distribution for case 7, table 4.1. Wall temperature profile 3, T_{sat} 709°C. Gas flow 4 l/min at 20°C. Average of 10 SMPS measurements.*

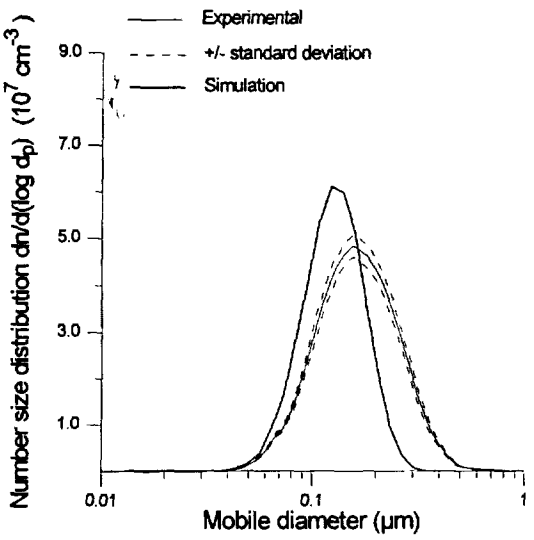

Figure 4.12 *Average number size distribution for case 8, table 4.1. Wall temperature profile 3, T_{sat} 722°C. Gas flow 4 l/min at 20°C. Average of 3 SMPS measurements.*

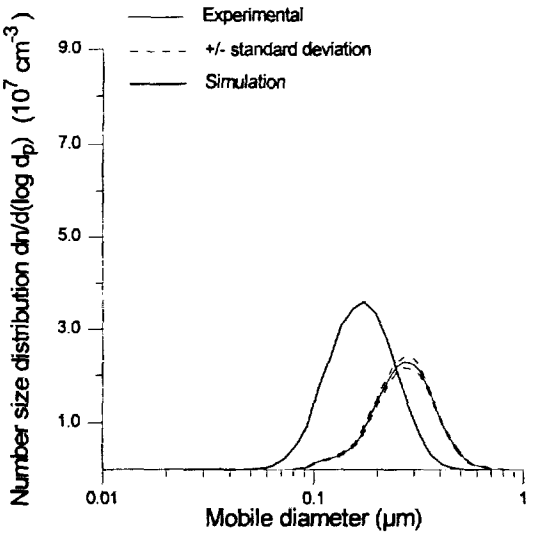

Figure 4.13 *Average number size distribution for case 9, table 4.1. Wall temperature profile 3, T_{sat} 751°C. Gas flow 4 l/min at 20°C. Average of 10 SMPS measurements.*

From the number size distributions it is possible to calculate the mass concentration of submicron KCl if the particles are assumed to be spherical. Knowing the total volume of gas which has

passed through the LFAC then allows a calculation of the total mass of the aerosol phase for a given experiment. The total gas volume also allows a calculation of the total amount of KCl released to the gas phase from the Al_2O_3 pellets, if the gas is assumed to be saturated at the temperature measured by the thermocouple placed in the pellet layer (cf. section 4.1). Finally, the actual mass of KCl evaporated from the pellets is calculated as the difference between pellet mass before and after the experiment. The experimental results for wall condensation in case 1-9 are listed in table 4.2 below.

Table 4.2 *Mass balances for LFAC experiments with no seed nuclei. T_{sat} is the saturator temperature, $\Delta m_{pellets}$ the mass of KCl evaporated from the pellets, $m_{particle}$ the mass of the aerosol phase, m_{wall} the mass of KCl deposited on the tube wall, m_{out} the sum of $m_{particle}$ and m_{wall}, m_{sat} the mass of KCl released to the gas phase assuming saturation with monomer (KCl) and both monomer and dimer (KCl + $(KCl)_2$), respectively, and wall condensation the percentage of total KCl which condenses on the tube wall.*

Case	Temp. profile	T_{sat} (°C)	$\Delta m_{pellets}$ (g)	$m_{particle}$[1] (g)	m_{wall} (g)	m_{out} (g)	m_{sat}[2] (g)		wall condensation (%)	
							KCl	KCl+ $(KCl)_2$	Sat.[3]	Meas.[4]
1	1	709	0.317	0.110	0.162	0.272	0.249	0.319	51	51
2	1	737	0.577	0.201	0.355	0.556	0.533	0.802	44	62
3	1	751	0.720	0.254	0.445	0.699	0.695	1.06	42	62
4	2	709	0.421	0.117	0.204	0.321	0.281	0.411	50	48
5	2	722	0.981	0.174	0.778	0.952	0.630	0.930	84	79
6	2	751	0.754	0.268	0.495	0.763	0.717	1.09	45	66
7	3	709	0.426	0.121	0.222	0.343	0.308	0.449	49	52
8	3	722	ND	-	-	-	-	-	-	-
9	3	751	0.706	0.216	0.536	0.752	0.671	1.03	52	76

[1]: Assuming particles are spherical. [2]: Vapor pressure of KCl and $(KCl)_2$ calculated according to appendix B.
[3]: Calculated as $100 \cdot m_{wall}/m_{sat}$, where m_{sat} is for both KCl and $(KCl)_2$. [4]: Calculated as $100 \cdot m_{wall}/\Delta m_{pellets}$.

It is apparent from table 4.2 that it is difficult to conclude whether the carrier gas has been completely saturated in all experiments. The mass of KCl evaporated, $\Delta m_{pellets}$, is smaller than that indicated if the gas were saturated with both the monomer and dimer of KCl in the high KCl concentration (i.e. high saturator temperature) cases 3, 6, and 9, and is in fact better described by the calculation assuming only monomer formation. On the other hand, the evaporated mass is in excellent agreement with the calculated monomer and dimer estimate in the low KCl

concentration cases 1, 4, and 7. For the mid-temperature cases 2 and 5 this conclusion is also valid if case 2 is counted among the high concentration cases and 7 to the low.

The deviation between the mass of KCl evaporated and the mass detected in aerosol phase and wall condensate combined is less than ± 5% in all cases except in the low saturator temperature cases 1, 4, and 7, where a deviation between 15 and 25% is seen. The explanation for this discrepancy is at present unknown, but may be related to the assumption of spherical particles. This assumption may not be valid for case 1, 4, and 7. In view of the uncertainties in the interpretation of the above experiments, it is difficult to choose an estimate of the wall condensation percentage.

The SMPS measurements also yield the total number concentration at 20°C and the geometric mean diameter d_p in addition to the number size distributions shown in figure 4.5 to 4.13.The changes in these output values when the cooling rate and KCl inlet concentration is changed are shown in table 4.3 for all nine cases with the same values calculated by the simulations with MONAERO. The percentage of KCl which condenses on the tube wall is also shown for both experiment and simulation. The wall condensation percentage calculated as $100 \cdot m_{wall}/\Delta m_{pellets}$ is shown.

Table 4.3 *Results from LFAC experiments and MONAERO simulations with no seed nuclei. d_p is the geometric mean diameter. "% wall" is the percentage of total KCl entering the condenser which is collected on the inner tube wall.*

Case	Temperature profile	T_{sat} (°C)	Experiment			Simulation		
			Number concentration (cm^{-3})	d_p (μm)	% wall[1]	Number concentration (cm^{-3})	d_p (μm)	% wall
1	1	709	$2.7 \cdot 10^7$	0.132	51	$1.4 \cdot 10^7$	0.152	63
2	1	737	$4.4 \cdot 10^6$	0.313	62	$5.1 \cdot 10^6$	0.296	57
3	1	751	$3.3 \cdot 10^6$	0.356	62	$4.4 \cdot 10^6$	0.340	59
4	2	709	$1.7 \cdot 10^7$	0.152	48	$1.8 \cdot 10^7$	0.132	67
5	2	722	$1.6 \cdot 10^7$	0.192	79	$1.1 \cdot 10^7$	0.176	67
6	2	751	$9.9 \cdot 10^6$	0.252	66	$7.8 \cdot 10^6$	0.241	69
7	3	709	$3.0 \cdot 10^7$	0.117	52	$3.0 \cdot 10^7$	0.102	74
8	3	722	$2.4 \cdot 10^7$	0.162	ND[2]	$2.2 \cdot 10^7$	0.126	75
9	3	751	$8.3 \cdot 10^6$	0.263	76	$1.4 \cdot 10^7$	0.168	78

[1]: *Calculated as* $100 \cdot m_{wall}/\Delta m_{pellets}$. [2]: *ND: Not determined.*

The experiments with no seed nuclei yield number concentrations of submicron particles between $3.3 \cdot 10^6$ and $3.0 \cdot 10^7$ particles/cm^3 at 20°C with geometric mean diameters between 117 and 356 nm. Within each set of experiments with identical cooling rates the highest number concentration of particles is observed with the lowest saturator temperature, i.e. with the lowest concentration of gas phase KCl when cooling starts (cf. table 4.3). The opposite trend is seen in the geometric mean diameter, which increases when the saturator temperature is raised. Reducing the KCl concentration thus results in an increase in the production of submicron aerosol in terms of numbers. Furthermore, the particles produced from the lowest KCl concentration are smaller, close to 0.1 μm for all three temperature profiles. The mass concentration is however higher in the high KCl concentration cases, as the mass concentration increases with d_p^3. Judging from the simulated results, reducing the cooling rate apparently has the effect of increasing the fraction of KCl which condenses on the tube wall, resulting in smaller particles being formed. The explanation is a higher residence time in the condenser before homogeneous nucleation is initiated, cf. section 4.5. On the other hand, both simulations and experiments indicate that the total number concentration of submicron particles increases when the cooling lowered.

4.4 Comparison of experiments and simulations

As described in chapter 3, the expressions for calculation of homogeneous nucleation and particle growth depend on a number of physical parameters of KCl and the carrier gas, e.g. surface tension, vapor pressure etc. These parameters are all temperature-dependent, and the FORTRAN code MONAERO calculates them using component-specific temperature-dependent expressions from the literature. All parameter expressions are listed in appendix B. For lack of a better estimate, the sticking coefficient (section 3.3) is set arbitrarily to 1. At high temperature the vapor pressure of the dimer $(KCl)_2$ becomes significant, however, in these simulations the homogeneous nucleation rate is calculated assuming only the presence of monomeric KCl. The bulk value of the surface tension is used in the simulations, as the Tolman coefficient for solid KCl is not well determined (cf. appendix B). No fitting of physical or other parameters has been carried out.

Further input for the model are the relevant measured wall temperature profile and the saturator temperature, the LFAC dimensions, and the distribution of seed nuclei, if any. Finally the numerical parameters for the simulation are specified, i.e. the number of collocation points, the minimum step legth and the integration tolerance.

Some deviation between simulation and experiment is seen when the individual size distributions are inspected (figure 4.5 to 4.13), but on the whole the agreement is quite satisfying. The experimentally determined mean diameter and total number concentration are excellently

reproduced by the simulations, cf. table 4.3, in this case where no seed nuclei are present. Figure 4.14, 4.15, and 4.16 show the data from table 4.3 graphically. The deviations between measured and calculated values are modest, considering the uncertainty in the calculation of the nucleation rate and the degree of saturation obtained in the saturator section of the LFAC.

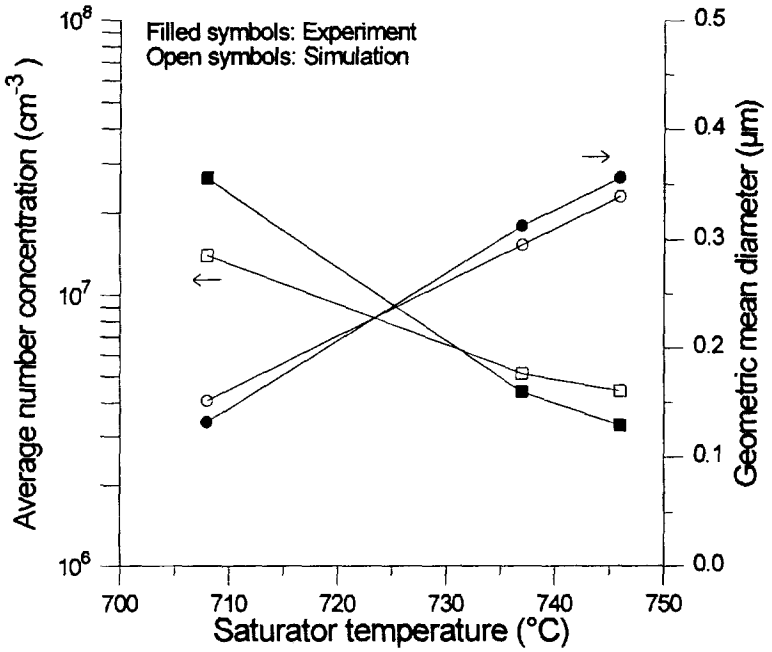

Figure 4.14 *Variation in average number concentration (at 20 C) and geometric mean diameter from SMPS measurements and MONAERO simulations. Case 1-3 of table 4.3, wall temperature profile 1.*

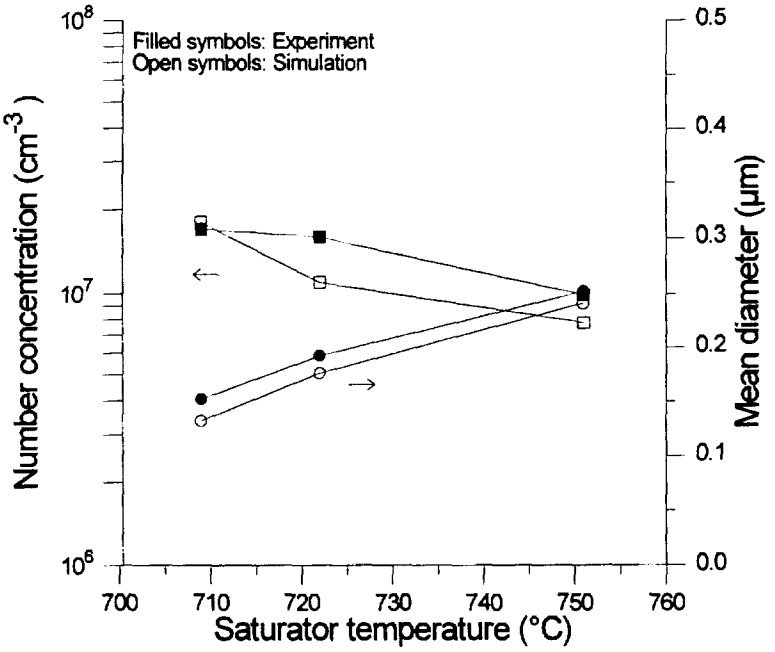

Figure 4.15 *Variation in average number concentration (at 20°C) and geometric mean diameter from SMPS measurements and MONAERO simulations. Case 4-6 from table 4.3, wall temperature profile 2.*

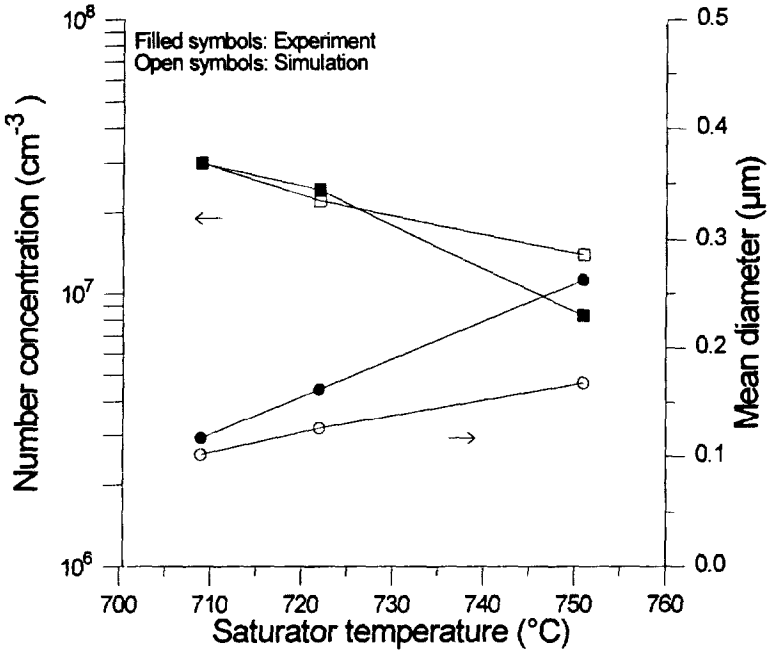

Figure 4.16 *Variation in average number concentration (at 20°C) and geometric mean diameter from SMPS measurements and MONAERO simulations. Case 7-9 from table 4.3, wall temperature profile 3.*

Not surprisingly, the agreement between experiments and simulations is less satisfying for wall condensation than for particle diameter and total concentration as a consequence of the uncertainties in the calculation of this parameter from the experiments.

4.5 Variation with cylindrical coordinates

In addition to the integrated results presented above, the simulations with MONAERO also provide the variation of important variables as a function of radius and axial position. These data make it possible to clarify the conditions under which homogeneous nucleation takes place. From table 4.1 it is apparent that the outlet number concentration increases with increasing cooling rate. Figure 4.17, 4.18, and 4.19 are three-dimensional plots of the variation in homogeneous nucleation rate (nuclei formed per m^3 per second) with axial and radial position for case 2, 5, and 8, which have similar saturator temperatures (i.e. KCl concentration prior to the onset of homogeneous nucleation), but different cooling rates. Table 4.4 shows the maximum nucleation rate from these simulations as well as the temperature and axial position at which the maximum is reached. In all three cases, the maximum nucleation rate is obtained at the tube center, and all data in table 4.4 are therefore for radius r=0.

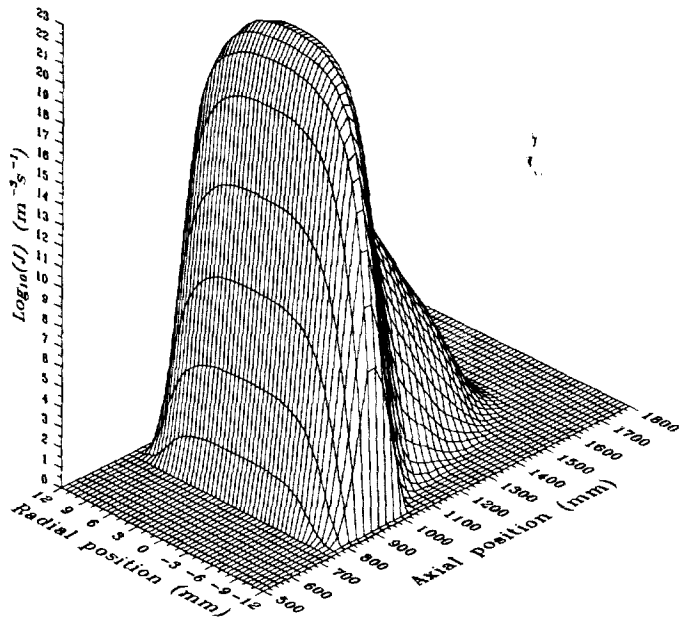

Figure 4.17 *Logarithm of homogeneous nucleation rate J as a function of radial and axial position, calculated by the MONAERO simulation code. Axial position = 0 mm corresponds to furnace inlet. Case 2 of table 4.1, wall temperature profile 1, T_{sat} 737°C.*

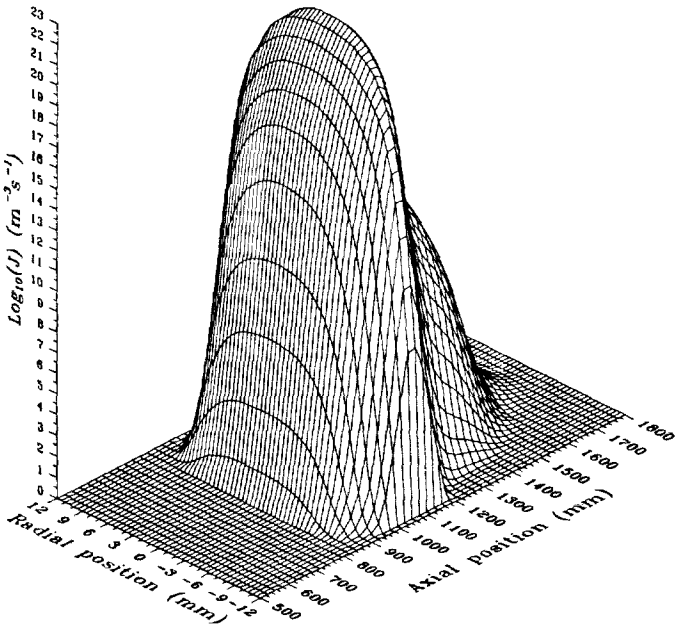

Figure 4.18 *Logarithm of homogeneous nucleation rate J as a function of radial and axial position, calculated by the MONAERO simulation code. Axial position = 0 mm corresponds to furnace inlet. Case 5 of table 4.1, wall temperature profile 2, T_{sat} 722°C.*

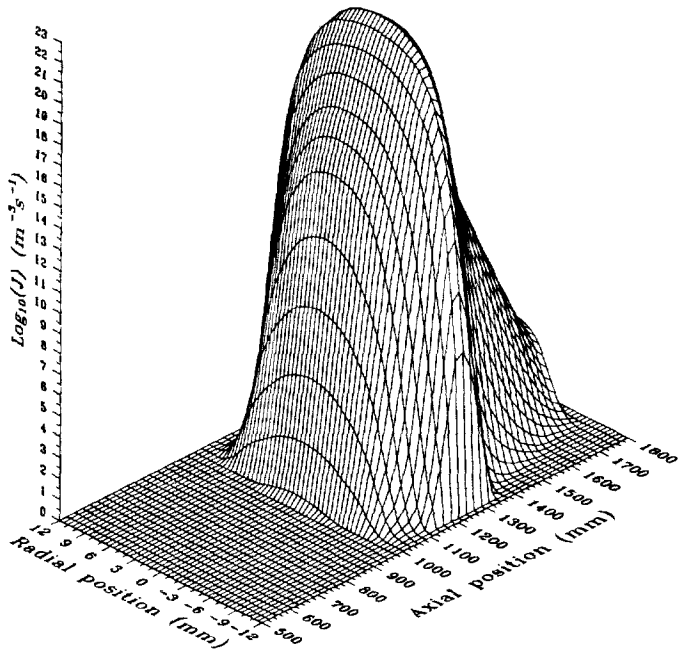

Figure 4.19 *Logarithm of homogeneous nucleation rate J as a function of radial and axial position, calculated by the MONAERO simulation code. Axial position = 0 mm corresponds to furnace inlet. Case 8 of table 4.1, wall temperature profile 3, T_{sat} 722°C.*

Table 4.4 *Maximum nucleation rate J_{max} occurring at axial position z_{max}, temperature T_{max} and saturation ratio s_{max}[1]. Results from simulations with MONAERO[2]. Z=0 corresponds to furnace inlet, z=1730mm to furnace outlet.*

Case	Temperature profile	T_{sat} (°C)	J_{max} ($m^{-3}s^{-1}$)	z_{max} (mm)	T_{max} (°C)	s_{max}[1]
1	1	709	$1.3 \cdot 10^{22}$	1057	589	3780
2	1	737	$4.0 \cdot 10^{22}$	1002	627	1172
3	1	751	$7.9 \cdot 10^{22}$	985	639	1003
4	2	709	$1.0 \cdot 10^{22}$	1174	581	6110
5	2	722	$1.6 \cdot 10^{22}$	1147	599	2520
6	2	751	$5.0 \cdot 10^{22}$	1101	630	1125
7	3	709	$1.0 \cdot 10^{22}$	1330	569	11945
8	3	722	$1.3 \cdot 10^{22}$	1306	585	5295
9	3	751	$3.2 \cdot 10^{22}$	1261	615	1486

[1]: *Saturation ratio defined as the ratio of the vapor pressure of KCl to the equilibrium vapor pressure of KCl.*

[2]: *Numerical parameters for simulations of table 4.4: 20 collocation points, minimum step length $5 \cdot 10^{-4}$m.*

Figure 4.17, 4.18, and 4.19 show that homogeneous nucleation begins abruptly and quickly reaches the maximum value listed in table 4.4. Since wall temperature profile 2 is lees steep than profile 1 (and profile 3 less steep than profile 2), the temperature where homogeneous nucleation is initiated is reached forther downstream in the condenser, i.e. at a higher *z*-value. The homogeneous nucleation rate is calculated by equation (3.21)-(3.24) of chapter 3, and depends strongly on the saturation ratio *s*. When the saturation ratio increases as a result of cooling, the equilibrium cluster concentration (3.24), i.e. the number of stable nuclei, increases extremely fast. Immediately after homogeneous nucleation is initiated, the rate of heterogeneous condensation also increases very rapidly when the large surface area of the newly formed nuclei becomes available. This leads to a decrease in saturation ratio as the KCl concentration is reduced, thus effectively killing off any further birth of new nuclei. The nucleation rate does not fall as abruptly as it increased, since the saturation ratio will continue to be greater than unity as a result of the continuing cooling. The maximum homogeneous nucleation rates listed in table 4.4 lie between $1.0 \cdot 10^{22}$ and $7.9 \cdot 10^{22}$ $m^{-3}s^{-1}$, and the maximum is reached at an axial position of approximately 1000 mm for profile 1, 1100 mm for profile 2, and 1300 mm for profile 3. The highest rate is obtained when the KCl concentration is high, and when the cooling is fast. Homogeneous nucleation takes place in the temperature range 550-650°C.

It is now possible to combine the information in table 4.3 and 4.4 to explain the increase in particle concentration indicated by both experimental and simulated results when the initial KCl level is lowered. As mentioned above, a competition between homogeneous nucleation and heterogeneous condensation takes place as soon as the new nuclei are formed. This mechanism is valid for all cases, however, in the cases where the KCl level is lower, homogeneous nucleation occurs at a lower temperature, (cf. table 4.4) and the subsequent growth rate by heterogeneous condensation, which depends on temperature, is correspondingly lower. Homogeneous nucleation is therefore allowed to continue longer than in the high-KCl case. This also explains the increase in total concentration observed when the cooling rate is decreased, which also results in homogeneous nucleation occurring at a lower temperature.

4.6 The influence of seed nuclei on homogeneous nucleation

In most real combustion systems a competition between homogeneous and heterogeneous condensation of alkali and other volatile species exists, since particles will be be present at the temperature where the condensation processes are initiated. These particles are formed by homogeneous nucleation of refractory elements already in the flame zone of the furnace and from mineral inclusions in the coal released after char burnout (cf. chapter 1). All of the above experiments are performed under initially particle-free conditions, and heterogeneous condensation on particles is of course only possible after new nuclei are formed. In order to

examine the behavior of KCl condensation in the presence of seed nuclei, a number of experiments are performed in which the inlet concentration of particles is varied systematically.

The number size distribution of the seed particles and the aerosol at the outlet is measured as described in chapter 2. An average of 3-5 inlet and outlet size distributions are measured with the SMPS system for each concentration of seed particles. An example of an inlet size distribution is shown in figure 4.20. The inlet number concentration in these experiments is varied between 10^3 and 10^6, and the geometric mean diameter of the seed nuclei is in the range 70-110 nm. In each of the cases 1-2, 4-5, and 7-8 the addition of seed nuclei in a concentration below some critical value results in the formation of a large number of particles by homogeneous nucleation. A sudden change in the measured outlet concentration is observed when the seed nuclei concentration exceeds this critical value, resulting in a drop in outlet concentration of close to two orders of magnitude. Increasing the seed nuclei concentration from this point on has no effect on the outlet concentration, as all KCl present in the gas phase apparently condenses on the seep particle surface. For all conditions investigated in this study, homogeneous nucleation can be suppressed by the addition of seed nuclei in a concentration of approximately 10^5 particles per cm^3. In the cases where homogeneous nucleation is suppressed, the heterogeneous condensation of KCl on the seed particles often causes them to exceed the upper detection limit of the SMPS system of 0.8 μm. An example of a measured outlet number size distribution is shown in figure 4.21. In this case, homogeneous nucleation is partially suppressed, and both homogeneously nucleated particles and the seed nuclei, which now have grown to approximately 0.25μm in mean diameter, are within the SMPS detection range.

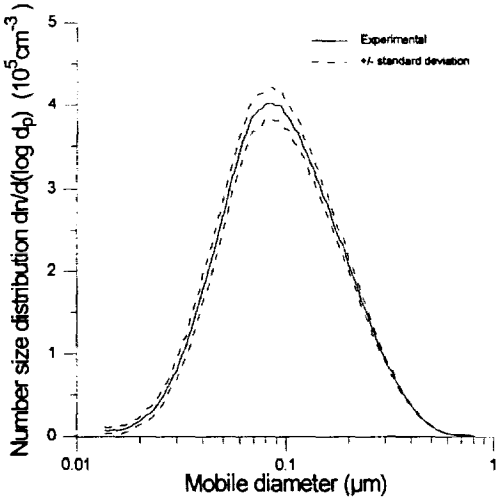

Figure 4.20 *Typical size distribution of seed nuclei. Number concentration at 20°C 10^5 cm^{-3}, geometric mean diameter 0.1 μm. Average of 3 SMPS measurements.*

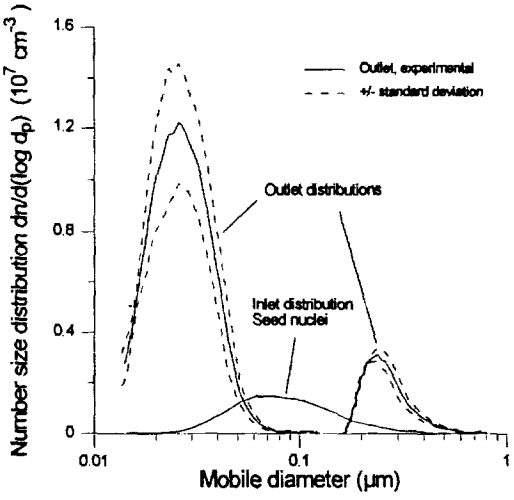

Figure 4.21 *Outlet size distribution of homogeneously nucleated particles and seed nuclei. Wall temperature profile 2, T_{sat} 709°C. Inlet seed nuclei number concentration $9.2 \cdot 10^5 cm^{-3}$ at 20°C, mean diameter 100 nm.*

At the other extreme, homogeneous nucleation can be completely suppressed when all available KCl condenses on the seed nuclei, as shown in figure 4.22. The result of the same temperature settings and a lower inlet concentration is shown in figure 4.23.

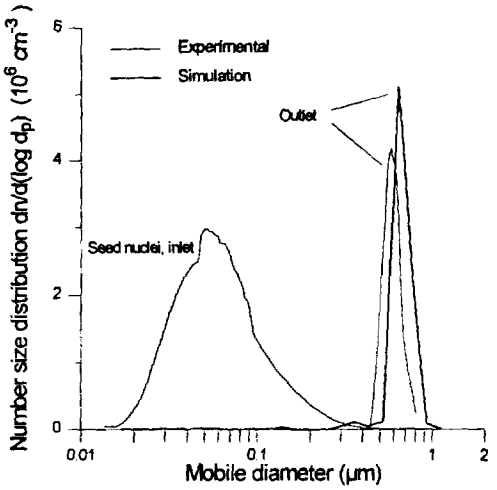

Figure 4.22 *Outlet size distribution with suppression of homogeneous nucleation. Wall temperature profile 2, T_{sat} 722°C. Inlet seed nuclei concentration $6.5 \cdot 10^5$ cm^{-3}, mean diameter 70 nm.*

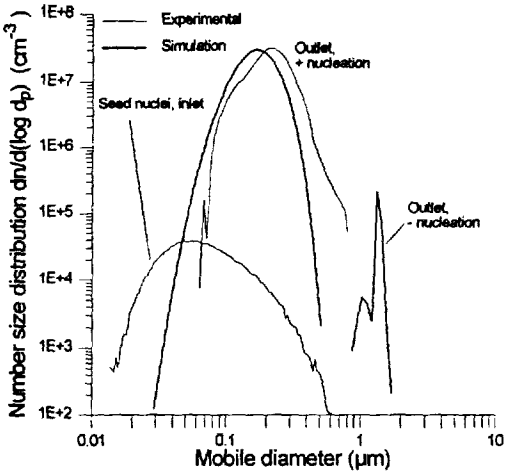

Figure 4.23 *Outlet size distribution with homogeneous nucleation. Wall temperature profile 2, T_{sat} 722°C. Inlet seed nuclei concentration $1.1 \cdot 10^4$ cm^{-3}, mean diameter 80 nm.*

The outlet size distributions from the simulations are all based on measured seed particle distributions, corrected for the loss of particles in the pellet layer as described in chapter 2.

In order to identify the critical seed nuclei concentration , the average number concentration of particles exiting the LFAC has been calculated with MONAERO, and is shown in the following as a function of the average number concentration of seed particles for case 1-2, 4-5, and 7-8. Measured inlet concentrations are again used as input for the simulations, where the number of particles in each size sections of the distribution has been multiplied by a constant factor in order to increase the total concentration. A dashed line corresponding to an outlet concentration identical to the inlet concentration is shown in all plots. In figure 4.24, 4.25, and 4.27 part of the measured outlet distribution is outside the SMPS detection limits. From the SMPS size distributions it is estimated that the real outlet number concentration in no case is more than twice the measured number concentration. In figure 4.28 the measured size distributions leading to the framed data points are below the detection limit of the SMPS system, and it is more difficult to estimate the real number concentration. However, the deviation is estimated to be less than one order of magnitude.

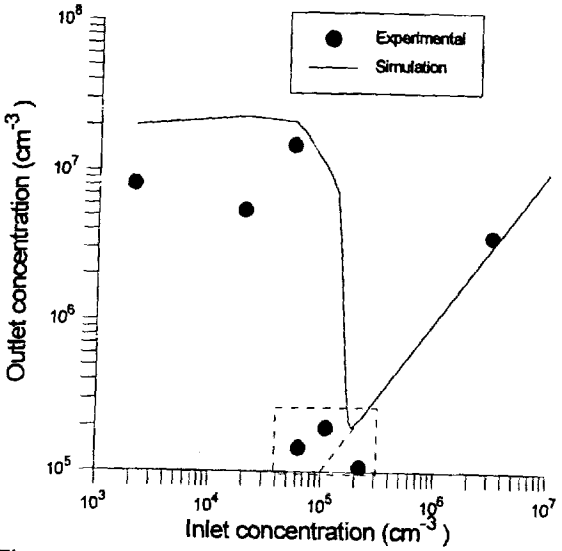

Figure 4.24 *Outlet concentration as a function of inlet concentration of seed nuclei. Case 1 of table 4.1, wall temperature profile 1, T_{sat} 709°C. Boxed data points are incomplete, some particles are outside the detection range of the SMPS system*

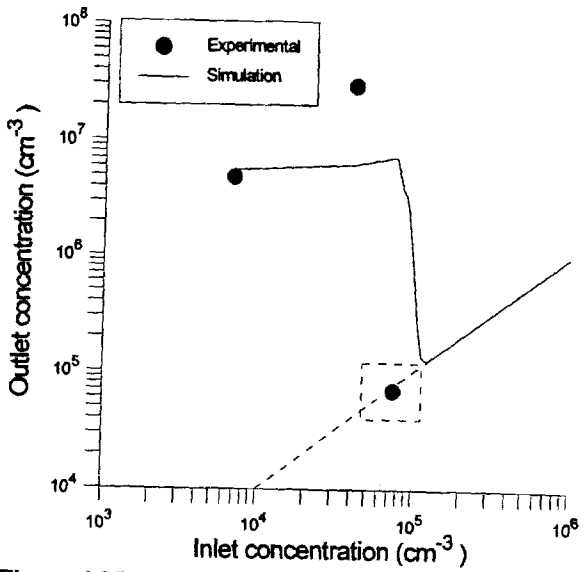

Figure 4.25 *Outlet concentration as a function of inlet concentration of seed nuclei. Case 2 of table 4.1, wall temperature profile 1, T_{sat} 737°C. Boxed data points are incomplete, some particles are outside the detection range of the SMPS system*

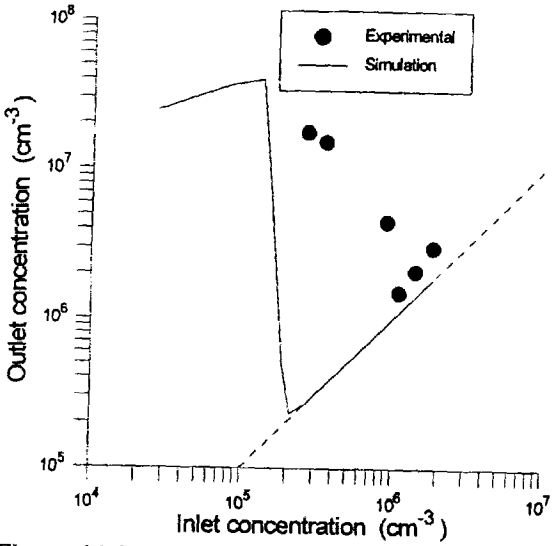

Figure 4.26 *Outlet concentration as a function of inlet concentration of seed nuclei. Case 4 of table 4.1, wall temperature profile 2, T_{sat} 709°C.*

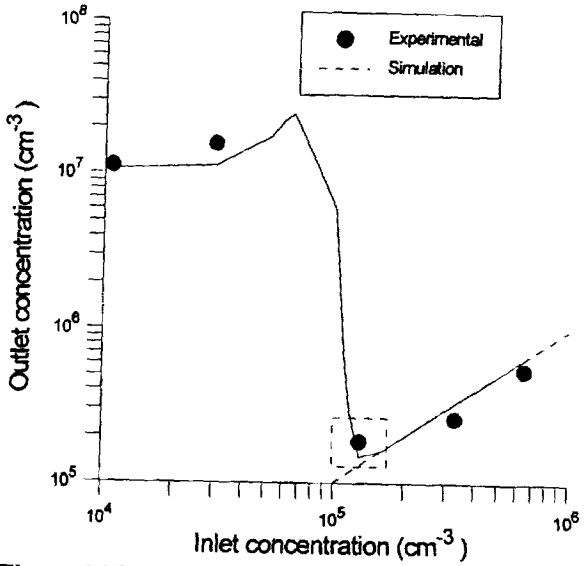

Figure 4.27 *Outlet concentration as a function of inlet concentration of seed nuclei. Case 5 of table 4.1, wall temperature profile 2, T_{sat} 722°C. Boxed data points are incomplete, some particles are outside the detection range of the SMPS system*

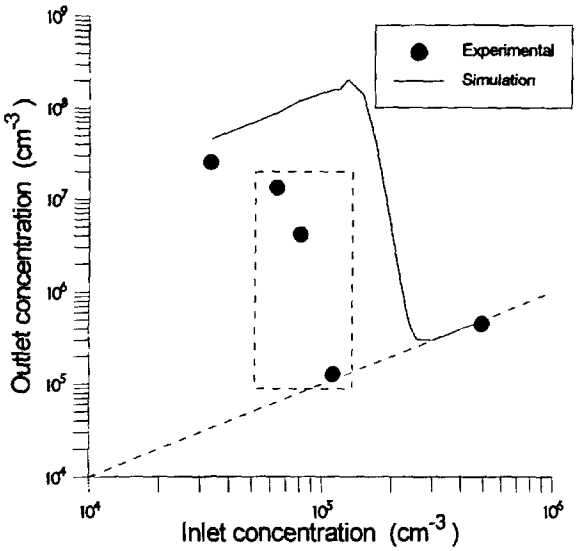

Figure 4.28 *Outlet concentration as a function of inlet concentration of seed nuclei. Case 7 of table 4.1, wall temperature profile 3, T_{sat} 709°C. Boxed data points are incomplete, some particles are outside the detection range of the SMPS system*

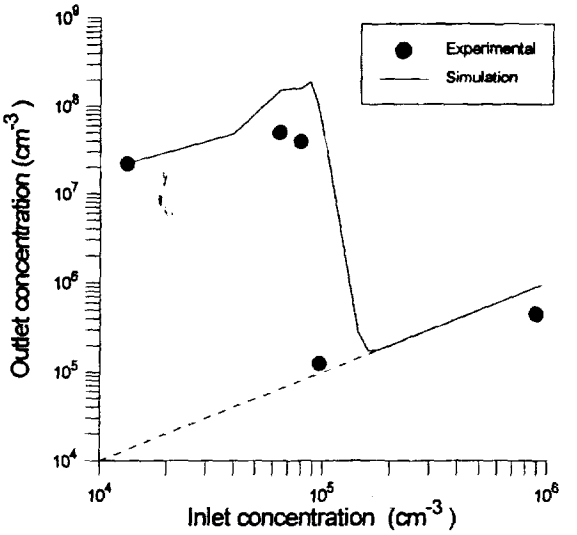

Figure 4.29 *Outlet concentration as a function of inlet concentration of seed nuclei. Case 8 of table 4.1, wall temperature profile 3, T_{sat} 722°C*

The results from the experiments and simulations with seed nuclei addition show the characteristic response of homogeneous nucleation of KCl to the presence of foreign nuclei. The number of particles formed is virtually unaffected by the seed particles until the inlet concentration of nuclei exceeds the critical value. There is no apparent correlation between the seed concentration necessary for suppression and process parameters such as saturator temperature (i.e. KCl concentration) or cooling rate. In most real pulverized fuel or biomass combustion systems a concentration of particles less than 10^5 cm^{-3} at the temperature of approximately 600°C where homogeneous nucleation of KCl begins will be rare. It must therefore be expected that condensation of KCl will take place entirely on particles already present in the gas phase. This conclusion can be completely changed by any occurrence of chemical reaction such as the sulphation reaction discussed in chapter 1.

Figures 4.24 to 4.29 show a fair agreement between simulated and experimental results. When determining the number of particles necessary to suppress homogeneous nucleation, the predictions of the simulation are excellent for case 1, 2, 5, and 8 (figures 4.24, 4.25, 4.27, and 4.29), while the simulation underestimates the onset of nucleation suppression in case 4 (figure 4.26) and overestimates it in case 7 (figure 4.28).

4.7 Gas temperature profile

The derivation of the model implemented in MONAERO uses a number of assumptions as described in chapter 3. In order to check the validity of the temperature calculations, a simulation using the computational fluid dynamics (CFD) software package FLUENT has been carried out. The equations governing heat and mass transfer in FLUENT are described in appendix C. The gas temperature calculated by both FLUENT and MONAERO is depicted in figure 4.30.

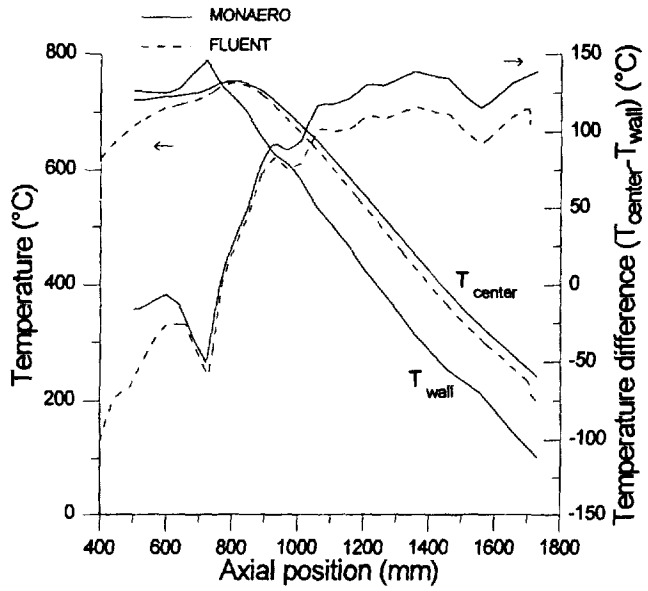

Figure 4.30 *Center and wall temperature profile and difference between wall and gas center temperature in the LFAC as a function of axial position. Results from simulations using the MONAERO and FLUENT programs.*

From the figure it can be concluded that the assumptions made in MONAERO regarding heat transfer are quite reasonable. The small difference in the center temperature between the two models can be explained by the assumption in MONAERO that convective heat transfer is negligible. The calculated center temperature will therefore be slightly overestimated compared to FLUENT, which includes convective heat transfer. Both simulations show a significant temperature gradient in radial direction. The difference between wall and gas center temperature is close to zero at the condenser inlet (axial position approximately 800 mm), and rises above 100 degrees when the gas center temperature reaches 600°C. The relatively large radial temperature gradient will lead to a convective flow in radial direction, which makes neglecting of radial velocity in the derivation of MONAERO somewhat less valid. The difference is approximately 10 degrees in the temperature range from 700 to 600 °C, where homogeneous nucleation takes place. In the lower sections of the condenser the difference between FLUENT and MONAERO center temperature is approximately 25 degrees, which is insignificant in this part of the condenser. The comparison of center temperatures from MONAERO and FLUENT does

however show that the deviations are acceptable, in view of the uncertainties of the theoretical description of homogeneous nucleation. Temperature distribution plots of the gas phase as calculated by FLUENT are shown in appendix C.

5. Design of field equipment

As described in the introduction (cf. chapter 1), using biomass as a fuel for power and heat generation is recommended by the Danish government. One possibility for large-scale utilization of straw, which is the most abundant biomass fuel in Denmark, is co-combustion with coal. As a first step, the consequences of implementing such a technology must be investigated. This includes plant performance, economy, and the previously discussed potential for increased problems with slagging, fouling, corrosion, and emission of submicron particulate matter. The present work describes measurements of the particles in the flue gas, intended to gain new insight int particle formation processes as a function of fuel load, composition and the utilization of straw as a fuel.

5.1 The MKS1 Demonstration program

The power company Midtkraft I/S has initiated a two-year demonstration program at unit 1 of the Studstrup Power Station near Aarhus, Denmark to evaluate the consequences of co-firing coal and straw in a utility boiler. A 380 MW_{th} wall-fired pulverized coal unit originally built in 1968 has been reconstructed to allow co-combustion of coal and straw. Straw is received as Hesston bales with dimensions 1.2 × 1.3 × 2.4 m and subsequently separated and ground to a length of less than 30 or 50 mm in four parallel hammer mills. From the reception and pre-treatment plant the straw is transported to the boiler in four 450 m long pneumatic tubes. The converted boiler has three rows of four burners each, and the straw is injected with coal and primary air in the four middle burners. Our part of the demonstration program was carried out in the spring of 1996 and 1997. In the 12-week measurement campaign total boiler load and the amount of straw co-fired is varied systematically according to table 5.1.

Table 5.1. Operating conditions in the MKS1 in-situ test program.

		Straw % (of total energy input)		
	Boiler load[2]	0 %	10 %	20 %
Coal type A	50 %	Series 7	-	Series 1
	75 %	Series 6	-	Series 2
	100 %	Series 5	Series 4	Series 3, 3a[1]
Coal type B	70 %	Series 8	-	-
Coal type C	100 %	Series 8a	-	Series 9a

[1]: Series 3a, 8a, and 9a measured in January 1997. [2]: Percent of total boiler load of 380 MW_{th}.

Several investigators from the Technical University of Denmark and Midtkraft I/S are involved in the in-situ measurement campaign, which includes gas phase analysis, alkali measurements, furnace temperature profile measurements, studies of fly ash deposition and composition, stack emissions, and aerosol measurements. The measurement positions of the various investigators are indicated on figure 5.1. Furthermore, samples are collected every 20 minutes from coal, straw, bottom slag and fly ash from the electrostatic precipitator. These samples are analyzed by the laboratory at Studstrup Power Station.

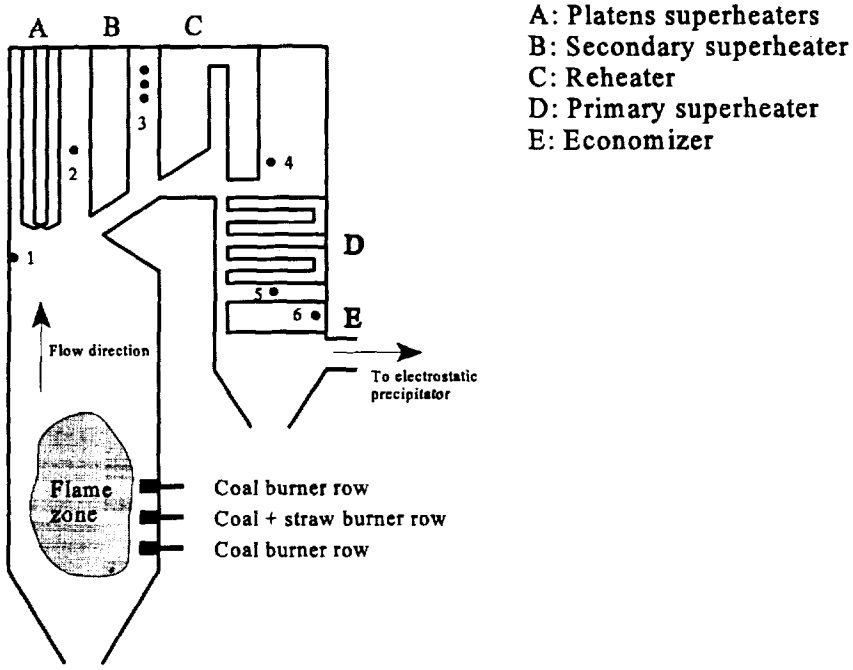

Figure 5.1 *Schematic of the reconstructed boiler unit 1 at Midtkraft Power Station. A-E indicate heat transfer surfaces. 1-5: Sampling positions for deposits, flue gas, alkali, fly ash particles, and temperature measurements. 6: Aerosol measurement position.*

Aerosol measurements are performed upstream from the electrostatic precipitator. Flue gas contains water vapor and other condensible components, as well as particles in high number concentration, and steps must be taken to prevent condensation and excessive coagulation during aerosol sampling. Other investigators have used in-stack sampling, where an impactor is placed inside the flue gas channel at a temperature of 130-140°C (Kauppinen and Pakkanen, 1990, Kauppinen et al., 1996). This method minimizes particle loss in the sampling line, but requires high thermal stability of the substrate coatings. A different method uses drying of the aerosol sample prior to characterization (Christensen, 1995). Water condensation is avoided, but the results must be corrected for particle loss in the drying system. A third possibility is lowering the dew point of the aerosol sample by dilution with dry inert gas (McCain et al., 1975, Markowski

et al., 1980, Joutsensaari et al., 1992). Dilution must be carried out above the dew point of water, and a method for measuring the dilution ratio must be devised. In the present work, the flue gas temperature is approximately 350 °C, which is somewhat higher than the 120°C previously used by our laboratory in field measurements of aerosols from pure straw combustion (Christensen, 1995). Therefore we decided to use the method of dilution, and a novel high-temperature dilution ejector probe was designed (figure 5.3).

An overview of the sampling equipment is shown in figure 5.2. Flue gas is withdrawn from the duct between the two banks of the economizer (see figure 5.1), perpendicular to the direction of flow. This prevents the largest of the fly ash particles from entering the probe and clogging up the capillary sampling tube (appendix D) at the tip of the probe (cf. figure 5.3).

The flue gas sample is mixed with 35 l/min of filetered air at the flue gas temperature immediately upon entry into the probe. The impactor pump withdraws a sample, which either enters the impactor or bypasses it when impactor foils are replaced. This ensures that the residence time in the sampling system remains unchanged even when the impactor is inactive. A second, smaller pump supplies samples to the SMPS (scanning mobility particle sizer) system, the TEM (transmission electron microscopy) sampling, and the humidity measurements.

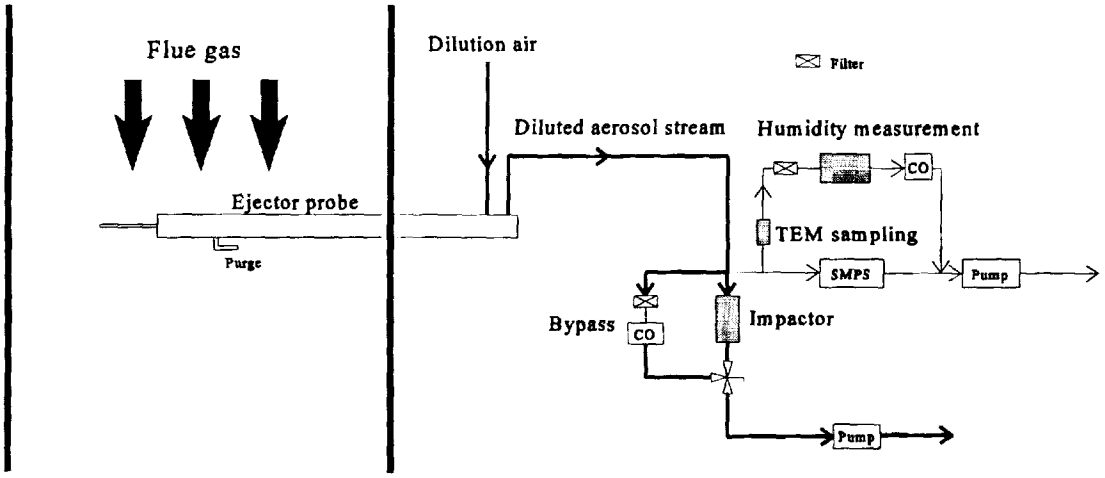

Figure 5.2 *Schematic of the sampling system.* ***SMPS****: Scanning mobility particle sizer system.* ***TEM****: Transmission electron microscopy.* ***CO****: Critical orifice.*

5.2 The ejector probe

The purpose of the probe (see figure 5.3 and) is to withdraw a well-defined sample of gas from the flue gas duct and to dilute it immediately upon entry in the probe. The probe should also be able to operate continuously for several hours without cleaning or other maintenance. It was designed in cooperation with Lars Skaarup Jensen as part of his masters project. The ejector suction, caused by the flow of dilution air in the ejector head (figure), withdraws a well-defined amount of flue gas through the capillary tube. Dry, filtered dilution air is heated in the outermost annulus by counterflowing diluted aerosol stream and the flue gas, keeping the ejector head at the flue gas temperature. Immediately after entering the probe, gas sample and dilution air is mixed, and the dew point of the mixture is lowered. Thus, the potential influence of both water condensation and aerosol agglomeration is much reduced. The diluted sample is cooled by counterflowing dilution air and further by a water-cooled tubular insert.

The probe is inserted in the flue gas channel perpendicular to the direction of flow. Due to their inertia, some of the larger fly ash particles are unable to follow the gas into the probe, and the probe placement thus ensures that clogging of the capillary tube and overloading of the upper stages of the impactor is less likely to occur (cf. section 5.7).

If SO_3 is present in the flue gas, a sulfuric acid aerosol can be formed, since the moist air in the probe can easily hydrolyze SO_3 to H_2SO_4, which can subsequently nucleate homogeneously. Such an artificial aerosol could lead to misinterpretation of the results. Therefore, the tip of the probe has been fitted with a SO_3 denuder in some experiments. The denuder consists of porous hollow ceramic cylinders. These have been soaked in a solution of $CaCO_3$ and dried before placement in a steel tube mounted on the probe tip. The flue gas sample thus has to pass through the tube, and SO_3 in the flue gas reacts with the $CaCO_3$ to form $CaSO_4$(s).

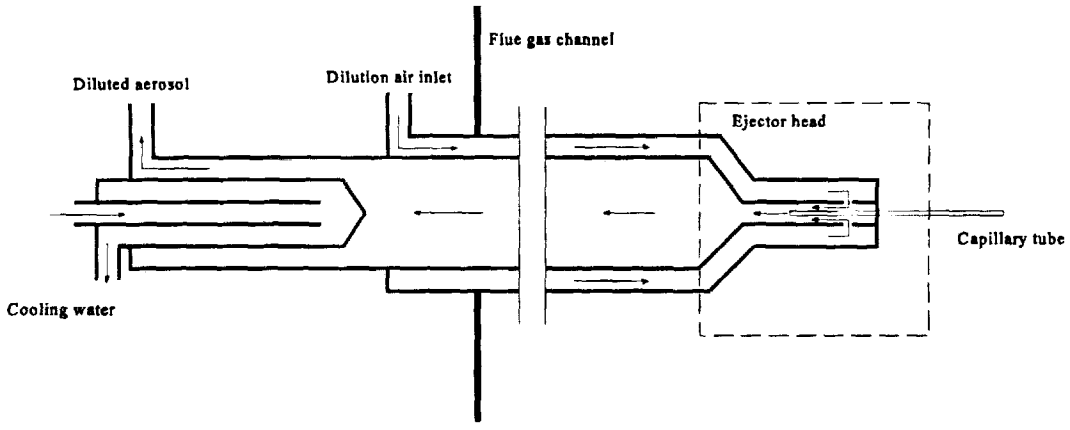

Figure 5.3 Schematic of the ejector probe.

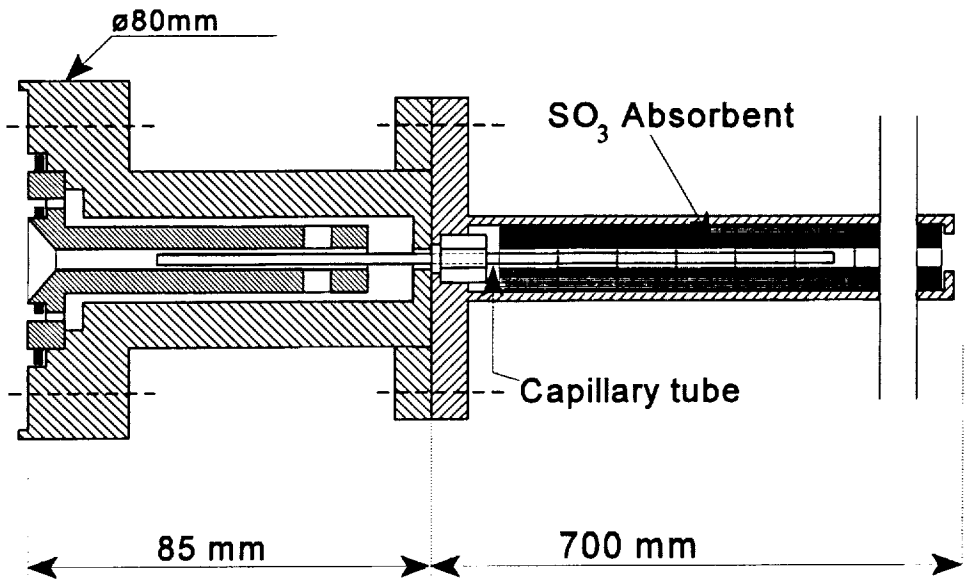

***Figure 5.4** Detailed drawing of the ejector head*

5.3 Humidity measurements

The exact sample flow entering the ejector probe is unknown, and therefore an independent method is used to calculate the dilution ratio defined as the ratio of sampling flow plus dilution air flow to the sampling flow. The method consists of two separate, simultaneous measurements of the water content of flue gas and diluted sample stream, respectively. Figure 5.4 shows the setup for measuring the water concentration in the undiluted flue gas. Undiluted flue gas at ambient temperature (which in this case means 32 °C) and pressure is withdrawn from the flue gas channel at a rate of 0.6 l/min and filtered by a quartz wool filter. It is dried by passing through a ½" stainless steel tube containing 55-60 g of drying agent (CECA zeolites, 3 Å). A constant flow is secured by using a critical orifice. The sampling line from the flue gas channel to the ½" tube is kept at 80°C to prevent premature water condensation. After a sampling period of approximately 60 minutes, the zeolite spheres are transferred quantitatively to an airtight container by opening the valve V in figure 5.4 and weighed. The mass increase is due solely to uptake of water, and the humidity of the flue gas can be calculated from knowledge of sampling time, gas flow, and the mass of water absorbed.

The water content of the diluted aerosol sample is analyzed in a side stream to the impactor and SMPS measurements (cf. figure 5.2) using a Cermet hygrometer (Michell Instruments) which measures the dew point of the gas. The hygrometer was calibrated between each series by a

method similar to the flue gas humidity measurements described above. Unfortunately, this instrument was not sufficiently robust to cope with the conditions in the diluted flue gas, and some measurements had to be discarded.

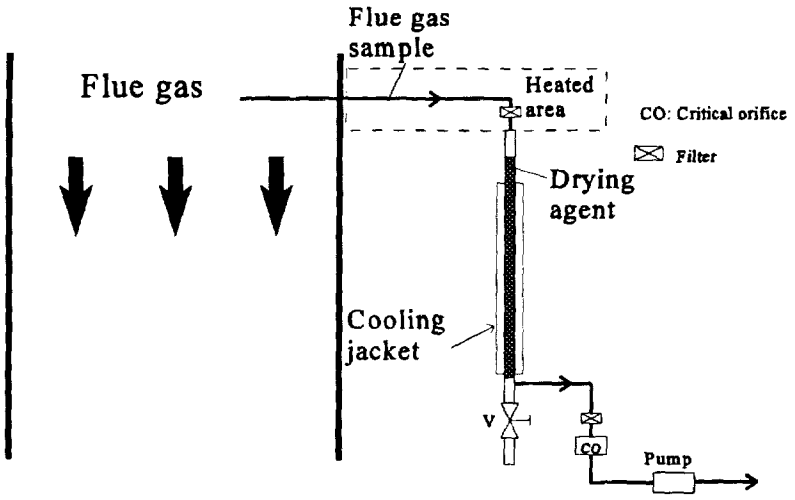

Figure 5.5 *Schematic of flue gas water content measurement. Measurements are carried out simultaneously with measurements of diluted sample humidity.*

5.4 The SMPS system

Particle number size distributions from the diluted flue gas sample are measured by the SMPS (scanning mobility particle sizer) system. The system in these measurements consists of a TSI model 3071 DMA (differential mobility analyzer) and a TSI model 3022 CPC (condensation particle counter). The setup and internal flows of the SMPS system are identical to those in the laboratory, cf. chapter 2.

5.5 The impactor

The main part of the diluted flue gas sample is analyzed using a Berner-type multijet low pressure impactor (Hauke model LPI 25/0.018/2). This device separates the particles according to their aerodynamic diameter by forcing the sample through 11 stages with increasing gas velocity. At a given stage, a fraction of the particles are unable to follow the gas to the next stage due to their inertia, and are collected on a receptor foil. The aerodynamic diameter of the particles which have a calculated impaction probability of 50% is called that stage's aerodynamic cut-diameter $d_{c,ae}$. The upper stages of the impactor operates at ambient pressure, whereas the pressure at the lower stages is reduced to improve separation of small particles. The flow through the impactor is kept at 24.4 l/min at 20°C and atmospheric pressure by a critical orifice, and the pressure downstream of the orifice is kept below 42 mbar by a large pump. The collected

particles may be subjected to chemical, gravimetric, and electron-microscopic analysis.

In this study, two different types of foils are used: Aluminum for gravimetric and chemical analysis and copper for analysis by EDX (energy-dispersive x-ray analysis). All copper and half the aluminum foils were coated with a thin layer of Apiezon H high-vacuum grease to minimize particle bounce and to improve substrate stability during handling and transport. The grease was applied by spreading a 2.5% (w/w) solution of Apiezon H in toluene in a circular pattern on the foils. After evaporation of the toluene, a flat layer of 0.3-0.5 mg of grease is left on the foil surface. All foils are weighed on a Sartorius M3P-000V 001 microbalance with a readability of 1 μg for the aluminum foils and 5 μg for the heavier copper foils.

The impactor separates the particles according to their aerodynamic properties. The results from the impactor measurements are therefore reported in terms of the aerodynamic diameter, which is not the same as the actual particle diameter. Aerodynamic diameter is defined as that of a sphere with density 1 g/cm^3 with the same rate of gravitational sedimentation as those deposited. As a consequence, the actual diameter of a particle collected on a given stage depends on the particle density. This is shown for some selected densities in table 5.2.

Table 5.2 Characteristics of the Berner low pressure impactor. Mean diameter d_{ae} of particles deposited on impactor stages as a function of particle density. The calculations assume that particles are spherical.

Impactor stage	Aerodynamic diameter	Diameter as a function of density			
		d_c (0.5 g/cm^3)	d_c (2 g/cm^3)	d_c (3 g/cm^3)	d_c (4 g/cm^3)
	μm	μm	μm	μm	μm
1	0.0253	0.0500	0.0127	0.0085	0.0064
2	0.050	0.095	0.0255	0.0171	0.0129
3	0.098	0.175	0.053	0.0359	0.0272
4	0.194	0.307	0.116	0.084	0.066
5	0.382	0.57	0.249	0.190	0.155
6	0.75	1.10	0.51	0.404	0.341
7	1.49	2.14	1.03	0.83	0.71
8	2.93	4.18	2.05	1.66	1.43
9	5.8	8.2	4.06	3.30	2.85
10	11.4	16.2	8.0	6.5	5.7

Even though the inertial filtering at the probe entrance caused by the 90° angle between gas flow and probe excludes most of the large particles, the very high mass concentration of these particles

results in a significant mass loading even on stages 7-10.

5.6 TEM sampling

Particles are collected on 300 mesh nickel grids 3 mm in diameter for morphology analysis by TEM (transmission electron microscopy). The grids are placed in a ¼" tube tee inserted in the humidity measurement sampling line (cf. figure 5.2 and chapter 5.6) upstream of the filter. Since the deposition mechanisms, primarily diffusion and impaction, are strongly dependent on particle size, the distribution of particles collected are not representative of the aerosol. Particles in the size range from 0.1-1.0 μm are expected to be collected with a low efficiency. A sampling time of 1-2 hours is sufficient to collect an appropriate number of particles on each grid.

5.7 Characterization of the field equipment

The sampling probe is designed to minimize the effect of processes which alter the aerosol size distribution and composition. However, any aerosol in a flow system will change with time due to diffusional and inertial deposition, sedimentation, thermophoresis, etc. Of these changes occurring inside the probe, only diffusional losses are expected to be of importance to the particle size range investigated in this work, since the residence time in the probe is less than two seconds.

The distribution of particles which enter the probe is not identical to the fly ash particle distribution. The placement of the probe perpendicular to the direction of flue gas flow results in an inertial filtering of the larger particles. This effect is described in further detail in appendix D. The result of this filtering is illustrated by figure 5.5 showing the penetration defined as the ratio of the number of particles of a given size which pass through the probe to the number of particles entering. Figure 5.5 shows that the inertial filtering does not affect particles with diameters less than 0.2 μm, and that 90 % of the particles less than 1 μm in diameter enter the probe.

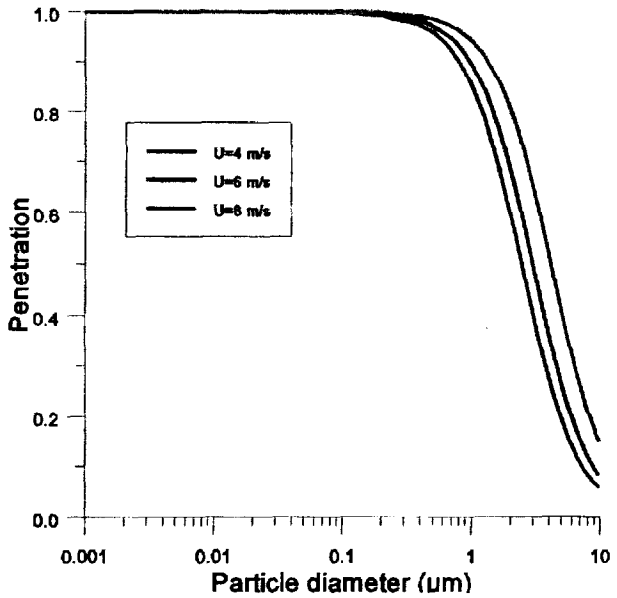

Figure 5.6 Calculated penetration of particles in probe tip placed perpendicular to the direction of flow in the flue gas channel.

Measurements performed with the SMPS system are therefore assumed to be unaffected by the inertial filtering at the probe inlet. Results from the impactor measurements are however strongly influenced by this effect, but the filtering is not expected to affect the distribution of species of the particles collected. The particles collected on the stages of the impactor are therefore assumed to be representative of the fly ash.

As seen in figure 5.3, the aerosol passes through a number of restrictions and tubes before being analyzed in the SMPS system or the impactor. Particle loss depending of particle size is expected to occur, and a penetration $P(d_p)$ of particles is determined, where

$$P(d_p) = \frac{\varphi_a(d_p, exit)}{\varphi_a(d_p, inlet)} \tag{5.1}$$

Here d_p the particle diameter, and φ_a the aerosol size distribution independent of temperature referred to a density ρ_r. A penetration of 1 means that the aerosol is unchanged by passing through the probe.

Ideally, the penetration should be determined under conditions identical to those used during the field measurements. However, it is more practical to measure the penetration under controlled laboratory conditions at room temperature. Additionally, calculations are performed to determine the penetration theoretically. If the two are in good agreement, the calculations can then be performed using the conditions from the field. In the laboratory measurements of the penetration an aerosol is generated from a solution of NaCl in a TSI model 3076 atomizer, and a fraction

thereof dried in two serial diffusion driers. The aerosol size distribution is measured upstream and downstream from the probe under identical conditions, and the penetration calculated from equation 5.1, where φ_a is a weighted average of at least four measurements. The results are uncertain for values of d_p far from the size distribution peak, and therefore several concentrations of NaCl are used to cover the relevant particle size range. The measurements are described in further detail in appendix D.

For the purpose of determining the theoretical penetration, it is assumed that particle losses due to diffusion in the sampling line occur in the capillary tube (A), cf. figure 5.7, the upper probe tube (B), the annulus at the cooling insert (C), and in two Tygon tubes leading the aerosol from the probe to the SMPS system (D and E).

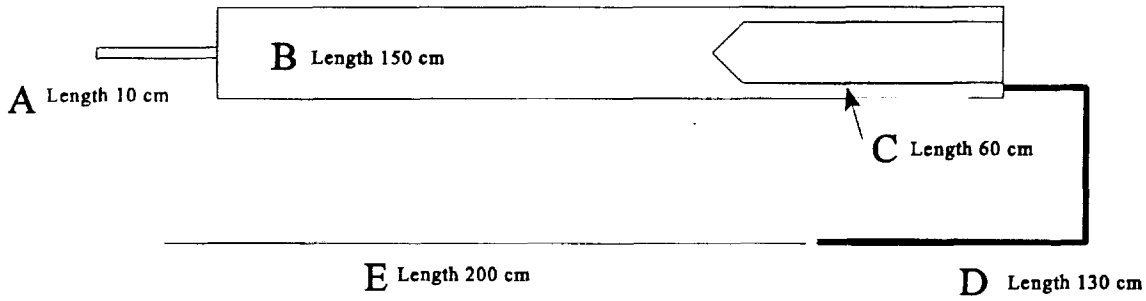

***Figure 5.7** Schematic of probe geometry as assumed for penetration measurements in the laboratory. **A**: Capillary tube. **B**: Upper probe tube. **C**: Annulus at cooling insert. **D, E**: Tygon tubes, 7/8" and 1/4" outer diameter, respectively. In field experiments, tube D is 100 cm long, and tube E is not used.*

The penetration in sections A, B, D, and E are calculated from a model for diffusional loss in a straight cylindrical tube with laminar flow and a particle concentration of zero at the tube wall, and the corresponding loss in section C from a model for laminar flow in an isothermal straight slit. In sections A, B, C, and E, the Reynolds number is well below the limit for laminar flow. In section D, the Reynolds number is approximately 2200, and laminar flow is assumed. For further details, see Appendix D. From figure 5.8, which shows the penetration in individual sections as well as the total penetration, it is clear that for particles above 0.05 μm the penetration is quite close to 100 %. It is also seen that the diffusional losses occur predominately in the annulus (C) and the longer of the Tygon tubes, which is not used in the field experiments.

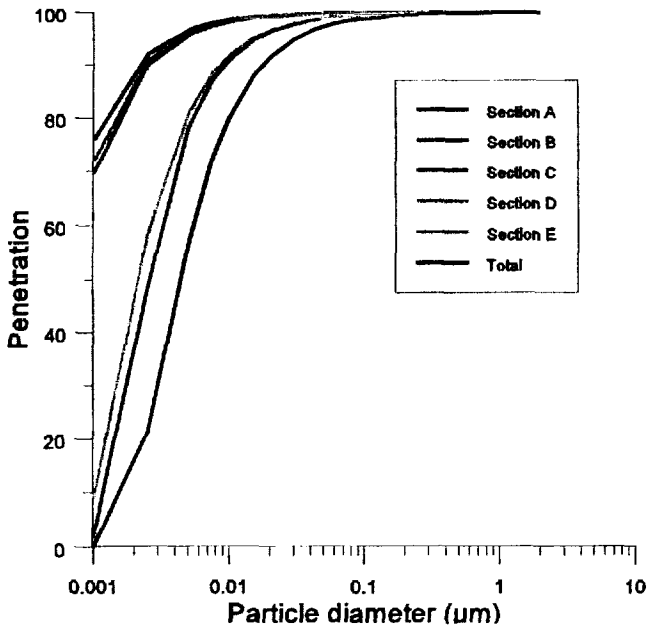

Figure 5.8 : Theoretical penetration in the ejector probe, total and in individual sections A-E (cf. Figure 5.7).Temperature 25°C.

A comparison of measured and calculated penetration (figure 5.9) shows a reasonably good agreement, although the calculations underestimate the particle loss for the smallest particles. This discrepancy is probably caused by turbulence in the probe, which particularly enhances the diffusion of the smallest particles. Turbulence is likely to occur in the area close to the exit from the ejector head (cf. figure 5.3).The results from SMPS measurements are not corrected for the losses from diffusion inside the probe, as the particle losses are deemed insignificant.

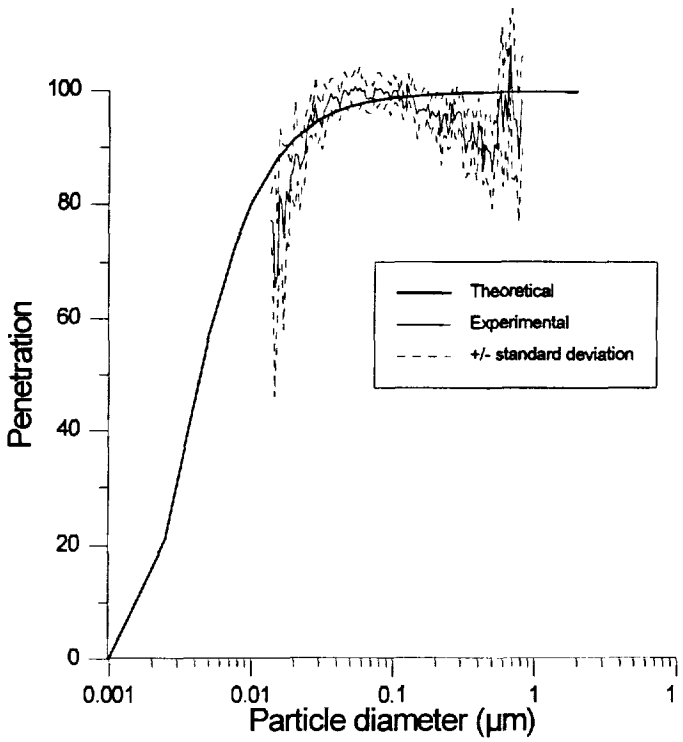

***Figure 5.9** : Total theoretical and experimental penetration in the ejector probe. NaCl-aerosol, temperature 25°C.*

6. Co-firing coal and straw: Aerosol measurement results

The field measurements have resulted in a large amount of data which will be presented in the following. An overview of the completed field experiments and analyses is found in appendix E. Each experiment with a given set of operating conditions (cf. table 5.1) usually lasted one week, the first day of which was used to obtain approximate steady-state conditions in the boiler. Aerosol measurements were scheduled for day three and four.

6.1 Analysis of coal and straw

Coal originating from three different sources were used in this measurement campaign, with type A (bituminous South American) the most widely used. A total of seven experiments were performed with this type, while only one was carried out with type B (bituminous African) and two with type C (bituminous American). The operational parameters for these experiments are listed in Table 5.1. The elemental analysis as well as data on heating value, ash and moisture content are listed in Hansen (1997). A number of general trends for the three coal types are:

- Type A is low in S
- Type B is low in Fe, K, Na, and volatiles, and high in Al, P, and Ca compared to A. S is at the same level as in A.
- Type C is low in total ash, and high in S, Fe, and Cl compared to A.

The straw used was mainly wheat from the harvest of 1995, where Denmark experienced an unusually dry summer. Therefore the straw was not leached by rain, and consequently the potassium and chlorine content of the straw was above average.

6.2 Dilution ratio

The aerosol sample taken from the flue gas channel is diluted with filtered air (section 5.3), and the dilution ratio is calculated from the measurements of the water content of the undiluted flue gas and the diluted aerosol sample . For some experiments, the dilution ratio had to be estimated due to failure of the Cermet hygrometer. The results are listed in table 6.1. The measurements of the water content of the undiluted flue gas were quite successful, as indicated by the modest standard deviation of these results.
The table shows a tendency for the water content of the flue gas to increase with increasing load, and possibly also with increasing straw input.

Table 6.1 *Water content of undiluted flue gas and calculated dilution ratios. Averages and standard deviation of water content with the number of measurements in parentheses.*

	50% load[1]		75% load[1]		100% load[1]	
	Humidity (% vol/vol)	Dilution ratio	Humidity (% vol/vol)	Dilution ratio	Humidity (% vol/vol)	Dilution ratio
0% straw[2], coal A	8.1 ± 0.1 (5)	13.6	8.2 ± 0.1 (4)	16.5[3]	9.1 ± 0.8 (4)	14.3[3]
10% straw[2], coal A	-	-	-	-	10.5 ± 0.4 (4)	14.3[3]
20% straw[2], coal A	8.6 ± 0.8 (2)	12.5	11.4 ± 0.4 (6)	16.5	10.6 ± 0.4 (6)	14.3
0% straw[2], coal B	-	-	7.6 ± 0.2 (3)	16.5[3]	-	

[1]: In percent of maximum load 380 MW_{Th} [2]: Percent of total energy input. [3]: Estimated.

6.3 Fine mode aerosol number and mass size distribution

Between 10-30 number distributions were measured using the scanning mobility particle sizer (SMPS) system for 6-8 hours each day, each measurement lasting eight minutes. The SMPS system was not used in series 3a, 8a, and 9a in 1997. Two or three impactor samples were collected each day, usually with two different impactor foil materials. Each impactor sampling period was approximately 90 minutes to obtain a total mass loading on the foils of 10-40 mg for most of the samples. If possible, the total deposited mass on the foils should be no more than 10 mg in order to prevent overloading of the impactor stages. In this work, however, it was decided to sample a larger mass in order to reduce the uncertainty of the chemical analyses of foil 1-5.

Figure 6.1 shows an example of the format of the number size distribution results, which are presented in full in appendix F. The results are shown as averages of all of the SMPS measurements performed on each day, in this example from series one, with total boiler load 50% of maximum load 380 MW_{Th}, and an energy fraction supplied by straw of 20%. The area under the number size distribution curve is equal to the number concentration of particles in the given size range. The number size distributions are shown as a function of particle mobile diameter, which is independent of density. For a spherical particle, mobile diameter and actual diameter are identical, but for particles other than spherical, the mobile diameter is the diameter of a sphere of the same mobility. Since the duration of an SMPS measurement is short compared to the impactor measurements, the total number concentration calculated from the SMPS results can be used as a semi-continuous monitoring of the submicron aerosol. Figure 6.2 shows an example of the variation in total submicron number concentration from series 1, day 1, and appendix G contains the number concentration plots for all days where SMPS measurements were performed.

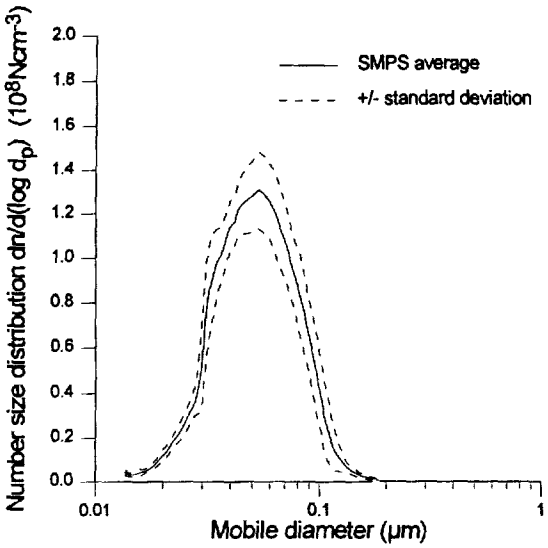

Figure 6.1 *Mean number size distribution of submicron aerosol from series 1, day 1. Type A coal, 50 % load and 20 % straw input. Average of 25 SMPS measurements and standard deviation are shown.*

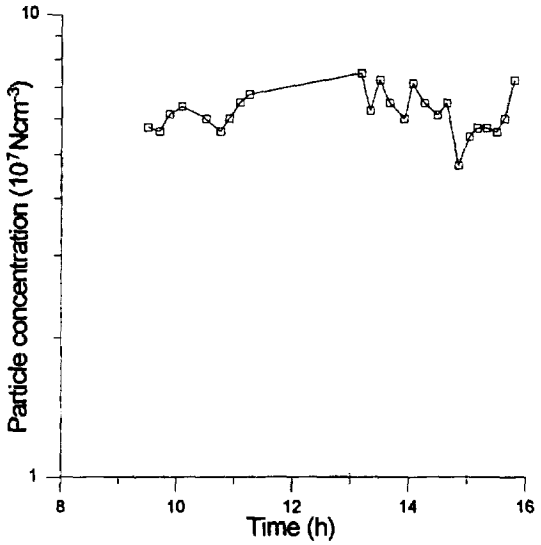

Figure 6.2 *Variation of total submicron number concentration as measured by the SMPS system in series 1, day 1. Coal Type A, boiler load 50%, straw energy input 20%.*

The number distributions, cf. figure 6.1, are unimodal in the range 0.014-0.8 µm which is covered by the SMPS system. The mass distributions, an example of which is shown in figure 6.3 and 6.4, also show a submicron peak below 0.1 µm, although it is somewhat overshadowed by the left flank of the coarse mode peak. The smallest particles belonging to the coarse mode is most likely superimposed on the right flank of the fine mode peak. Again it must be emphasized that the coarse mode distribution in figure 6.3 is not representative of the fly ash particle distribution, as the design and placement of the sampling probe prevents most of the coarse mode particles from entering the sampling line, cf. section 5.7.

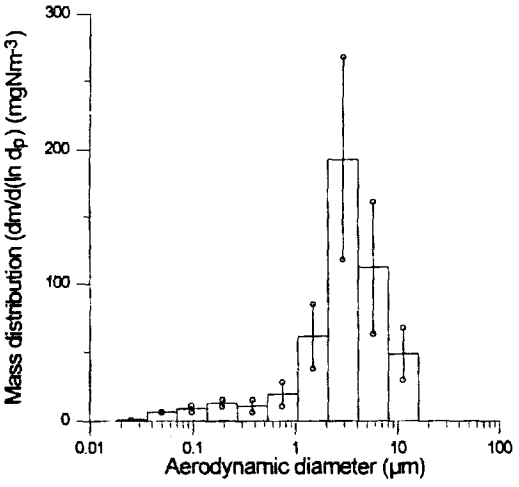

Figure 6.3 *Mean mass distribution as measured by the cascade impactor from series 1, day 1. Average of 2 measurements and standard deviation are shown. Coal Type A, boiler load 50%, straw energy input 20%.*

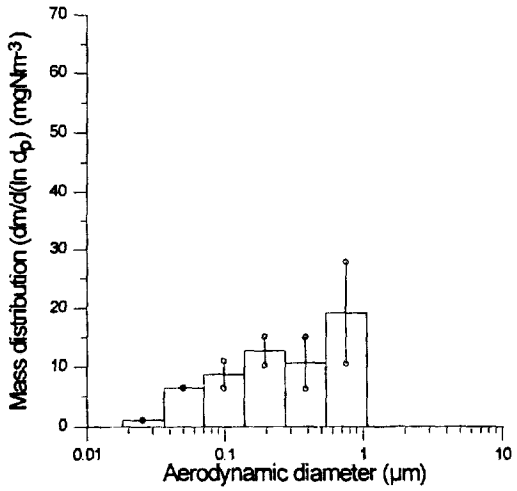

Figure 6.4 *Mean mass distribution as measured by the cascade impactor from series 1, day 1. Stage 1-6. Average of 2 measurements and standard deviation are shown. Coal Type A, boiler load 50%, straw energy input 20%.*

Similarly to the number size distributions, the integral of the mass size distribution equals the mass concentration of particles in a given range. The impactor classifies the particles according to their aerodynamic properties, and mass size distributions are therefore shown as a function of aerodynamic diameter d_{ae}. Actual and aerodynamic diameter are identical only if the particle density is 1 g/cm^3, as d_{ae} depends on density as demonstrated in table 5.2. It is possible to calculate the mass concentration of the fine mode aerosol from the number size distribution, if the density of the particles is known. However, this assumes that the particles are of some well-defined shape, e.g. spherical, and this is far from the case in this study, cf. section 6.4. Therefore, the transformation from number to mass concentration has not been carried out in this work, and the size distributions are presented in their original form. In table 6.2 a summary of average total number concentration and number mean mobile diameter from all SMPS measurements is shown, and the corresponding impactor data are shown in table 6.3.

Table 6.2: Content of submicron particles in flue gas calculated from the SMPS data. Average number concentration, mean mobile diameter and standard deviation are shown.

Series	Coal type	Boiler condition %Load[4]/%Straw nominal (actual)	Number concentration 10^7 Ncm^{-3}	Number of SMPS measurements	Mean mobile diameter nm
1	A	50/20 (57/18)	6.4 ± 0.9	50	50 ± 3.0
2	A	75/20 (71/17)	7.1 ± 1.4	38	87 ± 22
3	A	100/20 (98/16)	9.3 ± 0.4	52	64 ± 2.1
4	A	100/10 (98/10)	6.6 ± 2.1	32	71 ± 6.2
5[2]	A	100/0 (-/-)	8.2 ± 0.4	32	64 ± 1.7
6	A	75/0 (78/0)	5.4 ± 2.4[3]	32	44 ± 9.3
7[1]	A	50/0 (49/0)	3.9 ± 0.1	35	46 ± 3.8
8	B	70/0 (69/0)	7.1 ± 1.8[3]	28	79 ± 3.2

[1]: Data only for day 1. [2]: Data only for day 2. [3]: Peaks not included. [4]:Percent of maximum power 380 MW_{Th}

Discussion of number and mass distribution results

If the plots of total submicron number concentration variation in appendix G are inspected, large fluctuations are evident for some days, e.g. series 4, day 2 and series 6, day 2. If experimental error is ruled out, it is likely that these are caused by changes in the operating conditions, which should therefore be reflected in other measured process variables such as concentrations of CO, CO_2, O_2, NO_x, and SO_2 measured both in the smoke stack and in the boiler, as well as the temperature profiles obtained from positions inside the boiler. However, no convincing correlation has been found to any of these, and the variations must therefore be caused by incidental changes e.g. in fuel composition or burner operation which do not influence the mentioned process variables.

Table 6.3: *Content of submicron particles in flue gas calculated from the impactor data. The average mass concentration and standard deviation are shown. Mean diameter of primary particles are measured from TEM (Transmission electron microscopy) photos. The number of primary particles per cluster is calculated using the impactor mass concentration based on stages 1-5. A particle density of 3.5 g/cm³ is assumed*

Series	Coal type	Boiler conditions %Load [3]/%Straw nominal (actual)	Total fly ash concentration[2] mg/Nm³	no. of impactor measure-ments	Fine mode mass concentration				Primary particles	
					0.01-1.1µm (stage 1-6)		0.01-2.1µm (stage 1-7)		Mean diameter nm	Mean number per cluster
					mg/Nm³	Fraction of total fly ash	mg/Nm³	Fraction of total fly ash		
1	A	50/20 (57/18)	14700	5	35 ± 8	0.24 %	79 ± 21	0.54 %	21	18
2	A	75/20 (71/17)	13500	5	106 ± 19	0.79 %	168 ± 19	1.2 %	25	44
3	A	100/20 (98/16)	10100	4	51 ± 6	0.50 %	92 ± 6	0.91 %	23	18
4	A	100/10 (98/10)	10100	5	51 ± 10	0.50 %	91 ± 16	0.90 %	20	33
5[1]	A	100/0 (-/-)	13100	3	47 ± 15	0.36 %	97 ± 37	0.74 %	17	39
6	A	75/0 (78/0)	14200	4	28 ± 13	0.20 %	54 ± 25	0.38 %	12	74
7	A	50/0 (49/0)	14300	5	33 ± 18	0.23 %	67 ± 28	0.47 %	21	13
8	B	70/0 (69/0)	14100	3	71 ± 8	0.50 %	196 ± 36	1.4 %	ND	ND
3a	A	100/20 (93/17)	8280	3	32 ± 6	0.39 %	62 ± 9	0.75 %	ND	ND
8a	C	100/0 (92/0)	7290	3	45 ± 4	0.62 %	76 ± 2	1.04 %	ND	ND
9a	C	100/20 (92/18)	7300	2	70 ± 17	1.0 %	101 ± 24	1.38 %	ND	ND

[1]: Data only for day 2. [2]: The total fly ash concentration is calculated from tables 3.4.2.1 and 3.5.1 of P.F.B. Hansen (1997).[3]: Percent of maximum power 380 MW_{Th}. ND: Not determined.

The variation in the average total number concentration between the eight series (cf. table 6.2) is modest, from $3.9 \cdot 10^7$ Ncm^{-3} to $9.3 \cdot 10^7$ Ncm^{-3}. Figures 6.5 and 6.6 show the data from table 6.2 graphically to illustrate the dependence of total number concentration on total boiler load and fraction of energy input originating from straw for series 1-7. There is some indication that number concentration increases with increasing boiler load and straw loading, although not very strongly. Both tendencies can be explained by the theory for submicron particle formation discussed in chapter 1. The fine mode aerosol is formed by agglomeration of primary particles, and the size of the agglomerates are influenced, among other factors, by residence time and primary particle size. Increasing the boiler load leads to a decrease in residence time, which again leads to a decrease in agglomerate size and consequently an increase in number concentration. The mean mobile diameters obtained from the SMPS measurements (cf. Table 6.2) do not confirm this theory, which may be due to changes in boiler temperature profile with changing boiler load. Increasing the percentage of straw is expected to lead to an increase in primary particle size, as the total loading of condensing material is increased. This in turn leads to a decrease in the rate of agglomeration (e.g. Friedlander, 1977, chpt. 7). This effect of straw

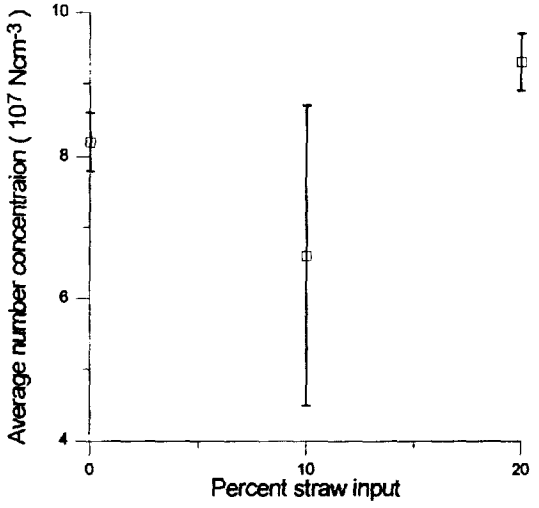

Figure 6.5: *Variation in average submicron aerosol number concentration as a function of straw input on an energy basis. Coal Type A, load 100 %, series 3, 4, and 5.*

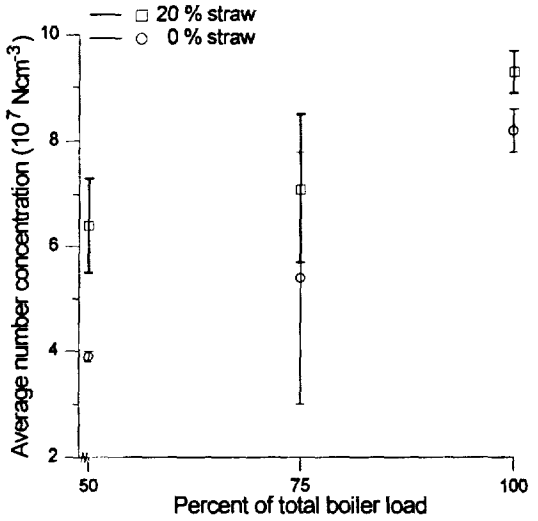

Figure 6.6: *Variation in average submicron aerosol number concentration as a function of total boiler load. Coal Type A, series 1-3 and 5-7.*

loading is to some extent confirmed by the calculations of primary particle size based on the impactor measurements and TEM pictures, cf. table 6.3. The variation of mass concentration in table 6.3 indicates that increasing either total load or straw input does not have a very strong influence. There is a tendency for an increase in mass concentration when the total load or straw input is increased, but on the evidence of the data this may be incidental. Table 6.3 shows mass concentration of submicron aerosol based on both impactor stages 1-6 and 1-7. This corresponds to particles with aerodynamic diameters less than approximately one and two μm, respectively.

The second column, which includes stage 7, corresponds to a real particle diameter of 1 μm if the particle density is assumed to be 4 g/cm^3, see table 5.2. This will be discussed further in section 6.4 on particle morphology. The effect of straw on the mass mean diameter is evident in a general upward shift of the submicron peak in the mass distribution figures in appendix H. This change is significant as it results in a larger mass loading of particles in a size range where removal is very difficult, as mentioned in chapter 1. No large effect of changing the coal type is evident on the mass mean diameter. A small change is evident for series 8a, which is 100% load, 0% straw with coal type C. The submicron peak is located at approximately 0.2 μm (see figure H.32 in appendix H), somewhat higher than all other series with pure coal firing. This again results in an increased mass loading of particles in an unfavorable size range. The increase in the mean mass diameter may be linked to the increased content of iron in coal type C, as some investigators point to iron as the principal nucleating agent in coal combustion, cf. chapter 1. The cause of this different nucleating kinetics is at present unclear.

As mentioned in the previous chapter, in series 6, 7, and 8 the sampling probe is fitted with a tube containing $CaCO_3$-impregnated cylinders, through which the flue gas is withdrawn. Any SO_3 or H_2SO_4 present in the flue gas will react and thus be selectively removed prom the sample. Any presence of H_2SO_4-drops homogeneously nucleated in the cooled probe should thus be indicated by a drop in measured submicron number concentration measured by the SMPS system. Although some changes in number concentration is seen when the $CaCO_3$-containing tube is used, these are indistinguishable from incidental variation in the number concentration.

A very important conclusion from the viewpoint of practical applications is that co-firing coal and straw leads to no significant increase in submicron number or mass concentration, as was the case in the previously mentioned investigation of pure straw-fired stoker-type boilers (Christensen, 1995). The conclusion is of course limited to this particular boiler and straw burner design, and to the types of coal tested.

6.4 Particle morphology

The particle morphology is investigated both with SEM (scanning electron microscopy) on the particles collected on the impactor foils, and by TEM (transmission electron microscopy) on the aerosol sampled on special TEM grids, cf. section 5.5. Using SEM, particles on impactor foils 6-10 can be investigated. Usually, the particles are deposited in a circle of cone-like structures on the foils, and only the top layer is visible in the SEM micrograph. The individual particles deposited on foils 1-5 are indistinguishable by SEM, and the morphology of this fraction of the aerosol is investigated using TEM. The particles are collected by placing the grid in the aerosol stream, and since particle deposition is dependent on size, the distribution on the grid is not

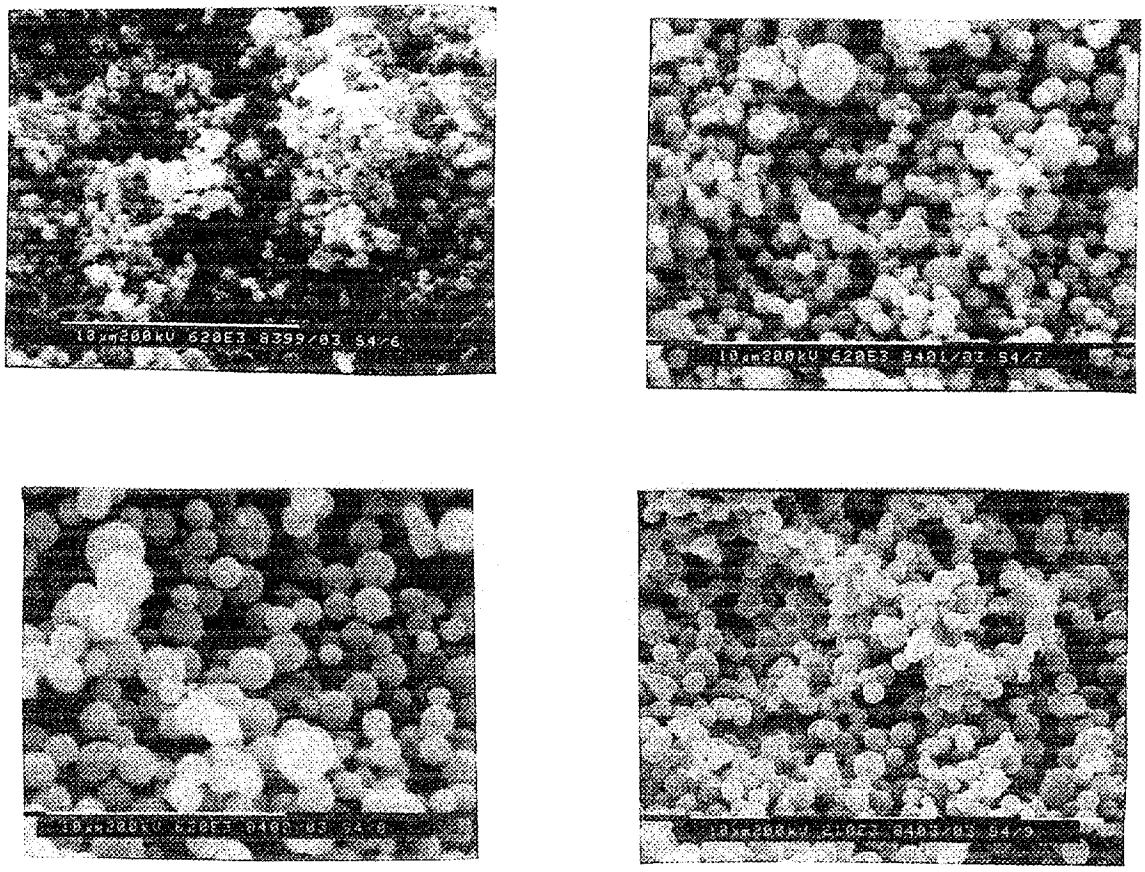

Figure 6.7: *Scanning electron micrograph of particle deposits on impactor stages 6-9. Coal type C, foil set S4. The length of the white bar is 10 μm in all four micrographs.*

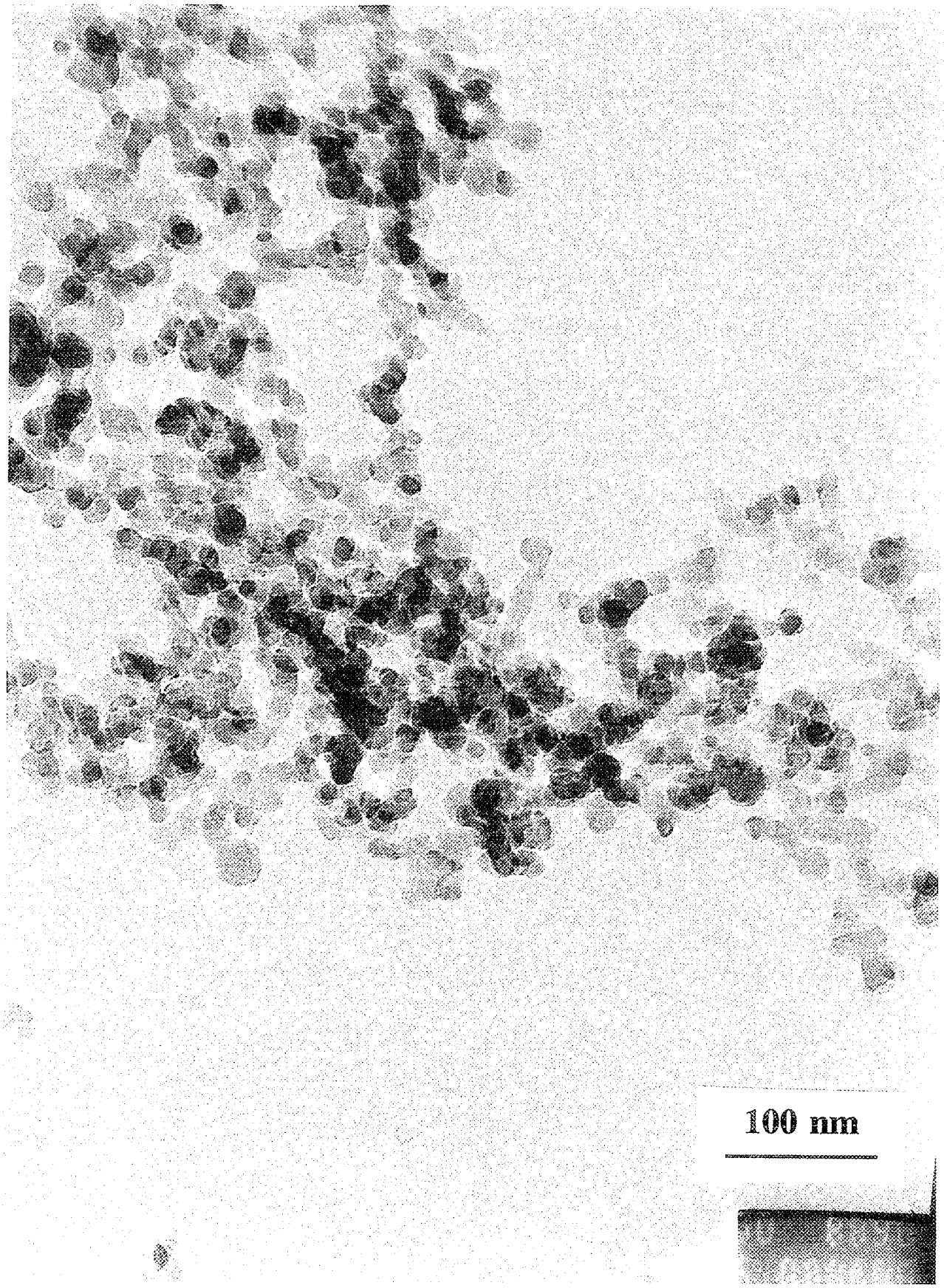

Figure 6.8: *Transmission electron micrograph of conglomerate particle. Coal type 1, series 5.*

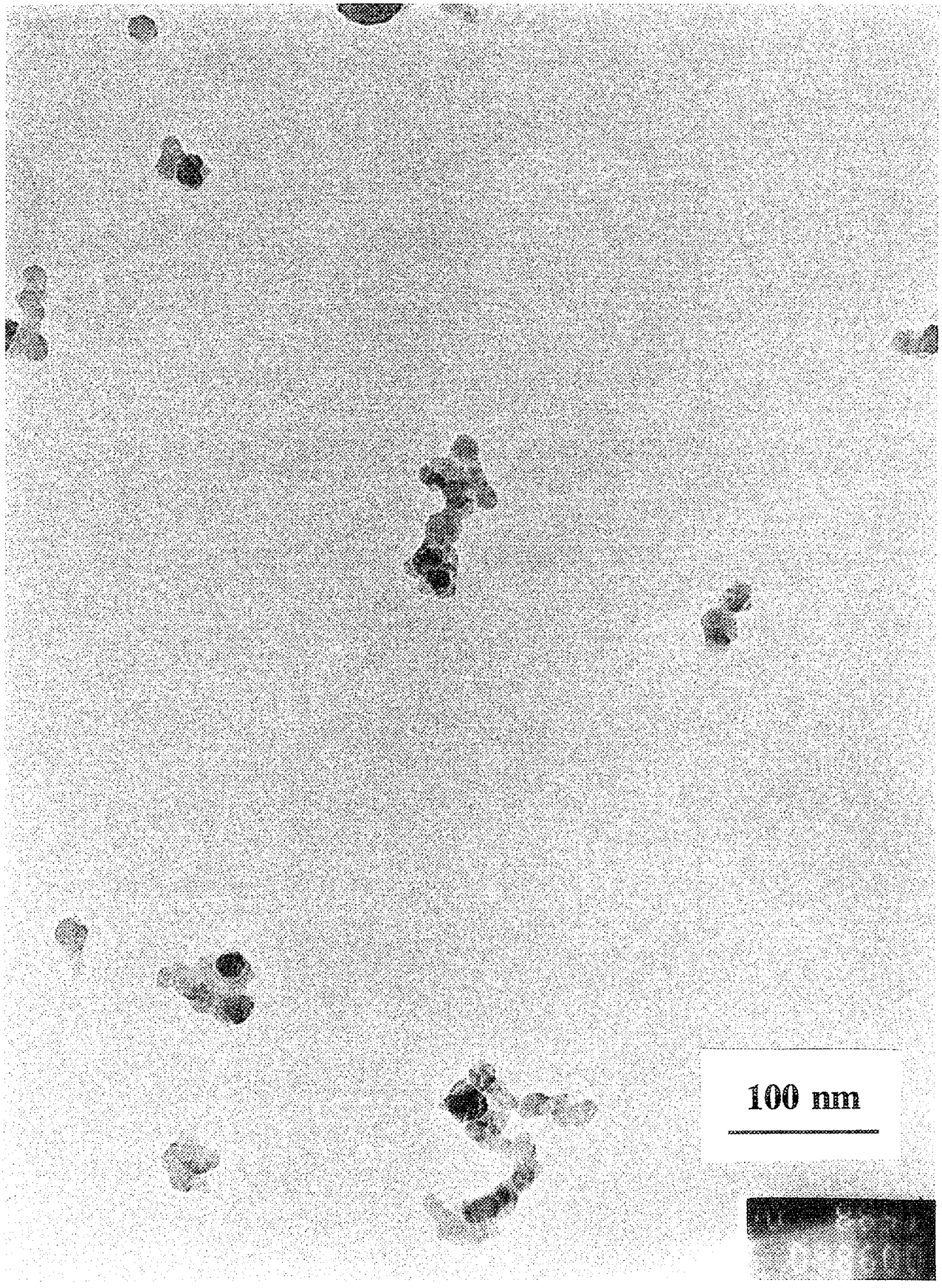

Figure 6.9: *Transmission electron micrograph of same sample grid as figure 6.8 showing smaller conglomerate particles. Coal type 1, series 5.*

identical to the bulk phase aerosol. Particles with diameters between 0.1 and 1 μm are expected to be deposited with low efficiency, cf. the discussion on particle removal in chapter 1.

The SEM micrographs, an example of which is shown in figure 6.7, consistently show that the particles on stages seven to nine are very nearly spherical, and have diameters much smaller than the aerodynamic cut-diameters of the stages where they are collected. This implies that the density is greater than 1 g/cm^3, and from table 5.2 the density can be estimated to be above 4 g/cm^3 for stage nine and close to 4 g/cm^3 for stages seven and eight. The shape of the particles indicate that they belong to the coarse mode, i.e. formed by melting of mineral inclusions in the coal. Visible on some particle surfaces are agglomerates of smaller particles scavenged by the larger particles. Particles on stage six are predominately agglomerates, with a few spherical coarse mode particles. On the basis of the SEM micrographs, stages one to five contain mainly fine mode particles. If stage six is included, some influence from the smallest coarse mode particles must be expected. If one chooses to discuss stages one to seven, significant "contamination" by coarse mode particles must be expected, even though these particles all have diameters less than one μm.

The morphology of the smallest particles is investigated by TEM, which consistently reveals these as agglomerates of fairly uniform primary particles, as demonstrated by figures 6.8 and 6.9. The primary particles are either spherical or polyhedral, and some crystallinity is confirmed by discrete spots in an electron diffraction pattern. Some sintering of primary particles is evident. The number of primary particles in the agglomerated particles varies greatly from just a few to extensive three-dimensional networks. Again, this agrees well with the theory that the fine-mode aerosol fraction are formed by homogeneously nucleated particles, which agglomerate and partly sinter as they travel through the flue gas channel.

6.5 Chemical composition

Two different methods of analysis were employed in this study to determine the distribution of elements in both fine and coarse mode particles, all using samples collected on impactor foils:

1. Energy-dispersive X-ray analysis (EDX)
2. Chemical analyses

EDX analysis

All EDX analyses are carried out at the Department of Process Technology, Technical University of Denmark, with the expert assistance of Inger Søndergaard. Impactor samples are collected on

copper foils in stead of aluminum to prevent interference with the Al-signal from the particles. The cone-shaped deposits are left on the foil and dried at 250 °C for two hours before coating with carbon. The deposits are probed with an electron beam, which leads to the emission of x-rays with energies characteristic of the elements in the sample (e.g. Willeke and Baron, 1993). Elements with atomic weights greater than that of sodium can be detected with a detection limit of approximately 0.1%. Since the fluorescence zone is limited to a layer of depth 1-2 μm, the results for submicron particles represent the bulk composition, while for larger particles, the results only represent the surface composition. Usually an electron beam of 100 x 80 μm was employed, except on stage 10, where very little material is found. The results for stage 10 are excluded from several of the impactor data in the following, as they represent the composition of single particles. EDX analysis results are reported in weight percent of the elements detected, and are represented graphically as a function of aerodynamic diameters corresponding to the appropriate mean size of particles deposited on the given stage. An example of the EDX results is shown in figures 6.10 and 6.11 for a load of 100% and straw energy input of 0 and 20% respectively. The complete composition versus aerodynamic diameter plots for all series are found in appendix I.

From the EDX results a number of general trends are evident. The main components of the particles are Si, Al, Fe, Ca, K, S, and P. One prominent element which is completely absent is Cl. Ba is detected in some samples, but the results are inconclusive as the Ba signal is distorted by interference by Ti and V. The refractory elements Fe, Al, and Si are distributed evenly, cf. figures 6.11 And 6.10, although the concentration decreases somewhat in the smaller particles when straw is used. This is caused by dilution with the increased amounts of volatile elements as discussed below. The elements Ca, S, and P are enriched in the smallest particles, both in the presence and absence of straw. As an example, the distribution of S is depicted in figure 6.13 for all series.

Potassium is usually counted among the volatile species, and K should therefore also be significantly enriched in the submicron particles compared to the larger particles on stages 7-9. As exemplified by figure 6.12, this is definitely not the case in this study. When coal is used alone, the level of K is much lower than during co-firing, since straw is the main source of this element. The concentration of K actually decreases with decreasing particle size implying that K is a non-volatile species when coal is used alone. When straw is co-fired, the potassium level is quite even, although some enrichment of the smaller particles is seen. A significant amount of potassium is however found in the coarse mode particles, i.e. there is no indication that the potassium preferentially condenses on the fine mode particles even when large amounts of potassium is available.

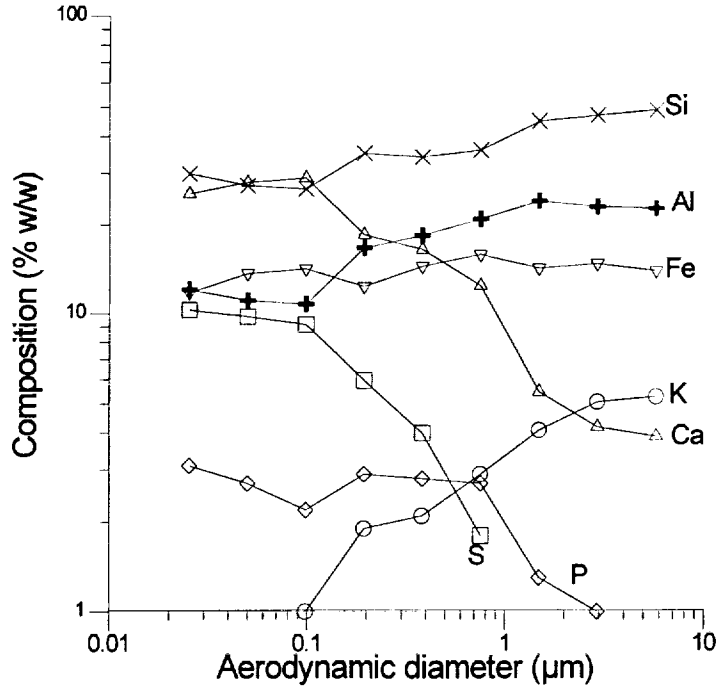

Figure 6.10 *EDX-data for series 5, day 2. Type A-coal 100% load, 0% straw, impactor sample 38. Distribution of main elements in weight % of elements detected.*

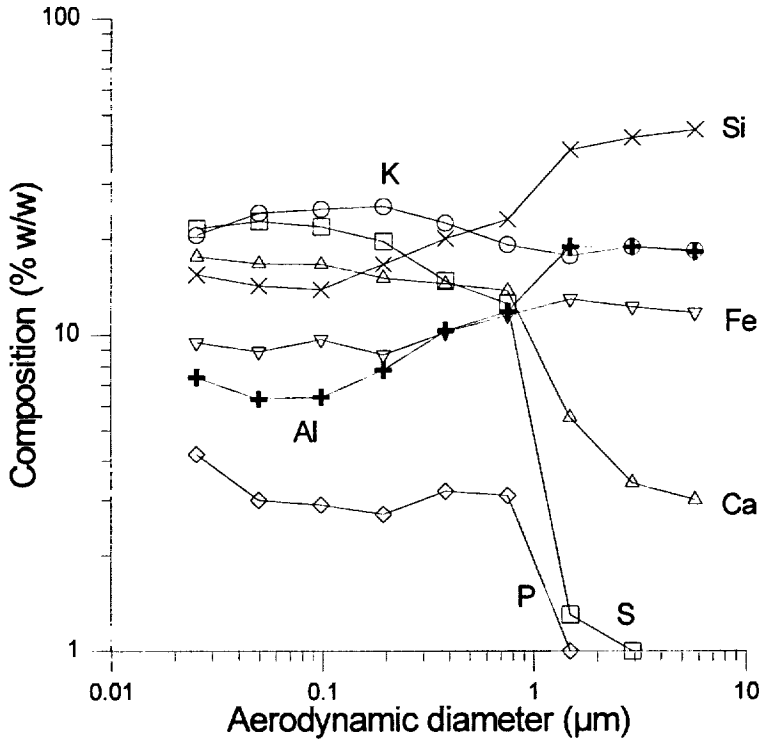

Figure 6.11: *EDX-data for series 3, day 2. Type A-coal 100% load, 20% straw, impactor sample 27. Distribution of main elements in weight % of elements detected.*

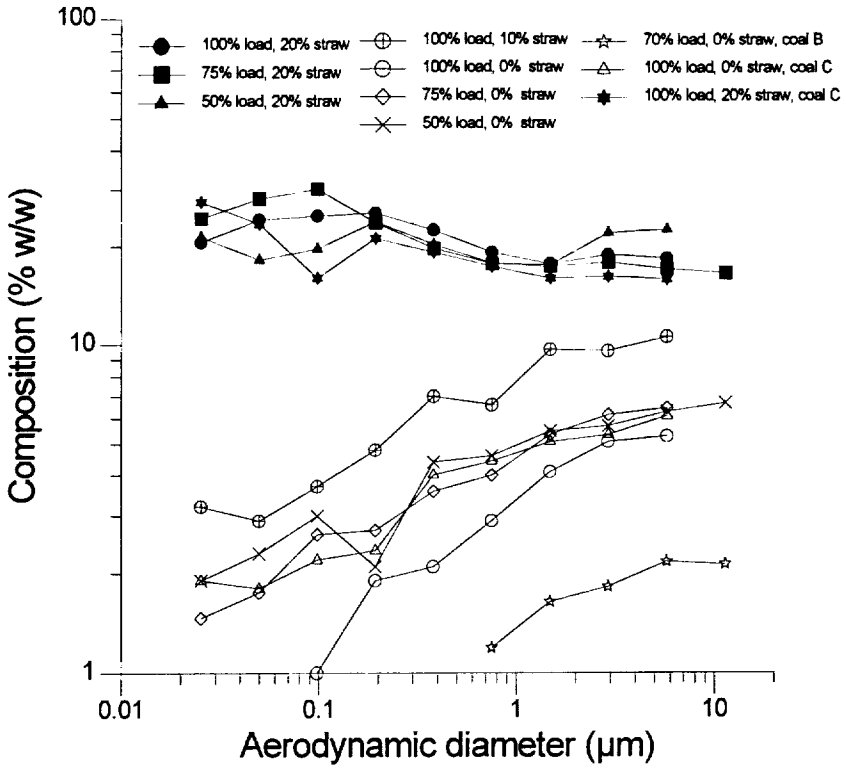

Figure 6.12 *Distribution of potassium for all series as measured by EDX. Weight% of main elements.*

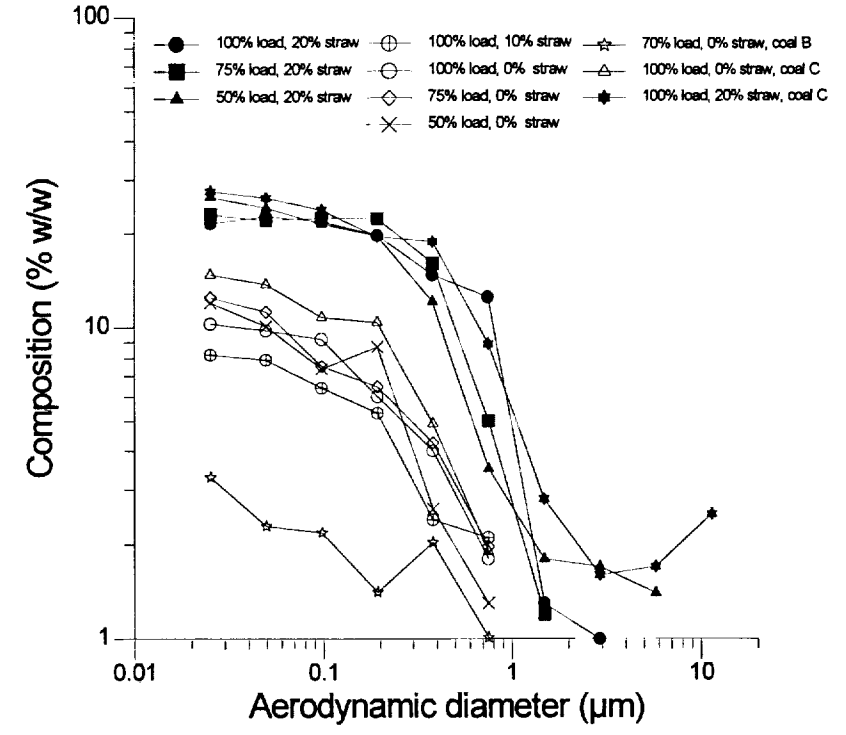

Figure 6.13 *Distribution of sulphur for all series as measured by EDX. Weight% of main elements*

Chemical analyses

The chemical analyses are performed by the laboratory at Studstrup power plant. K^+, Na^+, Ca^{2+}, Cl^-, PO_4^{3-}, and SO_4^{2-} are analyzed for using flame photometry and atom absorption spectroscopy. The particles are collected in the impactor on untreated aluminum foils, weighed, and subsequently foils one through five are cut in half and one half foil immersed in 50 ml ultrapure water for one hour before analysis. The detection limit is roughly 0.5% (W/W). Generally, no Cl^- or PO_4^{3-} is found in any of these analyses, and they are excluded from the following. The results of the chemical analyses are summarized in table 6.4.

***Table 6.4**: Summary of chemical analyses. Data are shown as weight percent of ions, and are averages if more than one impactor sample is available. Also listed are EDX data obtained under the same boiler conditions, where elements are assumed to be present as oxides. Chemical analysis results are averages of stage 1-5. Series 1-7 are made with Type A coal, and series 8 with Type B. Final column states the percentage of total mass deposited on stage 1-5 accounted for by K^+, Na^+, Ca^{2+}, and SO_4^{2-}.*

Series	%load/	K^+		Na^+		Ca^{2+}		SO_4^{2-}		Chemical,
	%straw	Chem	EDX	Chem	EDX	Chem	EDX	Chem	EDX	all ions
1	50/20	6.23	11.6	1.31	0.36	3.2	8.7	22.1	31.2	32.8
2	75/20	5.7	8.08	0.89	0.37	2.44	7.97	13.1	25	22.1
3	100/20	2.08	13.2	0.45	0.42	5.13	8.61	18.6	32.4	26.3
4	100/10	0.5	2.53	0.14	0.1	2.28	9.5	5.79	8.49	8.72
5	100/0	0	0.82	0.18	0.1	3.02	11.8	8.56	11	11.8
6	75/0	0	1.29	0.02	0	1.45	9.42	6.6	12.9	8.07
7	50/0	0	3.22	0	0	2.82	1.71	6.45	1.26	9.27
8	70/0	0	0.18	0.06	0	2.9	16.1	1.8	3.09	4.77

It is apparent from the table that the submicron particles are enriched in both potassium and sulphur when straw is used compared to pure coal combustion, and that no Cl is present. This supports the conclusions from the EDX analyses well. With the occasional exception of Na^+, the EDX results generally show a larger content of the ions than the chemical analyses, indicating that a large fraction of these are insoluble in water. The fraction of K-, Na-, Ca-, and S-compounds which are water soluble increases when straw is used.

6.6 Discussion of elemental distribution

As discussed in chapter 1, enrichment of submicron particles is characteristic of elements which have been completely volatilized and condense on the surface of previously formed particles present in the gas phase. Such enrichment is seen for Ca, P, and S. This behavior is somewhat unexpected for Ca, but the data are consistent in this matter. From theory it is expected that the concentration of completely volatilized species in the particles depend on the particle size. The variation in concentration is proportional to d_p^{-2} in the continuum range ($d_p >> 0.1$ μm, cf. chapter 3) and to d_p^{-1} in the molecular range ($d_p << 0.1$ μm) (Flagan and Seinfeld, 1988 chpt.6). Some proportionality to d_p^{-n} is indicated in a narrow band around one μm by the EDX data, but not for the smallest particles, i.e. those on stages 1-4, where the concentration of Ca, P, and S is relatively constant. This can be explained by mixing of the elements by agglomeration of the smallest particles. The smallest particles rich in P, S, and Ca quickly agglomerate in the boiler as they collide with larger particles where these elements are less abundant, resulting in a population of small particles detected on impactor stages 1-4 which are fairly uniform in composition.

Recalculation of the data in table 6.4 shows a rough agreement between the amounts of water soluble positive ions (K^+, Na^+, and Ca^{2+}) and the amount of water soluble negative ions, in this case SO_4^{2-}. This most likely indicates that these elements are present in the submicron particles as sulphates formed by sulphation reactions. For potassium this gas phase sulphation can be summarized by

$$2KCl + H_2O + SO_2 + \tfrac{1}{2}O_2 \rightleftharpoons K_2SO_4 + HCl \qquad \textbf{(6.1)}$$

Equilibrium calculations show that potassium is released from the straw at high temperature as KOH and KCl, sulphur and additional chlorine as SO_2 and HCl (Christensen, 1995). Calculations based on results from pure straw combustion in a stoker-type boiler indicate that reaction (6.1) is at equilibrium above 800°C, and that the equilibrium shifts to the right during cooling. The reaction rate becomes negligible at temperatures below 800°C. The effect of the sulphation reaction is to expel chlorine from species which will eventually condense. The EDX and chemical analyses support the validity of this theory even during co-firing of coal and straw. A simultaneous increase of potassium and sulphur in the submicron particles is observed when straw is used as a fuel, but the sulphur does not originate from the straw which is relatively low in sulphur. It is therefore likely that the increased potassium level leads to an increase in the conversion of S(IV) to S(VI) through reaction (6.1), and consequently to an increased binding of sulphur as K_2SO_4. This later condenses heterogeneously on the submicron particles as the gas is cooled. The fact that chlorine is completely absent from the smallest particles indicates that

reaction (6.1) most likely proceeds at temperatures below 800°C.

The mass of the coarse mode fraction quite dominates the fly ash, and the main part of the potassium therefore ends up in this fraction. It is, however, not bound to sulphur or chloride in the large particles, as these elements are absent from the large particles. The data suggest that potassium volatilized from the straw reacts with the coarse mode particles to form compounds of the form Al_2O_3,K_2O,nSiO_2. This reaction probably takes place at temperatures above the range of the sulphate condensation, i.e. 800-1100 °C. The theory of this potassium-binding reaction is supported by the observed absence of K in the small particles during pure coal combustion. It also explains why the submicron particles are only moderately enriched by potassium during co-firing of coal and straw, as most of the potassium is strongly bound in Al_2O_3,K_2O,nSiO_2 compounds when heterogeneous condensation of K_2SO_4 commences.

The fine mode particles also contain aluminum and silicon, and a reaction with potassium to form the same Al_2O_3,K_2O,nSiO_2 compound is therefore possible. The data indicate that the potassium preferentially reacts with the large particles, even though the small particles have a much greater surface area available for reaction. The explanation may be that the potassium-binding reaction is not mass transfer controlled, but in stead is limited by the kinetics of the reaction in the ash phase. Other possible explanations are differences in chemical composition or phase. The agglomerated structure of the fine mode particles indicates that they have been solid for most of the time after formation, whereas the spherical coarse mode particles clearly have been molten for some time in the boiler.

The effect of the coal type on the particle composition is moderate in the absence of straw, if the EDX-measurements for e.g series 6 (75% load, 0% straw, coal type A) and 8 (70% load, 0% straw, coal type B) as well as series 5 (100% load, 0 % straw, coal type A) and 8a (100% load, 0 % straw, coal type C) are compared. A lower content of sulphur, iron, and potassium and an increase in the concentration of calcium for series 8 is seen (see e.g figure 6.12 and 6.13) when compared to series 6, and an increase in the iron content is seen for series 8a compared to series 5. These changes most likely stem from the differences in coal composition listed in the beginning of this chapter. In the case where straw is co-fired, the results from series 3 (100% load, 20% straw, coal type A) and 9a (100% load, 20% straw, coal type C) differ somewhat. The small particles in series 9a have a larger content of S, and all sizes have a higher iron content than series in 3a. This is probably another reflection of the difference in composition of the two coal types. Although the chlorine content of type C coal is an order of magnitude greater than the other coals, no Cl is evident in any particle sizes analyzed by EDX.

7. Conclusion

A laboratory system for investigation of condensation processes in vapors containing condensing components has been designed and tested. The central unit of the setup is a 173 cm long tubular furnace, where the first part ensures that the carrier gas is heated and saturated with the component to be investigated. The second parts is the condenser, where the cooling rate can be varied within wide limits. The system is versatile and easy to use, and the possibilities for investigating condensation processes are many.

The homogeneous nucleation of KCl from a saturated gas has been studied in the LFAC, using the scanning mobility particle sizer SMPS system to characterize the effluent aerosol. A high number concentration of submicron aerosol is readily formed. Depending on initial KCl concentration and cooling rate between $3 \cdot 10^6$ and $3 \cdot 10^7$ particles/cm^3 at 20°C with geometric mean diameters from 0.1 to 0.35 μm. The number concentration depends on the temperature at which homogeneous nucleation takes place, which results in the largest number concentration being formed at the lowest initial concentration of KCl. The size of the particles increases with increasing KCl concentration and decreasing cooling rate. The homogeneous nucleation of KCl can be completely suppressed by the addition of a laboratory generated aerosol in a concentration of approximately 10^5 particles/cm^3. A mathematical model is presented which describes the evolution of the KCl aerosol in the LFAC. The model is in good agreement with the experimental data, and yields additional insight into the condensation processes.

An extensive field investigation of aerosols from co-combustion of coal and straw has been carried out at the Studstrup power plant in Århus, Denmark. A novel ejector probe, which dilutes the flue gas sample at high temperature, has been designed. Three different coal types have been used, and total boiler load and straw input was varied systematically. The aerosol has been characterized using a SMPS system and a Berner-type low-pressure impactor. The impactor samples have been analyzed by aqueous chemical analysis and energy-dispersive x-ray analysis (EDX). The flue gas is found to contain between $4 \cdot 10^7$ and $9 \cdot 10^7$ particles/cm^3 at 20°C, and the geometric mean diameter of the particles is from 0.04 to 0.09 μm. The main constituents of the aerosol determined by EDX are the elements Si, Al, Fe, K, Ca, S, and P. The small particles, i.e. with diameters less than 1 μm, are enriched in Ca, S, and P. The concentration of potassium decreases with decreasing particle size, probably as a result of a high-temperature reaction with the Si and Al of the larger particles. No chlorine is found in the particles collected, probably because the KCl present in the gas phase at high temperature is converted to K_2SO_4 by the sulphation reaction. An important conclusion is that the number and mass concentration of submicron aerosol are insignificantly changed by co-firing of straw under the conditions investigated.

References

Anisimov, M.P., Hämeri, K, and Kulmala, M. (1994). Construction and test of laminar flow diffusion chamber: Homogeneous nucleation of DHB and *n*-hexanol. *J. Aerosol Sci.* **25**, 23-32.

Baxter, L.L., Mitchell, R.E., and Fletcher, T.H. (1997). Release of inorganic material during coal devolatilization. *Combust. Flame* **108**, 494-502.

Baxter, L.L. (1992). Char fragmentation and fly ash formation during pulverized-coal combustion. *Combust. Flame* **90**, 174-184.

Bertozzi, G., and Soldani, G. (1967). Surface tension of molten salts. Alkali sulfate and chloride-sulfate binary systems. *J. Phys. Chem.*, **71**(5), 1536-1538.

Bird, R.B., Stewart, W.E., and Lightfoot, E.N. (1960). *Transport Phenomena.* Wiley, New York.

Christensen, K.A. (1995). *The formation of submicron particles from the combustion of straw.* Ph.D.-thesis, Department of Chemical Engineering, Technical University of Denmark, Lyngby.

Clausen, J.C. and Rasmussen, I. (1993). Co-firing of coal and straw in large boilers. *IEE Conf. Publ.* **385** (Renewable Energy-Clean power 2001), 43-48.

Dahneke, B. (1983). Simple kinetic theory of Brownian diffusion in vapors and aerosols. In: *Theory of dispersed multiphase flow* (R.E. Meyer, Ed.) pp. 97-138. Academic Press, New York.

Damle, A.S., Ensor, D.S., and Ranade, M.B. (1982). Coal combustion aerosol formation mechanisms: A review. *Aerosol Sci. and Technol.* **1**, 119-133.

Dockery, D.W., Pope III, C.A., Xu, X., Spengler, J.D., Ware, J.H., Fay, M.E., Ferris, Jr., B.G., and Speizer, F.E. (1993). An association between air pollution and mortality in six U.S. cities. *N. Engl. J. Med.* **329**(24), 1753-1759.

Flagan, R.C. and Friedlander, S.K. (1978). Particle formation in pulverized coal combustion -a review. In *Recent developments in aerosol science*. Editor D.T. Shaw, 25-59, Wiley, New York.

Flagan, R.C. and Taylor, D.D. (1981) Laboratory studies of submicron particles from coal combustion. *Symp. (Int.) Combust.*, **18**, 1227-1237.

Fluent User's Guide. (1996) Release 4.4.

Friedlander, S.K. (1977) *Smoke, Dust, and Haze.* Wiley, New York.

Gelbard, F., Tambour, Y., and Seinfeld, J.H. (1980). Sectional representation for simulating aerosol dynamics. *J. Colloid Interface Sci.*, **76**(2), 541-556.

Gelbard, F. (1990). Modeling multicomponent aerosol particle growth by vapor condensation. *Aerosol Sci. Techn.*, **12**, 399-412.

Handbook of Chemistry and Physics. (1986). 67th Ed. CRC press, Florida.

Hansen, P.F.B. (1997). *MKS1 Demonstration Program - Elemental balances and mass balance closure*. I/S Midtkraft internal report. (In Danish).

Harrison, R.M., and Jones, M. (1995). The chemical composition of airborne particles in the UK atmosphere. *Sci. Total. Environ.* **168**, 195-214.

Helble, J., Neville, M., and Sarofim, A.F. (1986). Aggregate formation from vaporized ash during pulverized coal combustion. *Symp. (Int.) Combust.*, **21**, 411-417.

Joutsensaari, J., Kauppinen, E., Ahonen, P., Lind, T., Ylätalo, S., Jokiniemi, J., Hautanen, J., and Kilpeläinen, M. (1992). Aerosol formation in real scale pulverized coal combustion. *J. Aerosol Sci.*, **23**(Suppl. 1), 241-244.

Kacker, A., and Heist, R.H. (1985). Homogeneous nucleation rates. I. Ethanol, *n*-propanol, and *i*-propanol. *J. Chem. Phys.* **82(6)**, 2734-2744.

Katz, J.L. (1970). *J. Chem. Phys.* **52**, 4773.

Kauppinen, E.I. and Pakkanen, T.A. (1990). Coal combustion aerosols: A field study. *Environ. Sci. Technol.*, **24**(12), 1811-1818.

Kauppinen, E.I., Lind, T,M., Valmari, T., Ylätalo, S., Jokiniemi, J.K., Powell, Q., Gurav, A.S., Kodas, T.T., and Mohr, M. (1996). The structure of submicron ash from combustion of pulverized South African and Colombian coals. *Appl. Adv. Technol. Ash-Relat. Probl. Boilers (Proc. Eng. Found. Conf.).* 471-484. Baxter, L.L., and DeSollar, R. (Eds.). Plenum, New York, N.Y.

Knacke, O., Kubaschewski, O., and Hesselmann, K. (Eds.) (1991). *Thermochemical properties of inorganic substances.*, 2nd edition, Springer-Verlag, Berlin.

Lehtinen, K.E.J., Windeler, R.S., and Friedlander, S.K. (1996). Prediction of nanoparticle size and the onset of dendrite formation using the method of characteristic times. *J. Aerosol Sci.*, **27**(6), 883-896.

Linak, W.P., and Peterson, T.W. (1986). Mechanisms governing the composition and size distribution of ash aerosol in a laboratory pulverized coal combustor. *Symp. (Int.) Combust.*, **21**, 399-410.

Markowski, G.R., Ensor, D.S., Hooper, R.G., and Carr, R.C. (1980). A submicron aerosol mode from a pulverized coal utility boiler. *Environ. Sci. Technol.*, **14**, 1400-1402.

Markowski, G.R. and Filby, R. (1985). Trace element concentration as a function of particle size in fly ash from a pulverized coal utility boiler. *Environ. Sci. Technol.*, **19**(9), 796-804.

McCain, J.D., Gooch, J.P., and Smith, W.B. (1975). Results of field measurements of industrial particulate sources and electrostatic precipitator performance. *J. Air Poll. Control Assoc.*, **25**, 117-121.

McElroy, M.W., Carr, R.C., Ensor, S., and Markowski, G.R. (1982). Size distribution of fine particles from coal combustion. *Science*, **215**, 13-19.

Miles, T.R., Miles, T.R. Jr., Baxter, L.L., Bryers, R.W., Jenkins, B.M., and Oden, L.L. (1996). Boiler deposits from firing biomass fuels. *Biomass Bioenergy* **10**(2-3), 125-138.

Monn, CH., Braendli, O., Schaeppi, G., Schindler, CH., Ackermann-Liebrich, U., Leuenberger, PH., and SAPALDIA team (1995). Particulate matter <10μm (PM_{10}) and total suspended particulates (TSP) in urban, rural and alpine air in Switzerland. *Atmos. Environ.* **29**(19), 2565-2573.

Neville, M. and Sarofim, A.F. (1982). The stratified composition of inorganic submicron particles produced during coal combustion. *Symp. (Int.) Combust.*, **19**, 1441-1449.

Nguyen, H.V., Okuyama, K., Mimura, T., Kousaka, Y., Flagan, R.C., and Seinfeld, J.H. (1987). Homogeneous and heterogeneous nucleation in a laminar flow aerosol generator. *J. Colloid Interface Sci.* **119(2)**, 491-504.

Pedersen, C., and Røkke, M. (1996). *Combustion aerosols from co-firing of coal and straw.* (In Danish). Preparatory M.Sc. thesis, Department of Chemical Engineering, Technical University of Denmark, Lyngby.

Quann, R.J. and Sarofim, A.F. (1982). Vaporization of refractory oxides during pulverized coal combustion. *Symp. (Int.) Combust.*, **19**, 1429-1440.

Quann, R.J., Neville, M., and Sarofim, A.F. (1990). A laboratory study of the effect of coal selection on the amount and composition of combustion generated submicron particles. *Combust. Sci. and Tech.* **74**, 245-265.

Reid, R.C., Prausnitz, J.M., and Pooling, B.E. (1987). *The properties of gases and liquids*, 4th Ed. McGraw-Hill, New York.

Sander, B. (1997). Properties of Danish biofuels and the requirements for power production. *Biomass Bioenergy* **12**(3), 177-183.

Schmitt, J.L., Zalabsky, R.A., and Adams, G.W. (1983). Homogeneous nucleation of toluene. *J. Chem. Phys.* **79(9)**, 4496-4501.

Seinfeld, J.H. (1986). *Atmospheric chemistry and physics of air pollution.* Wiley, New York.

Sharaf, M.A., and Dobbins, R.A. (1982). Comparison of measured nucleation rates with the predictions of several theories of homogeneous nucleation. *J. Chem. Phys.* **77(3)**, 1517-1526.

Simonsen, O. (1993). *Condensation of sulfuric acid vapors - Dynamics of binary aerosol condensation.* Ph.D.-thesis, Department of Chemical Engineering, Technical University of Denmark, Lyngby

Smith, J.M., and Van Ness, H.C. (1987). *Introduction to chemical engineering thermodynamics*, 4th Ed., McGraw-Hill, New York.

Smolík, J. and Žmídal, V. (1993). Condensation of supersaturated vapors. Homogeneous nucleation of bis(2-ethyl-hexyl)sebacate (DEHS). *J. Aerosol Sci.* **24**, 589.

United States Environmental Protection Agency, Office of Air and Radiation, Office of Air Quality Planning and Standards (1997). EPA's revised particulate matter standards. *EPA Fact Sheet*, July 17, 1997.

Villadsen, J. and Michelsen, M.L. (1978). *Solution of differential equations by polynomial approximation.* Prentice-Hall, New Jersey.

Vincent, J.H. (1989). *Aerosol sampling.* John Wiley Sons Ltd., New York.

Vogelsberger, W. (1980). Influence of curvature-dependent surface tension on the free energy of formation of microclusters. *Chem. Phys. Lett.*, **74**, 143-146.

Wagner, P.E., and Strey, R. (1984). Measurements of homogeneous nucleation rates for *n*-nonane vapor using a two-piston expansion chamber. *J. Chem. Phys.* **80**, 5266-5275.

Wawra, H. (1972). Temperature and pressure dependence of free surface energy of solid and liquid potassium chloride between 0 deg. and 1400 deg. K. (In German). *Radex-Rundschau*, **5**, 351-364.

Willeke, K., and Baron, P.A. (Eds.) (1993). *Aerosol measurement.* Van Nostrand Reinhold, New York.

Wolf, M.E., and Hidy, G.M. (1997). Aerosols and climate: Anthropogenic emissions and trends for 50 years. *J. Geophys. Res.* **102**(D10), 11113-11121.

Appendix A: A model for saturation in a packing of porous pellets

A simple isothermal model for the saturation of a gas with KCl is derived, in which it is assumed that the saturation can be viewed as taking place in a packed column with plug flow.

A mass balance over a segment of the column of width Δz for component j yields

$$v \cdot c_j|_z - v \cdot c_j|_{z+\Delta z} + k_g(c_j^* - c_j) \cdot A \cdot a \cdot \Delta z = 0 \qquad \textbf{(A.1)}$$

where v is the gas flow in m^3/s, c_j the concentration of component j in mol/m^3, k_g the mass transfer number in m/s, c_j^* the saturation concentration of component j, A the cross-sectional area of the packing in m^2 and a the packing surface area-to-volume ratio of the packing in m^{-1}.

Division by Δz and taking the limit as $\Delta z \to 0$ yields

$$v\frac{dc_j}{dz} = k_g(c_j^* - c_j)Aa \Leftrightarrow \frac{dp_j}{dz} = \frac{k_g A a}{v}(p_j^* - p_j) \qquad \textbf{(A.2)}$$

where p_j is the partial pressure of component j in Pa and p_j^* the vapor pressure of pure component j, also in Pa.

The mass transfer number k_g is estimated using the relation $\epsilon j_D = 0.357/Re^{0.358}$, where ϵ is the porosity of the packing and j_D is the j-factor. The Reynolds number Re is defined as $dv\rho/\mu$, where d is the diameter of the pellets, v the linear gas velocity based on an empty tube, ρ the density of the gas, and μ the viscosity. It is now possible to calculate k_g from the expression

$$j_D = ShSc^{-\frac{1}{3}}Re^{-1} = \frac{k_g}{v}Sc^{\frac{2}{3}} \qquad \textbf{(A.3)}$$

where Sh is the Sherwood number, and Sc the Schmidt number, given by $Sc = \mu/\rho D_{jm}$. D_{jm} is the coefficient of diffusion for component j in the gas phase. The differential equation (A.3) is solved using a fifth or sixth order Runge-Kutta method in the FORTRAN code DVERK.

The solution of the differential equation (A.3) is implemented in the FORTRAN code SAT.FOR, which requires an input file KCLSAT.IN containing the relevant physical parameters of the problem.

Appendix B: Physical properties

The simulation program MONAERO (chapter 3) requires a number of temperature-dependent, component-specific functions, which are specified in the following sections.

B.1 Equilibrium vapor pressure

The equilibrium vapor pressure of pure KCl is calculated from the data in Knacke et al. (1991). The following expression is used to calculate the vapor pressure p_i^* in bar:

$$Log_{10}(p_i^*) = \frac{10^3 \cdot e}{T} + f \cdot \log_{10}(T) + g \qquad \textbf{(B.1)}$$

where T is the temperature in Kelvin. The expression (B.1) is valid below as well as above the melting point of KCl. the parameters e, f, and g are listed in table B.1 below.

Table B.1 *Parameters for the calculation of equilibrium vapor pressure of KCl given by equation B.1.*

e	f	g	Temperature range (K)
-12.151	-2.99	17.254	<1045
-11.326	-4.21	20.148	≥1045

B.2 Surface tension

The temperature and phase dependent surface tension of KCl is calculated by the Tolman equation (e.g. Vogelsberger, 1980). The surface tension σ_i is given by

$$\sigma_i = \sigma_{\infty i}\left(1 + 4\frac{\delta_i}{d_p}\right)^{-1} \qquad \textbf{(B.2)}$$

where $\sigma_{\infty i}$ is the macroscopic surface tension and δ_i the Tolman length. The equation (B.2) includes the dependence of σ_i on the curvature of the particles.

Experimental data for surface tension of solids is rare in the literature. In this work σ_i is calculated from data of Wawra (1972), who determined the surface tension of solid KCl in the temperature range 0-1400 K by determination of elastic constants. The data of Bertozzi and Soldani (1967) are used for the surface tension of liquid KCl above the melting point of 1044 K. A piecewise, non-continuous expression is used for calculation of $\sigma_{\infty i}$:

$$\sigma_{\infty,KCl} = \begin{cases} 0.2987 - 1.376 \cdot 10^{-4} T & T < 1044K \\ 0.1588 - 7.4 \cdot 10^{-5}(T - 273.15) & T \leq 1044K \end{cases} \qquad \textbf{(B.3)}$$

B.3 Gas viscosity

The gas viscosity of nitrogen is calculated from a linear interpolation based on data from Handbook of Chemistry and Physics (1986). The expression is given by

$$\mu = 94.4077 + 0.30607T \qquad \textbf{(B.4)}$$

Where μ is in micropoise and T in Kelvin.

B.4 Thermal conductivity

The thermal conductivity of gaseous nitrogen k in SI-units as a function of temperature is given by Reid (1987):

$$k = A + BT + CT^2 + DT^3 \qquad \textbf{(B.5)}$$

The constants for nitrogen at 1 bar, 115 to 1470 K are

A	B	C	D
$3.919 \cdot 10^{-4}$	$9.816 \cdot 10^{-5}$	$-5.067 \cdot 10^{-8}$	$1.504 \cdot 10^{-11}$

B.5 Heat capacity

The heat capacity C_p of gaseous nitrogen in SI-units is given by Smith and van Ness (1987):

$$\frac{C_p}{R_g} = A + BT + CT^2 + DT^{-2} \qquad \textbf{(B.6)}$$

where R_g is the gas constant and T is in Kelvin. The constants have the following values:

A	$10^3 B$	$10^6 C$	$10^{-5} D$
3.280	0.593	-	0.040

B.6 Diffusion coefficient

The binary diffusion coefficient of the molecule pair A and B D_{AB} in SI-units is calculated from the Chapman-Enskog equation (Bird et al., 1960):

$$D_{AB} = 0.018829 \frac{\sqrt{T^3 \left(M_A^{-1} + M_B^{-1}\right)}}{p_t \sigma_{AB}^2 \Omega_{D,AB}} \qquad \textbf{(B.7)}$$

where M_i is the molecular weight of molecule i, T the temperature in Kelvin, p_t the total pressure, σ_{AB} the characteristic length in Angstrom, and Ω_D the dimensionless diffusion collision integral.

Two interaction parameters σ_{AB} and ϵ_{AB} are calculated from empirical formulas

$$\sigma_{AB} = \frac{\sigma_A + \sigma_B}{2} \qquad \textit{and} \qquad \epsilon_{AB} = (\epsilon_A \epsilon_B)^{1/2} \qquad \textbf{(B.8)}$$

In (B.8) the Lennard-Jones parameters for each molecule $\sigma_{LJ,i}$ and $\epsilon_{LJ,i}$ are estimated from the properties of the solid at the melting point T_m. The parameters are listed in table B.2 below.

$$\epsilon_{LJ}/k_b = 1.92 \cdot T_m \qquad \textit{and} \qquad \sigma_{LJ} = 1.222 \cdot V_m^{1/3} \qquad \textbf{(B.9)}$$

where V_m is the molar volume of the solid at the melting point in cm^3/mole.

The diffusion collision integral Ω_D is given by Reid et al. (1987):

$$\Omega_D = \frac{A}{(T^*)^B} + \frac{C}{\exp(DT^*)} + \frac{E}{\exp(FT^*)} + \frac{G}{\exp(HT^*)} \qquad \textbf{(B.10)}$$

where $T^* = T/(\epsilon_L/k_B)$ and

A=1.06036 B=0.15610 C=0.19300 D=0.47635
E=1.03587 F=1.52996 G=1.76474 H=3.89411

***Table B.2** Properties of KCl and air*

Species	M (g/mole)	T_m (K)	V_m (cm^3/mole)	σ_{LJ} (Å)	ϵ_{LJ}/k_B (K)
KCl	74.55	1045	49.05	4.47	2006
Air	28.97	-	-	3.62	97.0

Appendix C: Modelling the LFAC with FLUENT

The computational fluid dynamics (CFD) software package FLUENT can be used to simulate a number of problems in chemical engineering. It enables theoretical descriptions of mass and energy transfer, chemical reaction and more. In this work FLUENT has been used to simulate the laminar flow aerosol condenser (LFAC) used in the laboratory investigation of KCl (chapter 2). The models system is two concentric cylindrical tube, corresponding to the inner and outer Al_2O_3 tube of the LFAC. The temperature profile termed profile 2 measured in the LFAC (cf. section 4.2) is used as a boundary condition in FLUENT, i.e. the same input as is used in MONAERO (cf. chapter 3).

C.1 Equations

Fluent employs several standard flow and energy conservation equations, and those relevant for this simulation are described below in Cartesian coordinates (Fluent User's Guide vol. 4, 1996).

Mass conservation is given by

$$\frac{\partial \rho}{\partial t} + \frac{\partial}{\partial x_i}(\rho u_i) = S_m \qquad \textbf{(C.1)}$$

where ρ is the fluid density, u_i the velocity, and S_m a source term for mass added to the continuous phase. Momentum conservation is given by

$$\frac{\partial}{\partial t}(\rho u_i) + \frac{\partial}{\partial x_j}(\rho u_i u_j) = -\frac{\partial p}{\partial x_i} + \frac{\partial \tau_{ij}}{\partial x_j} + \rho g_i + F_i \qquad \textbf{(C.2)}$$

where p is the static pressure, τ_{ij} the stress tensor, and g_i and F_i are gravitational acceleration and external body forces in the i direction, respectively. Conservation of species i' is described by

$$\frac{\partial}{\partial t}(\rho m_{i'}) + \frac{\partial}{\partial x_i}(\rho u_i m_{i'}) = \frac{\partial}{\partial x_i}(J_{i',i}) + S_{i'} \qquad \textbf{(C.3)}$$

where $m_{i'}$ is the mass fraction of species i', $J_{i',i}$ the diffusive mass flux of species i' in the ith direction and $S_{i'}$ the net rate of production of species i' per unit volume from chemical reaction or contribution from the dispersed phase. FLUENT includes diffusion due to concentration gradients and thermal effects, neglecting diffusion due to pressure diffusion and external forces, and the diffusive mass flux $J_{i',i}$ is therefore given by

$$J_{i',i} = -\rho D_{i',m}\frac{\partial m_{i'}}{\partial x_i} - D_{i'}^{T}\frac{1}{T}\frac{\partial T}{\partial x_i} \qquad \textbf{(C.4)}$$

where $D_{i,m}$ is the diffusion coefficient for species i' in the gas and D_i^T is the thermal diffusion coefficient.

For the energy conservation equations FLUENT uses the static enthalpy h defined as

$$h = \sum_i m_i h_i \quad , \text{ where } h_i = \int_{T_{ref}}^{T} c_{p,i}\, dT \tag{C.5}$$

T_{ref} is a reference temperature and $c_{p,i}$ the specific heat at constant temperature of species i'. Diffusion due to pressure diffusion and external forces is again neglected, and the energy equation can be written as

$$\frac{\partial}{\partial t}(\rho h) + \frac{\partial}{\partial x_i}(\rho u_i h) = \frac{\partial}{\partial x_i}\left(k \frac{\partial T}{\partial x_i}\right) - \frac{\partial}{\partial x_i}\sum_j h_j J_j + \frac{\partial p}{\partial t} + u_i \frac{\partial p}{\partial x_i} + \tau_{ij}\frac{\partial u_i}{\partial x_j} + S_h \tag{C.6}$$

in which T is the temperature, τ_{ij} the viscous stress tensor, J_j the flux of species j', and k is the thermal conductivity. S_h is a source term describing enthalpy sources due to chemical reaction, radiation and heat exchange with a dispersed second phase.
In a conducting solid region (e.g. the inner tube wall) FLUENT employs an equation of conduction which includes heat flux resulting from conduction and volumetric heat sources within the solid, given by

$$\frac{\partial}{\partial t}\rho_w h_w = \frac{\partial}{\partial x_i} k_w \frac{\partial T}{\partial x_i} + \dot{q}''' \tag{C.7}$$

where ρ_w is the wall density, h_w wall enthalpy, k_w wall conductivity, T wall temperature, and $\dot{q}'''$ the volumetric heat source. Equation (C.7) is solved simultaneously with (C.6).

The physical parameters necessary for solution of the flow and heat transfer equations are calculated by FLUENT according to the user's specifications. In this case temperature-dependent expressions are used, calculated from kinetic theory.

The equations described above are solved numerically using a finite element method. For further reference, see FLUENT user's guide (1996).

C.2 The grid

FLUENT requires boundaries within which the calculations are to take place. These are defined by a grid which contains information on the physical system and phases included in the calculations, starting values, boundary conditions and models for flow and heat transfer. In this case the system is a cylindrical tube, and a rotational symmetry option is used. Figure C.1 shows a schematic view of the grid used. The grid will not be further discussed here.

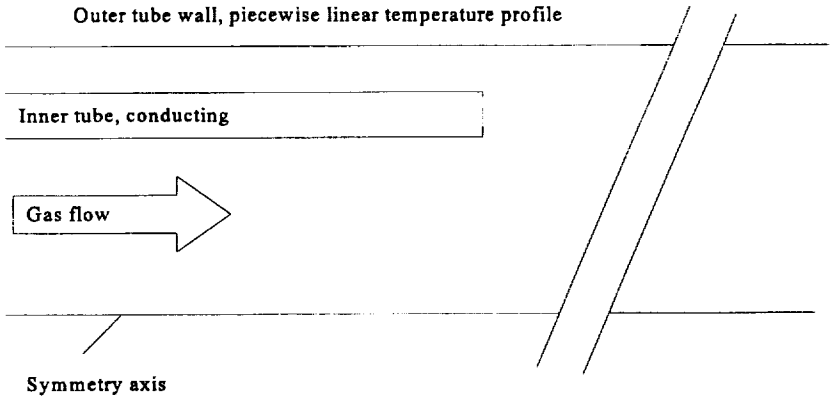

Figure C.1 *Schematic view of laminar flow aerosol condenser used for simulations with FLUENT.*

Figure C.2 shows a cross-sectional view of the LFAC from FLUENT, where the gas temperature is shown as coloured zones. The region in the LFAC from the inner tube outlet to an axial position of 120 cm from the furnace inlet is shown. The image has been enlarged five times in the radial direction.

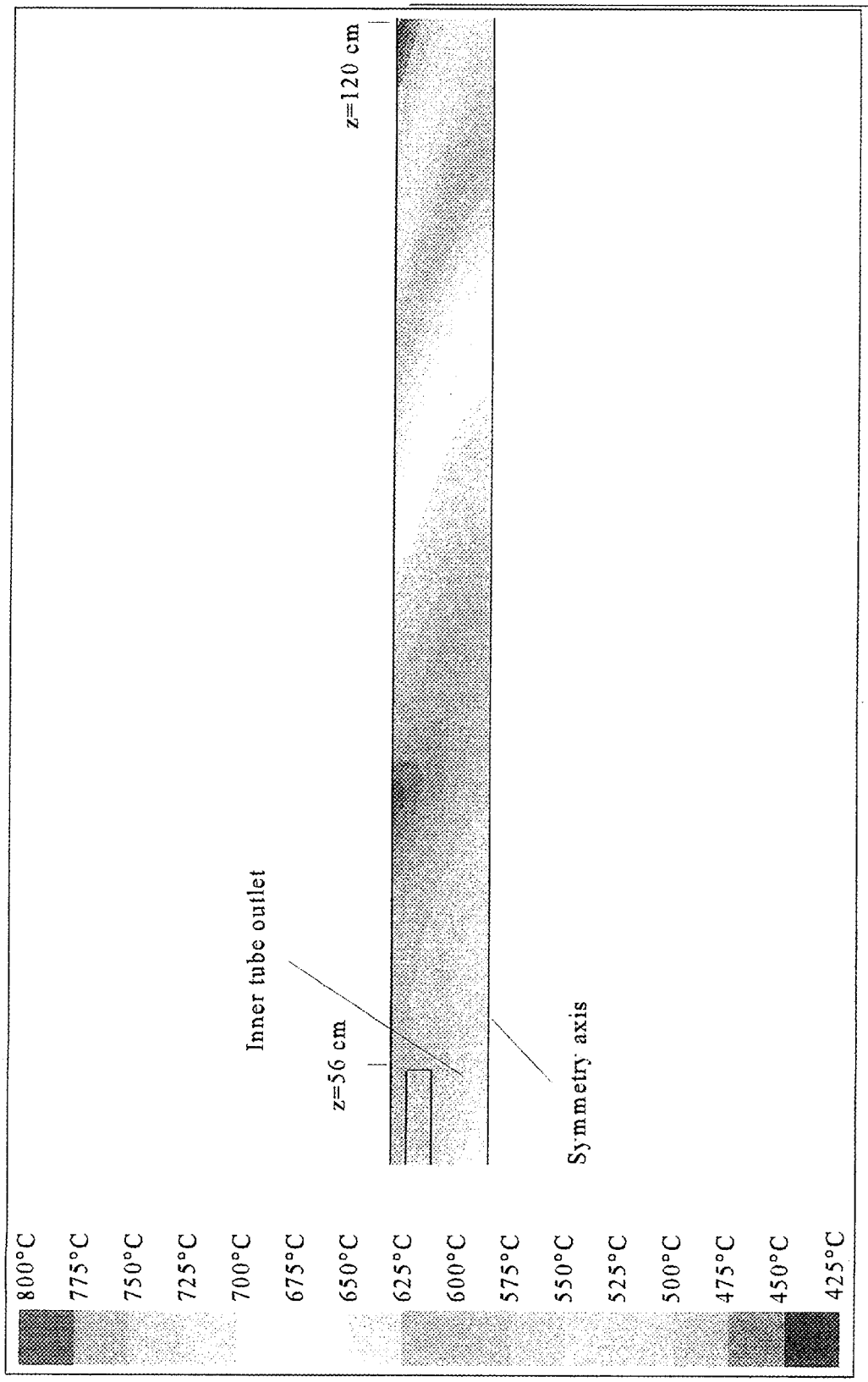

***Figure C.2** Cross-section of LFAC from FLUENT. Gas temperature variation in axial and radial direction. Wall temperature profile 2. Gas flow 4 l/min at 20°C.*

Appendix D: Particle penetration in the ejector probe

An experimental and theoretical investigation of the particle penetration in the ejector probe used in the field experiments has been performed.

D.1 Particle filtering at the probe inlet

The probe is inserted perpendicular to the direction of flow of the flue gas. The 90° angle between gas velocity and probe leads to an inertial filtering of large particles, since these are less likely to be able to follow the gas streamlines int the probe. For a thin-walled probe the aspiration efficiency (the fraction of particles that enter the probe) is defined by (Vincent, 1989)

$$A = \left(1 + 4\lambda St\sqrt{U/U_t}\right)^{-1} \qquad \textbf{(D.1)}$$

where the Stokes number St is given by

$$St = \frac{d_p^2 \rho_p U}{18\mu d_t} \qquad \textbf{(D.2)}$$

where d_p is the particle diameter, ρ_p the particle density, U the gas velocity, U_t the mean gas velocity in the probe, μ the viscosity and d_t the probe inner diameter. λ is an experimentally determined parameter, the value of which has been set to 2.1 ± 0.9. The gas velocity in the flue

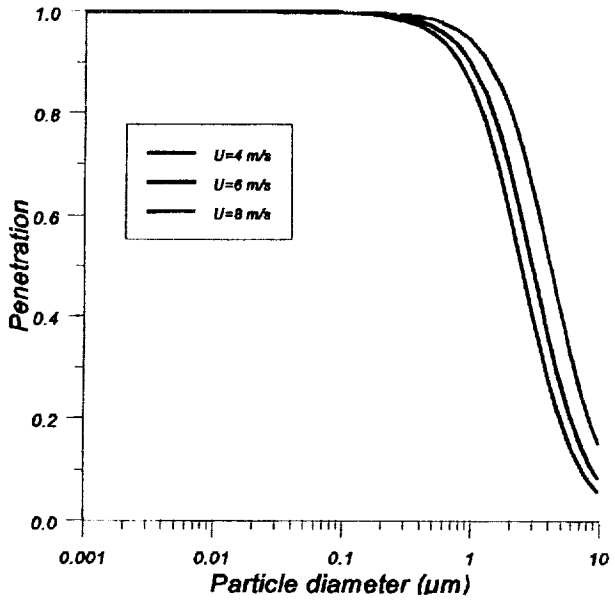

***Figure D.1** Penetration of particles in probe tip placed perpendicular to the direction of flow in the flue gas channel.*

determined parameter, the value of which has been set to 2.1 ± 0.9. The gas velocity in the flue gas channel has been estimated to 6 m/s (Pedersen and Røkke, 1996), which leads to a penetration of particles at the probe inlet depicted in figure D.1. The sensitivity to the flue gas velocity is illustrated by curves for velocities of 4 and 8 m/s, respectively. Figure D.1 shows that 100% of the particles with diameter less than 0.2 μm enter the probe, and 90% of the particles 1 μm in diameter.

D.2 Calculated penetration

A simplified representation of the probe is used in calculating the penetration of particles inside the probe and tubing leading to the analyzing equipment (figure D.2). Total penetration P is calculated as

$$P = \prod_i P_i, \qquad i = A,B,C,D,E \tag{D.3}$$

The penetration in probe sections A, B, D, and E is calculated using a model for diffusional loss by Brownian motion in a isothermal straight tube with laminar flow. The particle concentration N_p is a function of axial and radial position, l and r, respectively. Neglecting axial diffusion yields the equation of convective diffusion

$$v_z r \frac{\partial N_p}{\partial l} = D_p \frac{\partial}{\partial r}\left(r \frac{\partial N_p}{\partial r} \right) \tag{D.4}$$

with the boundary conditions

$$l=0 : N_p=N_{p0}, \qquad r=0 : \frac{\partial N_p}{\partial r} = 0, \qquad r=R : N_p=0 \tag{D.5}$$

For laminar flow in a tube, the velocity profile is described by (Bird et al., 1960):

$$v_z = 2U_t\left(1-(r/R)^2\right) \tag{D.6}$$

The differential equation (D.4) can be transformed to dimensionless variables and solved numerically using the method of orthogonal collocation (Villadsen and Michelsen, 1978). For further details, the reader is referred to Christensen, appendix B (1995).

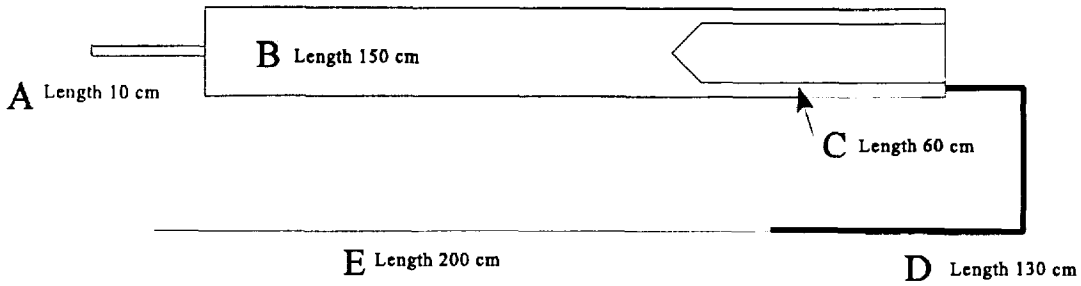

***Figure D.2** Schematic of ejector probe geometry as assumed for penetration calculations. **A**: Capillary tube. **B**: Upper probe tube. **C**: Annulus at cooling insert. **D, E**: Tygon tubes, 7/8" and 1/4" outer diameter, respectively.*

Penetration in section C (figure D.2) is calculated from a similar model of Brownian diffusion in an isothermal annulus with laminar flow. Since the annulus slit width δ_s is smaller than the annulus diameter, the equations are derived using planar geometry, where particles are lost both to inner and outer surfaces. Particle concentration N_p is again a function of axial and radial position l and r.

Assuming that axial diffusion is negligible yields an equation of convective diffusion of the form

$$v_z \frac{\partial N_p}{\partial l} = D_p \frac{\partial^2 N_p}{\partial r^2} \qquad \textbf{(D.7)}$$

with boundary conditions

$$l=0 : N_p=N_{p0}\,, \qquad r=0 : \frac{\partial N_p}{\partial r} = 0\,, \qquad r=\frac{\delta_s}{2} : N_p=0 \qquad \textbf{(D.8)}$$

The laminar velocity profile in the annular slit has the form

$$v_z = \frac{3}{2} U_l \left(1 - (2r/\delta_s)^2\right) \qquad \textbf{(D.9)}$$

(Bird et al., 1960), U_l is again the mean gas velocity. The differential equation (D.7) can be transformed to dimensionless variables and solved by orthogonal collocation (Villadsen and Michelsen, 1978). For further details, see Christensen, appendix B (1995).

An experimental investigation of the penetration in the probe is also performed. Submicron aerosol number size distributions are measured upstream and downstream from the probe, and the penetration $P(d_p)$ calculated as

$$P(d_p) = \frac{\varphi^a(d_p,exit)}{\varphi_a(d_p,inlet)} \qquad \textbf{(D.10)}$$

Here d_p the particle diameter, and φ_a the aerosol size distribution independent of temperature referred to a density ρ_r. In the laboratory measurements of the penetration an aerosol is generated from a solution of NaCl in a TSI model 3076 atomizer, and a fraction thereof dried in two serial diffusion driers. The aerosol size distribution is measured upstream and downstream from the probe under identical conditions, and the penetration calculated from equation D.10, where φ_a

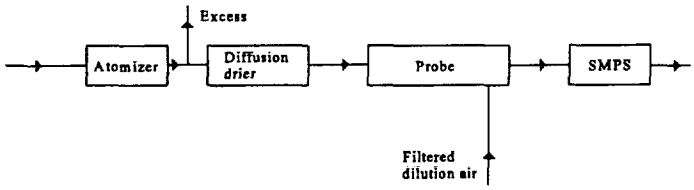

Figure D.3 *Laboratory setup for measurement of aerosol penetration in the field measurement probe. The aerosol size distribution is measured upstream as well as downstream from the probe using the SMPS system.*

is a weighted average of at least four measurements. The results are uncertain for values of d_p far from the size distribution peak, and therefore several concentrations of NaCl are used to cover the relevant particle size range. The experimental setup used for this investigation is shown in figure D.3.

Figure D.4 shows the penetration at 25°C of particles in the five individual sections of the simplified probe geometry shown in figure D.2, as well as the total penetration. The major particle loss is seen to take place in the annular slit and in the final tube E. It must be remembered that this tube is not used in the field experiments. Figure D.5 shows a comparison of measured and calculated diffusional particle loss in the probe. The deviation between the two is relatively small in the relevant size range. The models underestimate the particle loss of the smallest particles, probably due to the neglecting turbulence, which will enhance particle diffusional removal.

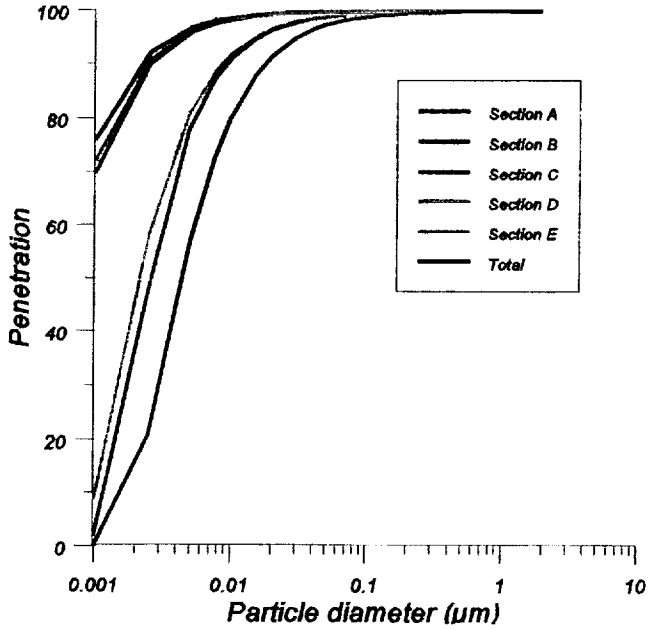

***Figure D.4** : Theoretical penetration in the ejector probe, total and in individual sections A-E (cf. Figure D.5).Temperature 25°C.*

These calculations and experiments have all been performed at a temperature of 25°C. Calculations have also been carried out with a high temperature input to simulate the conditions under which the probe was used in the field experiments. The results were similar to those shown, although with a slightly smaller penetration (data not shown).

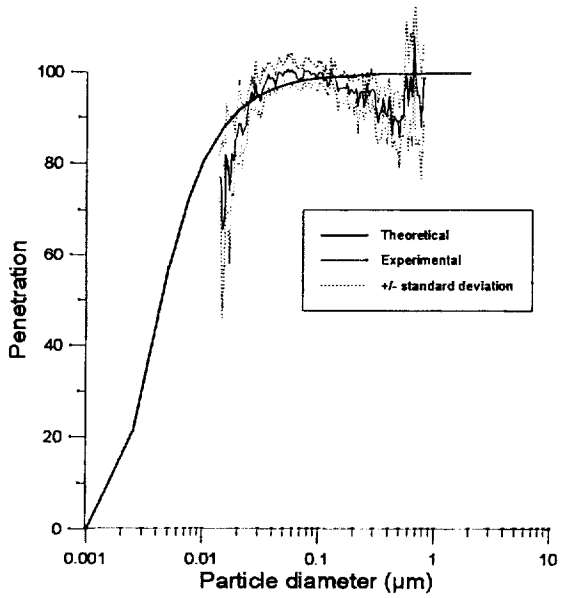

***Figure D.5** : Total theoretical and experimental penetration in the ejector probe. NaCl-aerosol, temperature 25°C.*

Appendix E: Survey of field experiments

The field experiments took place in early 1996 and early 1997. Below is listed a survey of the complete field experiments, including analyses performed on impactor foils.

***Table E.1**: Overview of aerosol field experiments performed on unit one of the Midtkraft Studstrup power plant. #SMPS indicates the total number of SMPS (scanning mobility particle sizer system) measurements performed on that day. No SMPS measurements were carried out in experiments 3a, 8a, and 9a. % load indicates nominal percentage of total load of 380 MW_{Th}. % straw indicates nominal straw input on an energy basis. Al indicates aluminum impactor foil, Cu copper foil, PTFE Teflon foil, and +/- presence or absence, respectively, of grease on foil surface.*

Series	Coal	%Load/ %straw	Date	Time	#SMPS	Impactor set no. Foil type	Analysis on foils
1	Type A	50/20	03/20/96	9.30-15.47	25	10, Al+	-
						11, Al+	Chem
			03/21/96	8.52-14.58	25	12, Al+	Chem
						31, Al-	EDX
2	Type A	75/20	04/10/96	10.55-15.47	16	14, Al+	Chem
						28, Cu+	EDX
			04/11/96	8.07-12.36	22	16, Al+	Chem
						29, Cu+	EDX
						34, Al-	
3	Type A	100/20	03/27/96	9.07-14.42	27	13, Al+	Chem
						32, Al-	
			03/28/96	8.11-11.19	25	27, Cu+	EDX
						33, Al-	
4	Type A	100/10	04/17/96	10.35-12.48	11	19, Al+	Chem
						30, Cu+	
			04/18/96	7.46-12.45	21	20, Al+	Chem
						35, Al-	
						37, Cu+	EDX
5	Type A	100/0	04/24/96	-	-	-	-
			04/25/96	7.28-13.50	28	22, Al+	Chem
						36, Al-	
						38, Cu+	EDX
6	Type A	75/0	05/08/96	9.26-12.46	13	41, Cu+	EDX
						53, Al+	Chem
			05/09/96	7.53-12.53	19	24, Al+	Chem
						42, Cu+	
7	Type A	50/0	05/01/96	10.54-12.50	11	39, Cu+	EDX
						51, Al+	Chem
			05/02/96	08.20-12.54	24	23, Al+	Chem
						40, Cu+	
						45, Al-	

Series	Coal	%Load/ %straw	Date	Time	#SMPS	Impactor set no. Foil type	Analysis on foils
8	Type B	70/0	05/15/96	8.15-16.21	28	25, Al+ 43, Cu+ 48, Al-	Chem EDX
3a	Type A	100/20	29/01/97	7.46-15.32	0	S1, Cu+ S2, Cu+ S7, PTFE	EDX NAA
			30/01/97	7.52-11.25	0	S3, Cu+ S8, PTFE	
8a	Type C	100/0	02/05/97	9.52-19.19	0	S4, Cu+ S5, Cu+ S6, Cu+ S9, PTFE	EDX NAA
9a	Type C	100/20	02/07/97	7.38-15.07	0	S10, PTFE S12, Cu+ S13, Cu+	NAA EDX

Appendix F: Number size distributions from co-firing of coal and straw

Series 1

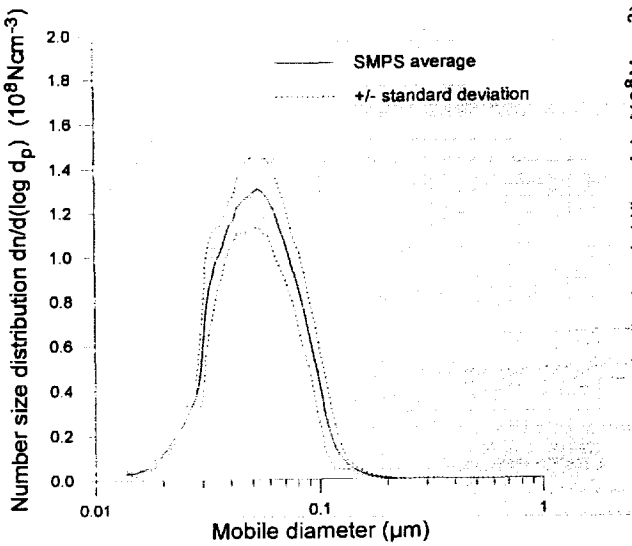

Figure F.1 *Average number size distribution. 25 SMPS measurements. Series 1, day 1*

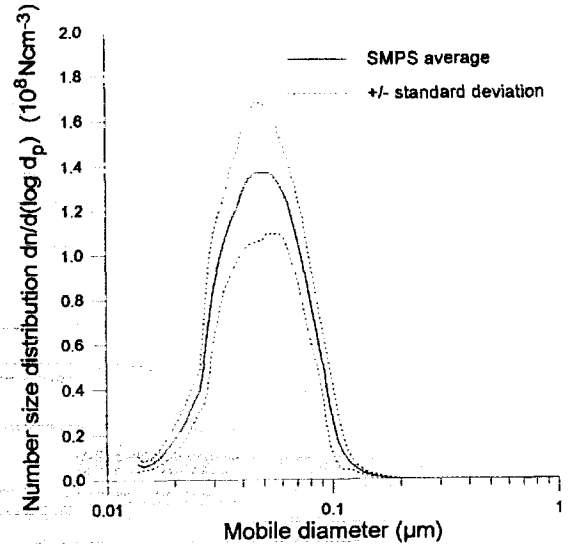

Figure F.2 *Average number size distribution. 25 SMPS measurements. Series 1, day 2*

Series 2

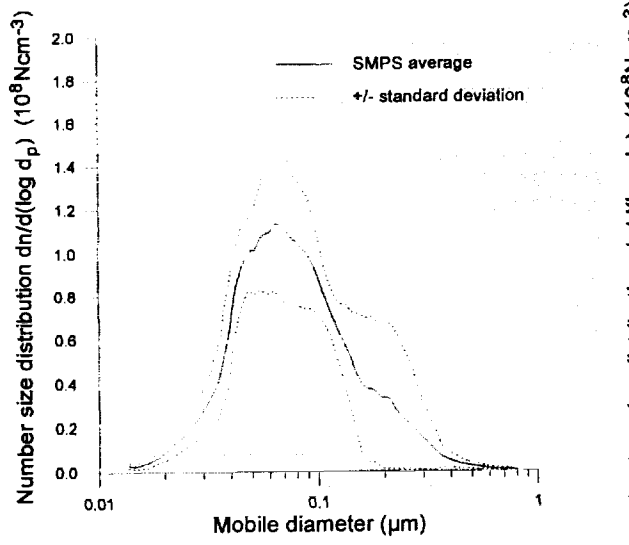

Figure F.3 *Average number size distribution. 16 SMPS measurements. Series 2, day 1*

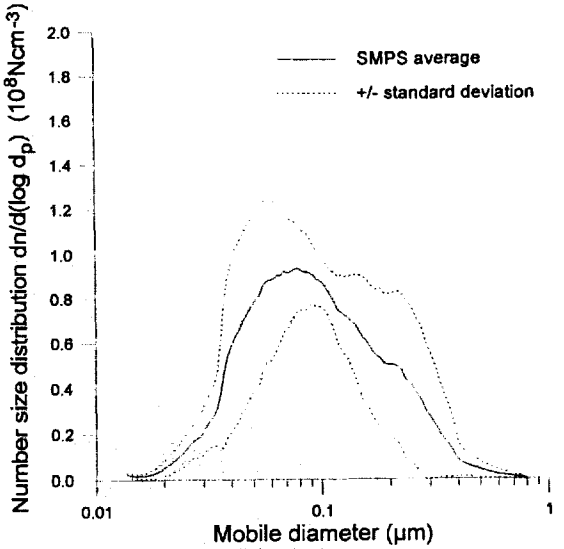

Figure F.4 *Average number size distribution. 22 SMPS measurements. Series 2, day 2*

Series 3

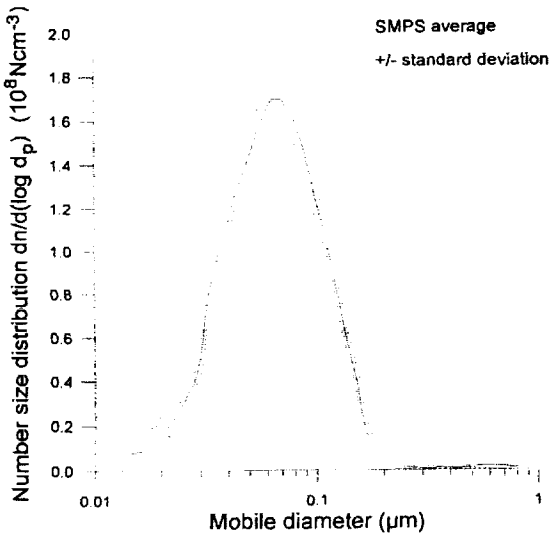

Figure F.5 *Average number size distribution. 27 SMPS measurements. Series 3, day 1*

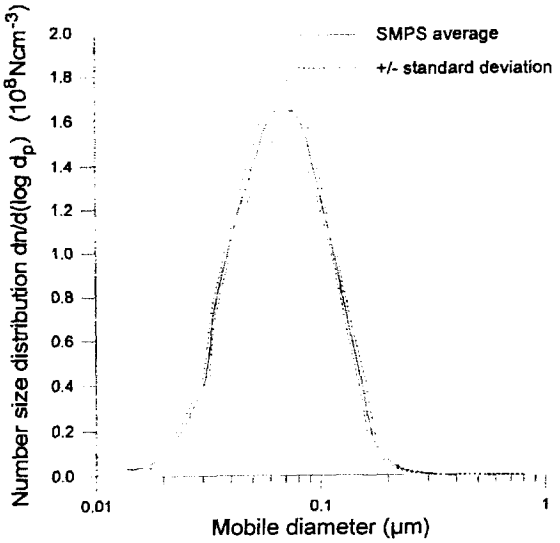

Figure F.6 *Average number size distribution. 25 SMPS measurements. Series 3, day 2*

Series 4

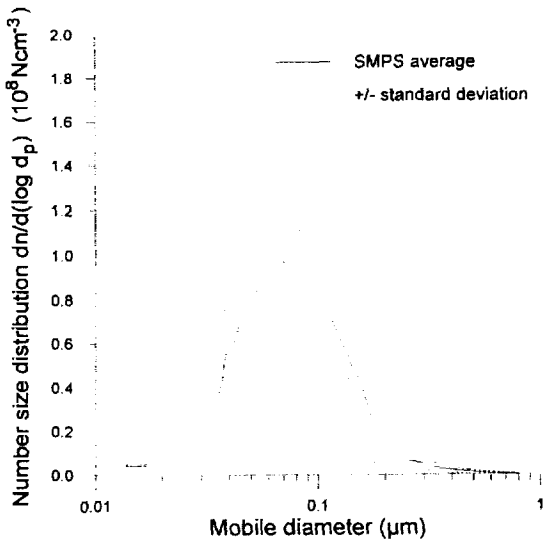

Figure F.7 *Average number size distribution. 11 SMPS measurements. Series 4, day 1*

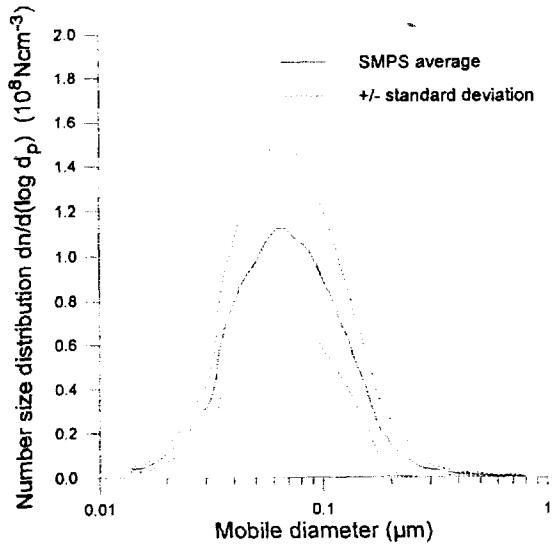

Figure F.8 *Average number size distribution. 21 SMPS measurements. Series 4, day 2*

Series 5

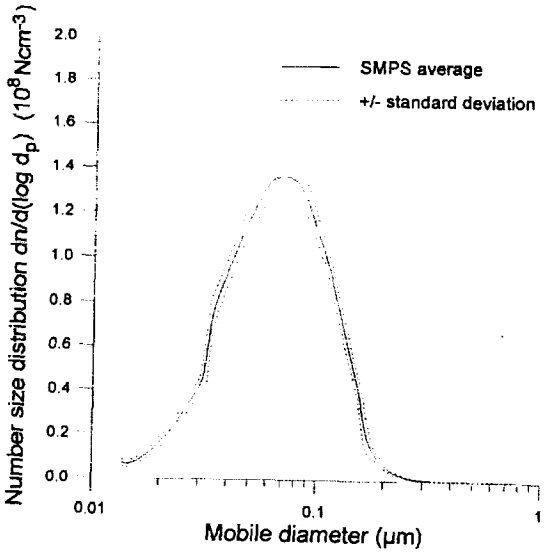

Figure F.9 *Average number size distribution. 28 SMPS measurements. Series 5, day 2*

Series 6

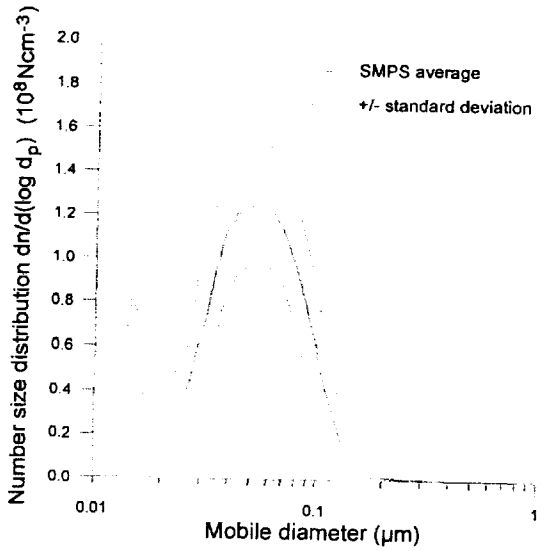

Figure F.10 *Average number size distribution. 13 SMPS measurements. Series 6, day 1. Deviating distributions not included, cf. appendix G.*

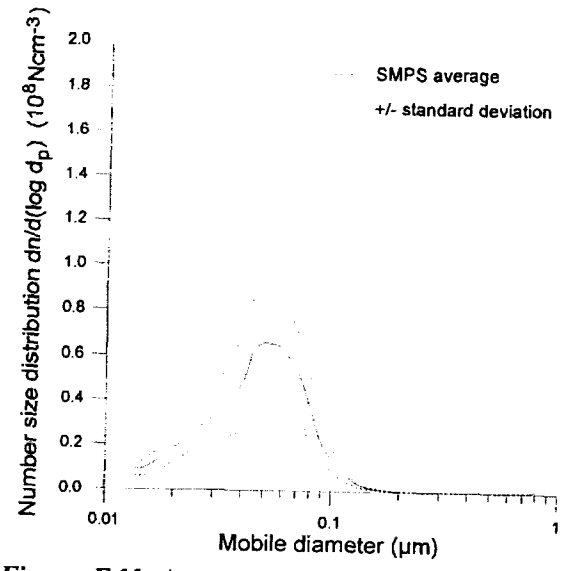

Figure F.11 *Average number size distribution. 19 SMPS measurements. Series 6, day 2. Deviating distributions not included, cf. appendix G.*

Series 7

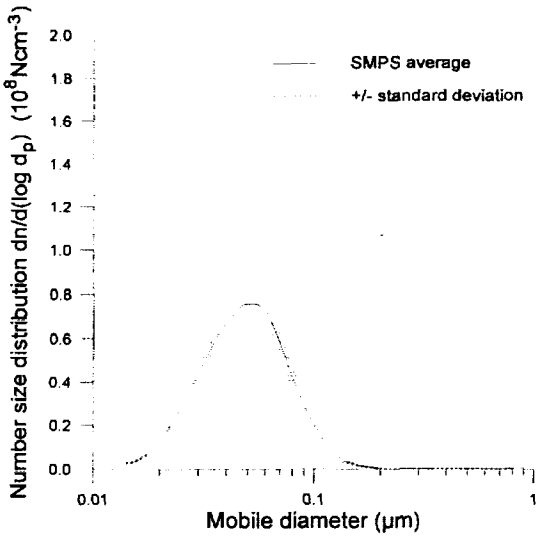

Figure F.12 *Average number size distribution. 11 SMPS measurements. Series 7, day 1*

Series 8

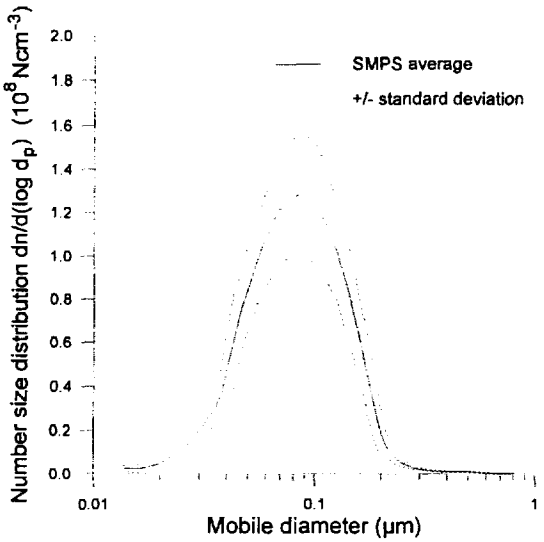

Figure F.13 *Average number size distribution. 28 SMPS measurements. Series 8, day 1. Deviating distributions not included, cf. Appendix G.*

Appendix G: Average number concentration from co-firing of coal and straw

Series 1

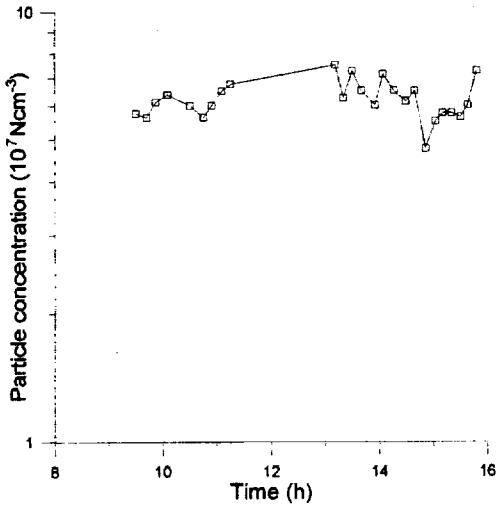

Figure 1.1 *Total number concentration from SMPS measurements. Series 1, day 1*

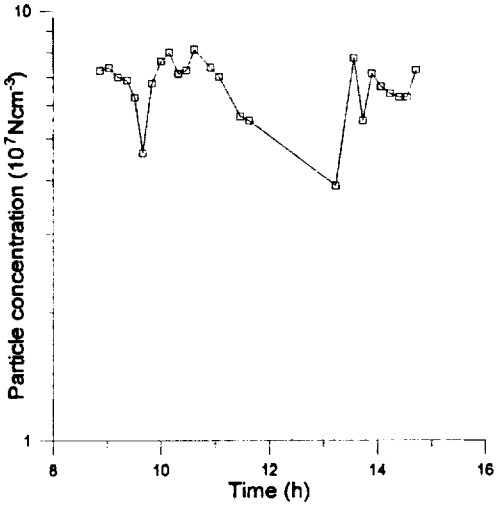

Figure 1.2 *Total number concentration from SMPS measurements. Series 1, day 2*

Series 2

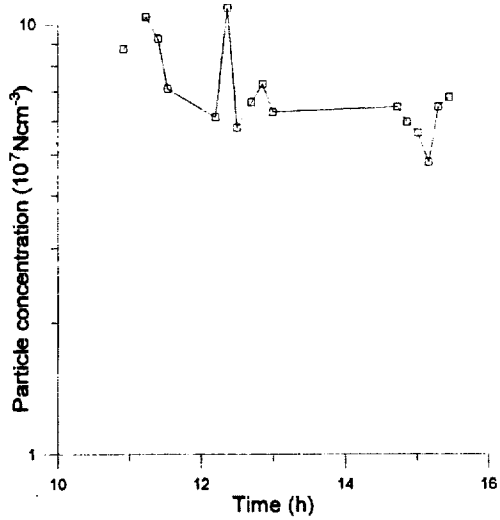

Figure 1.3 *Total number concentration from SMPS measurements. Series 2, day 1*

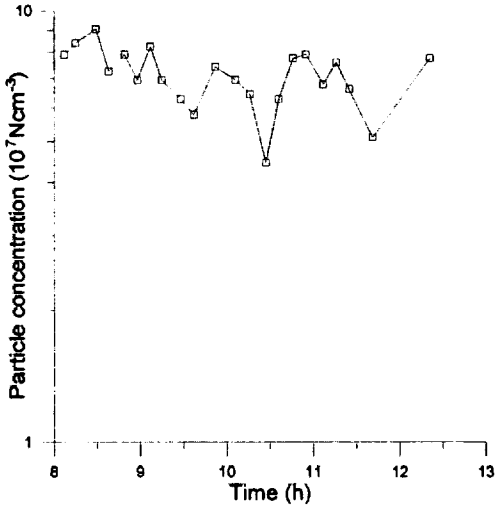

Figure 1.4 *Total number concentration from SMPS measurements. Series 2, day 2*

Series 3

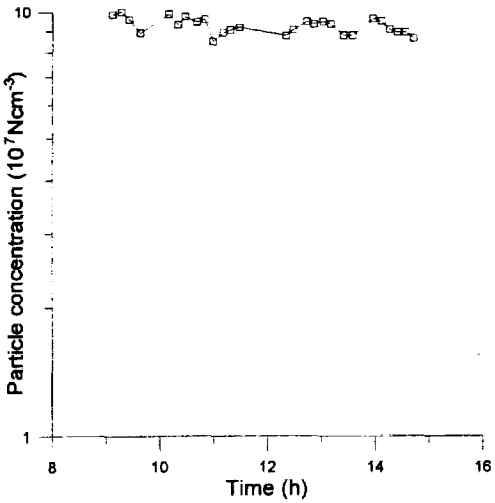

Figure 1.5 *Total number concentration from SMPS measurements. Series 3, day 1*

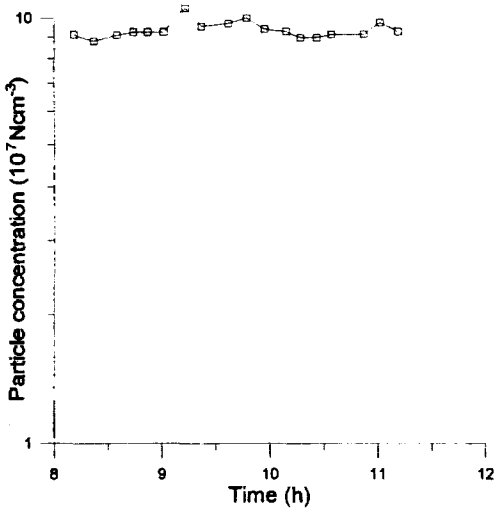

Figure 1.6 *Total number concentration from SMPS measurements. Series 3, day 2*

Series 4

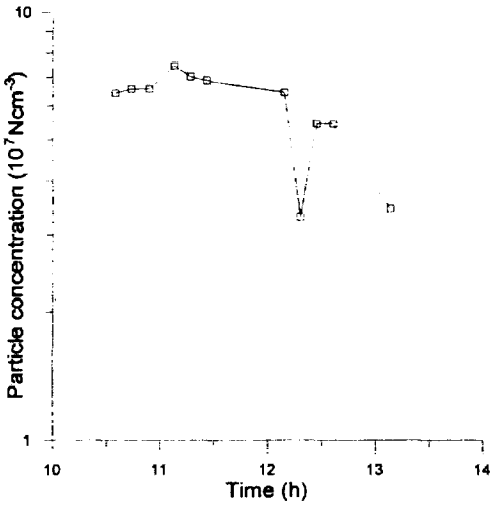

Figure 1.7 *Total number concentration from SMPS measurements. Series 4, day 1*

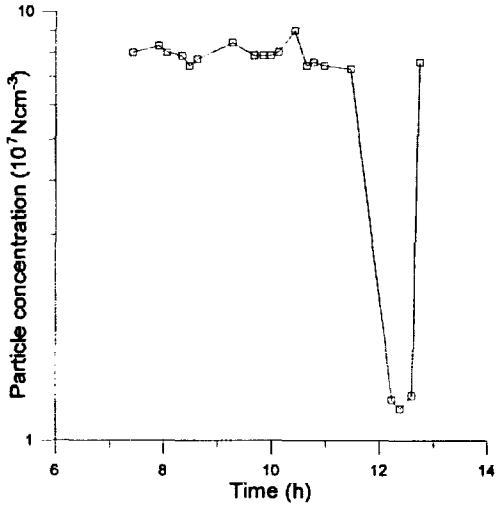

Figure 1.8 *Total number concentration from SMPS measurements. Series 4, day 2*

Series 5

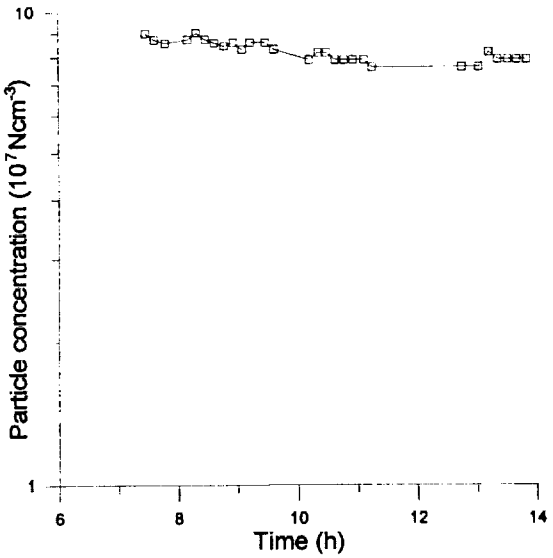

Figure 1.9 *Total number concentration from SMPS measurements. Series 5, day 2*

Series 6

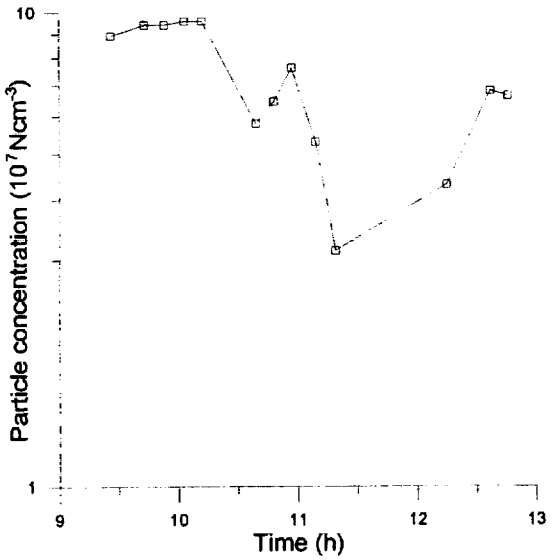

Figure 1.10 *Total number concentration from SMPS measurements. Series 6, day 1*

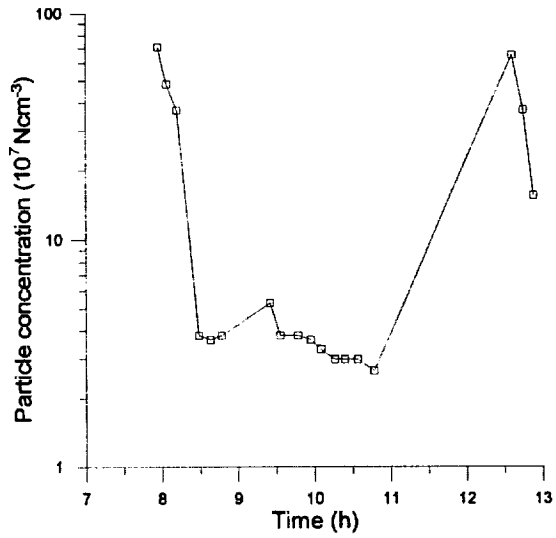

Figure 1.11 *Total number concentration from SMPS measurements. Series 6, day 2*

Series 7

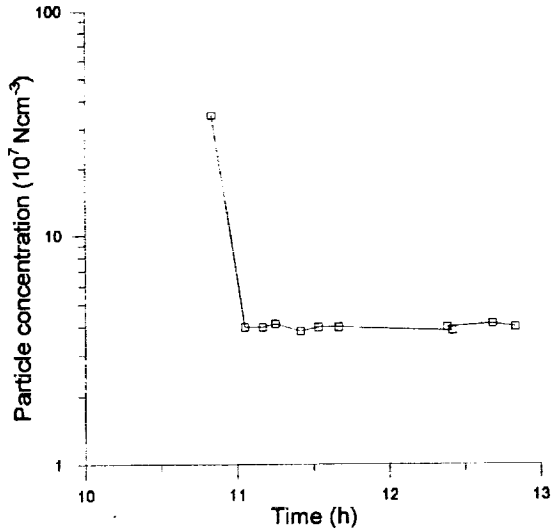

Figure 1.12 *Total number concentration from SMPS measurements. Series 7, day 1*

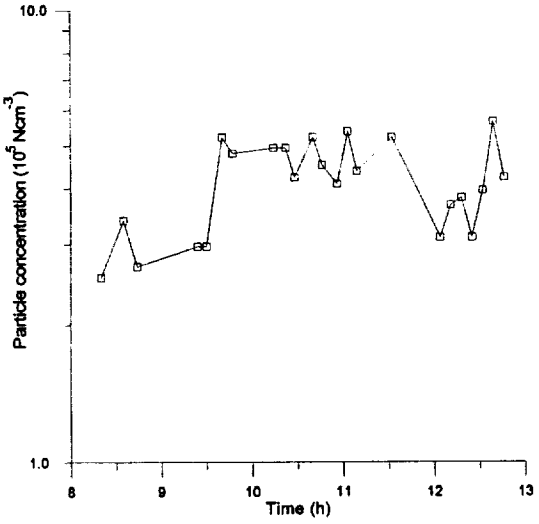

Figure 1.13 *Total number concentration from SMPS measurements. Series 7, day 2*

Series 8

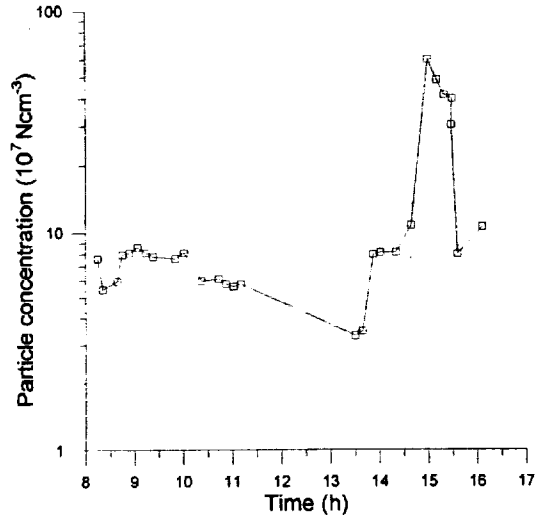

Figure 1.14 *Total number concentration from SMPS measurements. Series 8, day 1*

Appendix H: Fly ash mass distributions from co-firing of coal and straw

Series 1

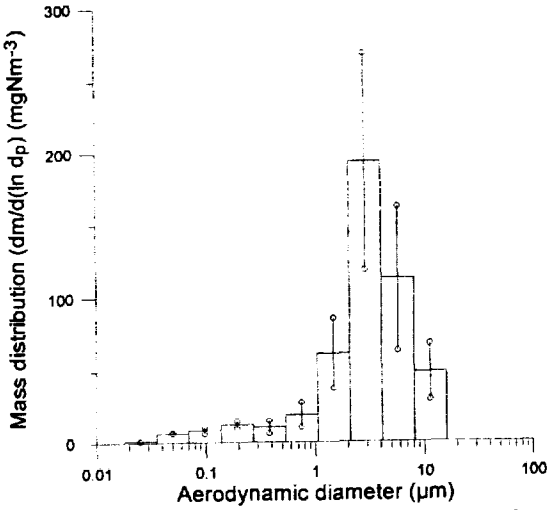

Figure H.1 *Mass distribution of fly ash ,all impactor stages. Series 1, day 1.*

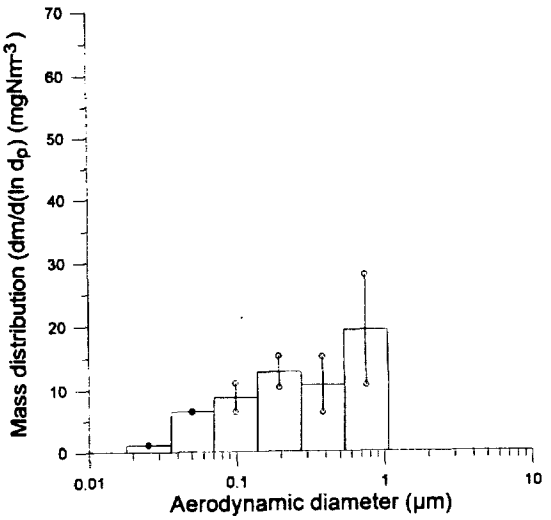

Figure H.2 *Mass distribution of fly ash, impactor stages 1-6. Series 1, day 1*

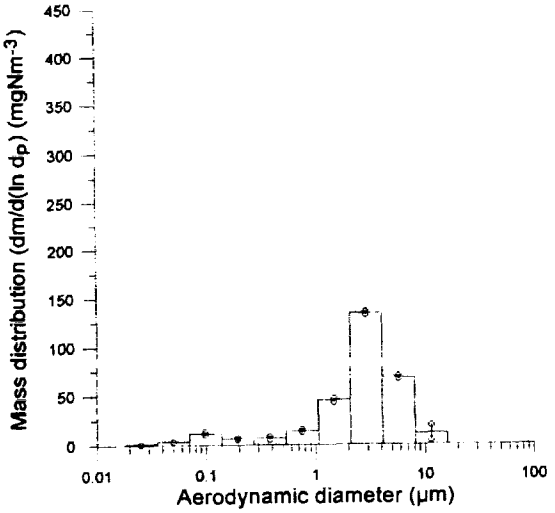

Figure H.3 *Mass distribution of fly ash, all impactor stages. Series 1, day 2*

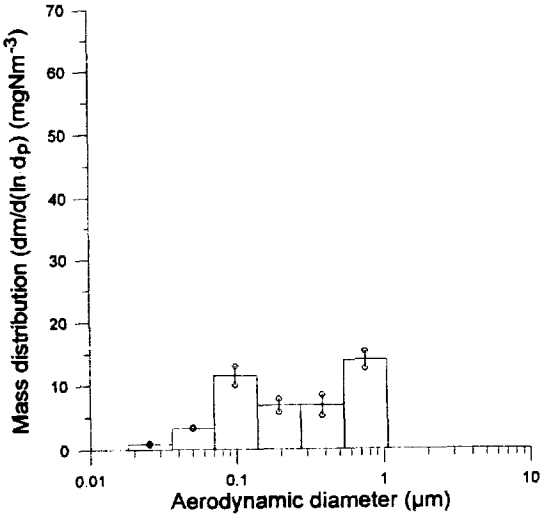

Figure H.4 *Mass distribution of fly ash, impactor stages 1-6. Series 1, day 2*

Series 2

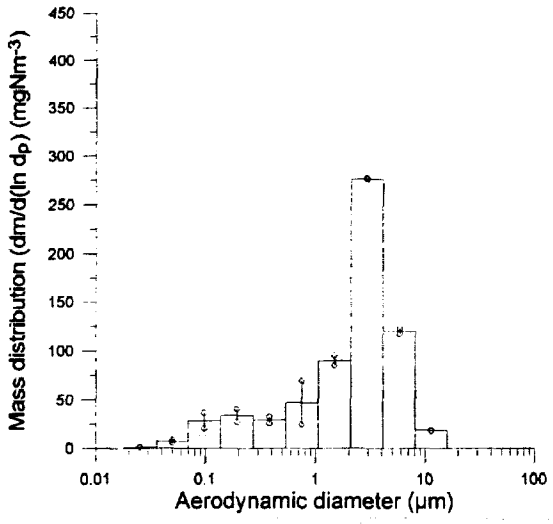

Figure H.5 *Mass distribution of fly ash, all impactor stages. Series 2, day 1*

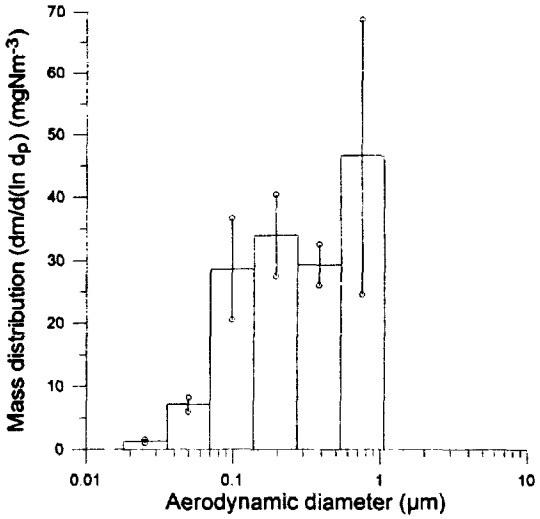

Figure H.6 *Mass distribution of fly ash, impactor stages 1-6. Series 2, day 1*

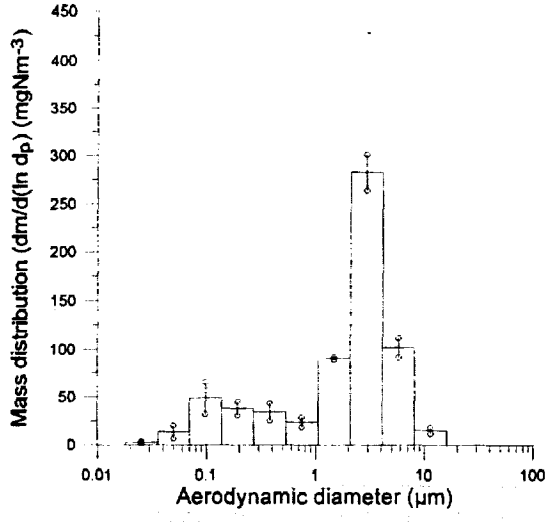

Figure H.7 *Mass distribution of fly ash, all impactor stages. Series 2, day 2*

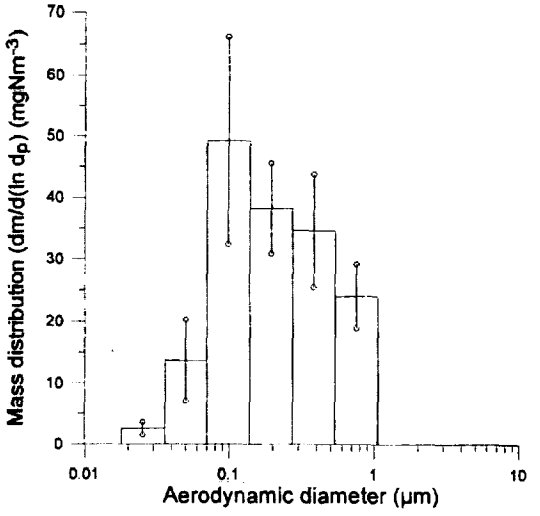

Figure H.8 *Mass distribution of fly ash, impactor stages 1-6. Series 2, day 2*

Series 3

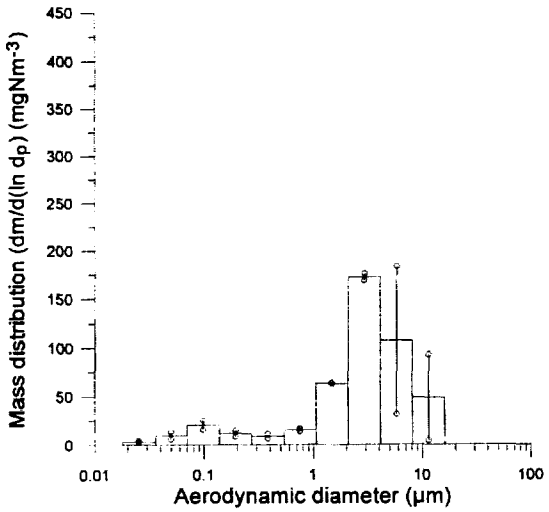

Figure H.9 *Mass distribution of fly ash, all impactor stages. Series 3, day 1*

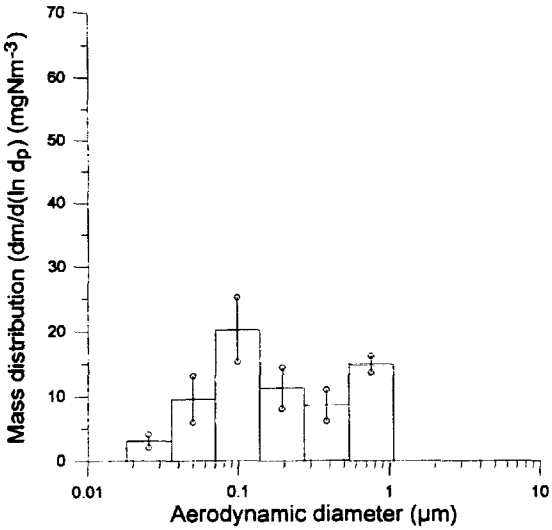

Figure H.10 *Mass distribution of fly ash, impactor stages 1-6. Series 3, day 1*

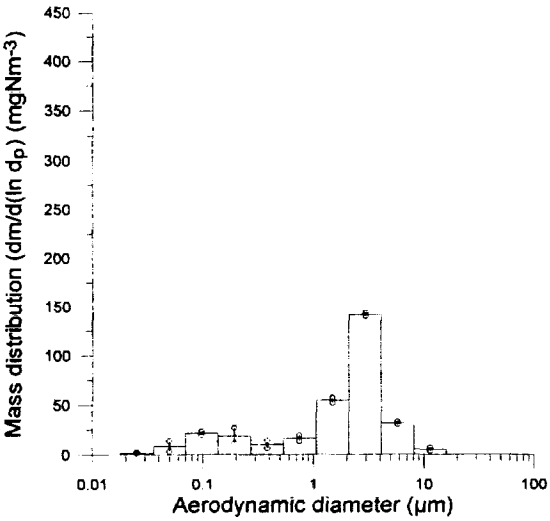

Figure H.11 *Mass distribution of fly ash, all impactor stages. Series 3, day 2*

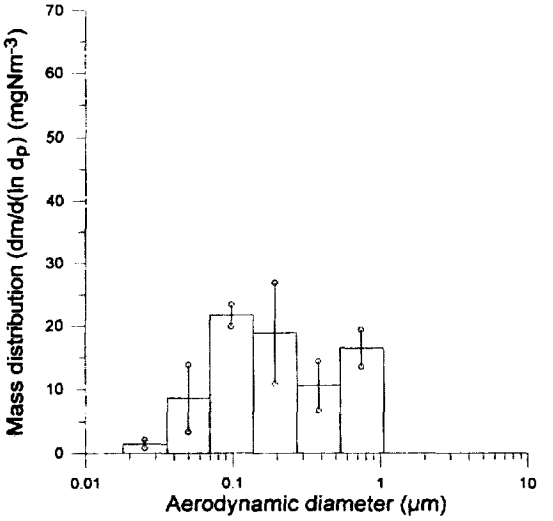

Figure H.12 *Mass distribution of fly ash, impactor stages 1-6. Series 3, day 2*

Series 4

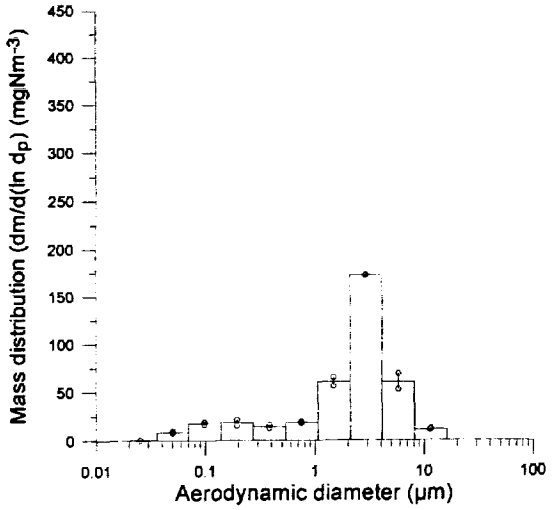

Figure H.13 *Mass distribution of fly ash, all impactor stages. Series 4, day 1*

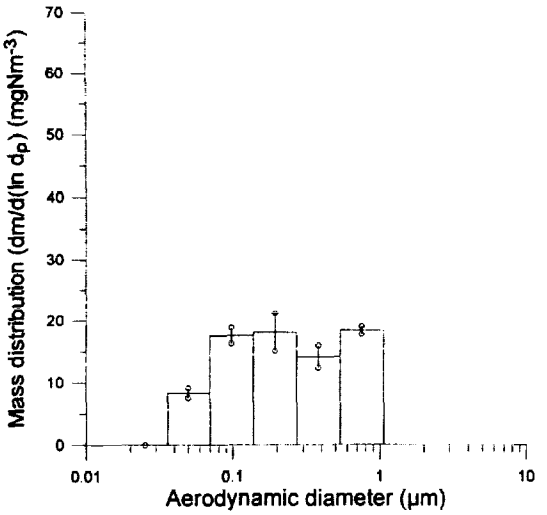

Figure H.14 *Mass distribution of fly ash, impactor stages 1-6. Series 4, day 1*

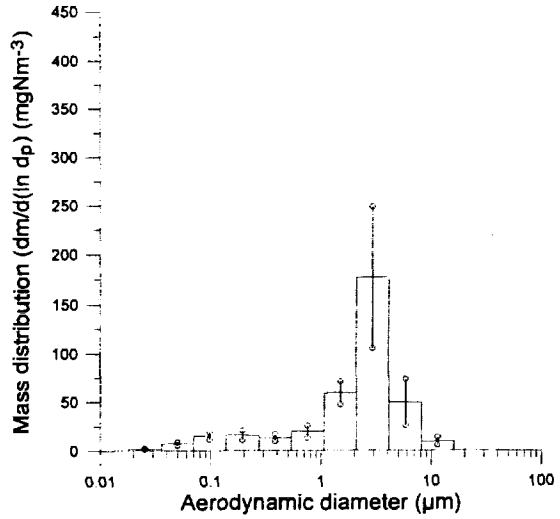

Figure H.15 *Mass distribution of fly ash, all impactor stages. Series 4, day 2*

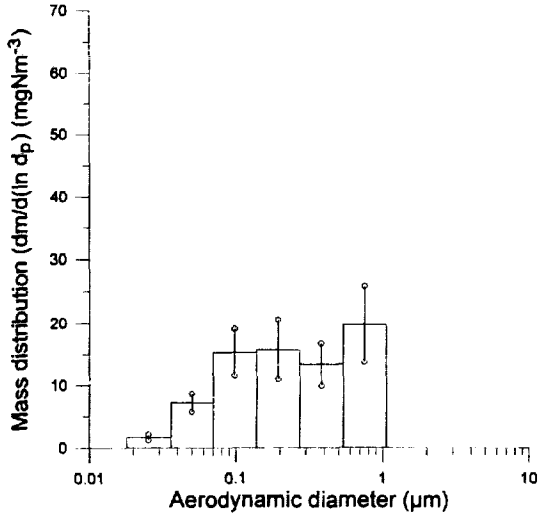

Figure H.16 *Mass distribution of fly ash, impactor stages 1-6. Series 4, day 2*

Series 5

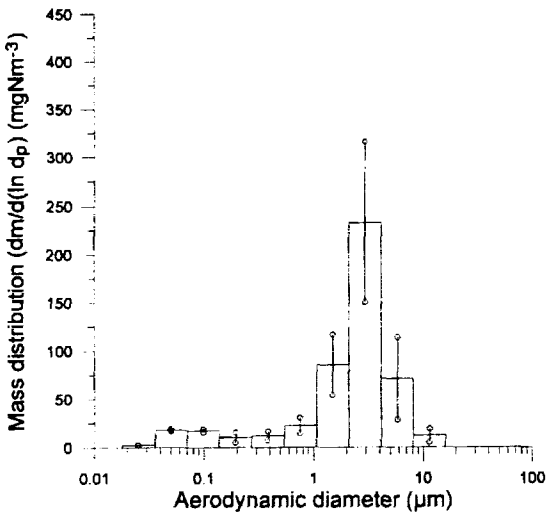

Figure H.17 *Mass distribution of fly ash, all impactor stages. Series 5, day 2*

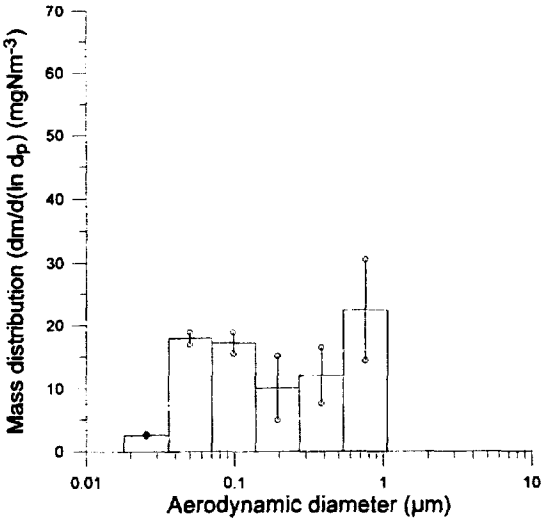

Figure H.18 *Mass distribution of fly ash, impactor stages 1-6. Series 5, day 2*

Series 6

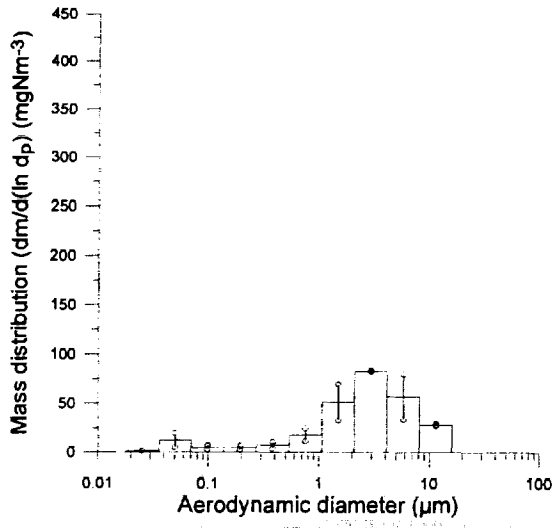

Figure H.19 *Mass distribution of fly ash, all impactor stages. Series 6, day 1*

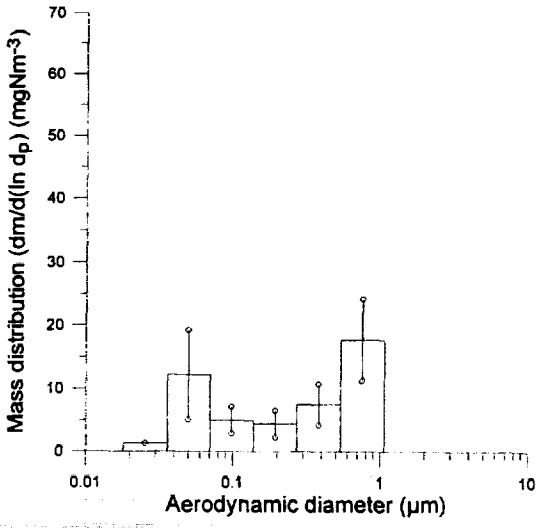

Figure H.20 *Mass distribution of fly ash, impactor stages 1-6. Series 6, day 1*

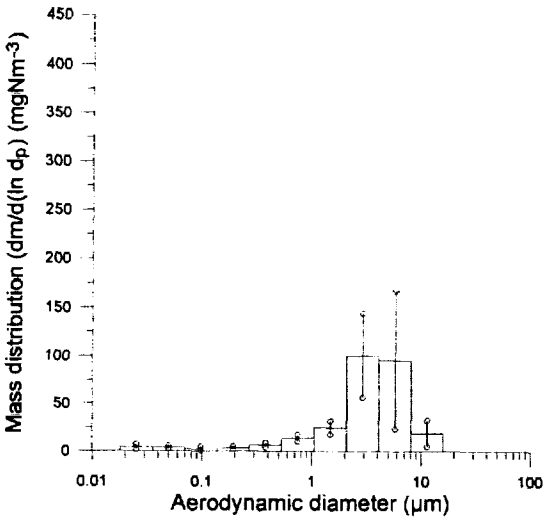

Figure H.21 *Mass distribution of fly ash, all impactor stages. Series 6, day 2*

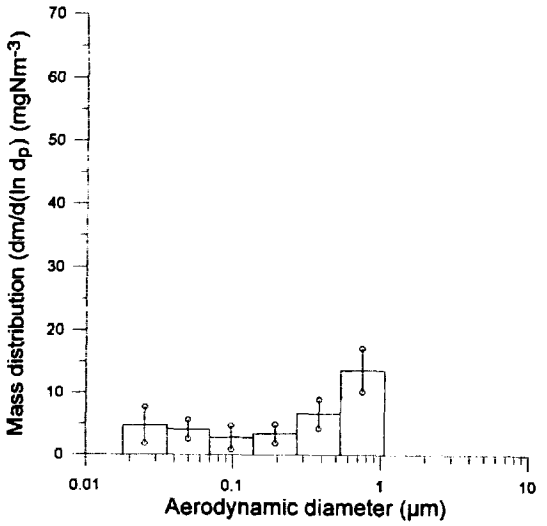

Figure H.22 *Mass distribution of fly ash, impactor stages 1-6. Series 6, day 2*

Series 7

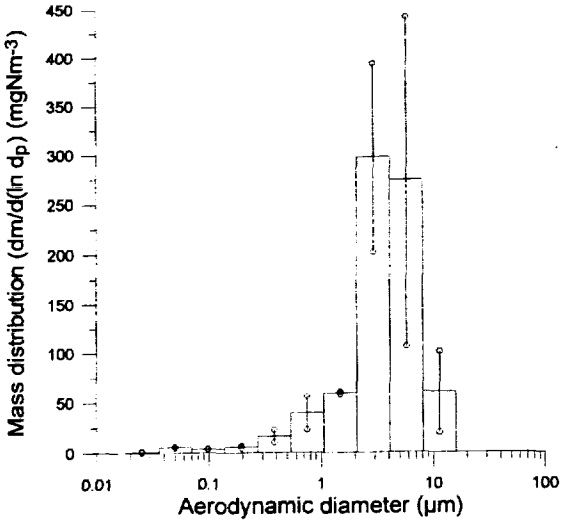

Figure H.23 *Mass distribution of fly ash, all impactor stages. Series 7, day 1*

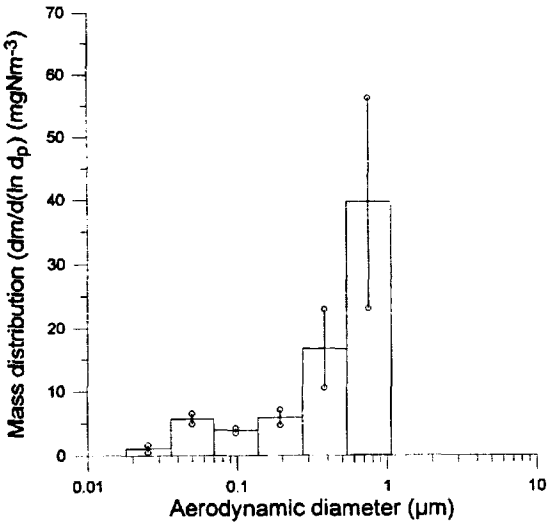

Figure H.24 *Mass distribution of fly ash, impactor stages 1-6. Series 7, day 1*

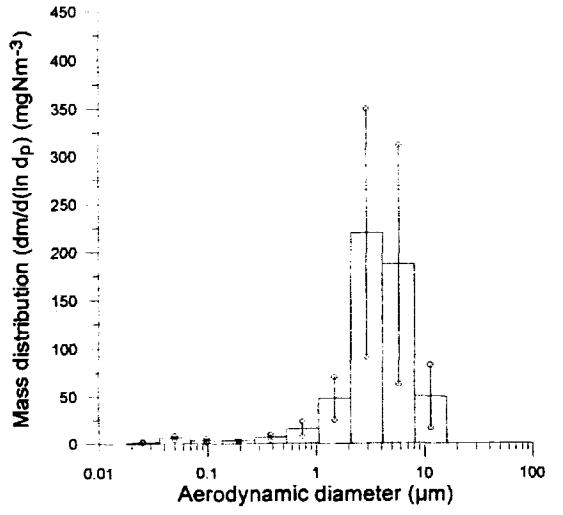

Figure H.25 *Mass distribution of fly ash, all impactor stages. Series 7, day 2*

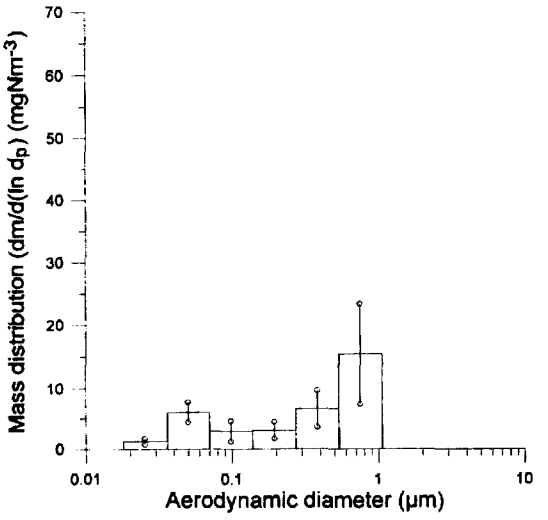

Figure H.26 *Mass distribution of fly ash, impactor stages 1-6. Series 7, day 2*

Series 8

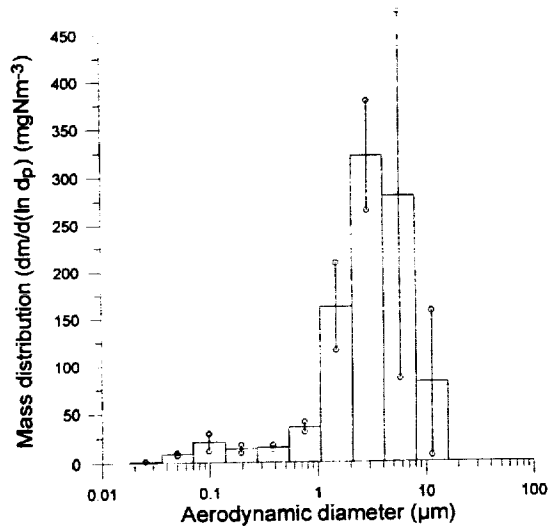

Figure H.27 *Mass distribution of fly ash, all impactor stages. Series 8, day 1*

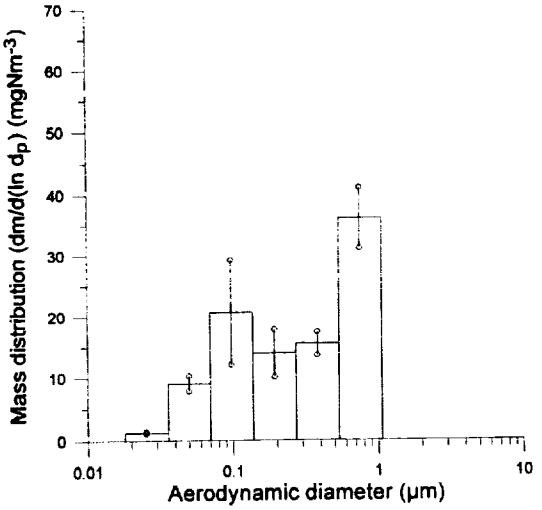

Figure H.28 *Mass distribution of fly ash, impactor stages 1-6. Series 8, day 1*

Series 3a

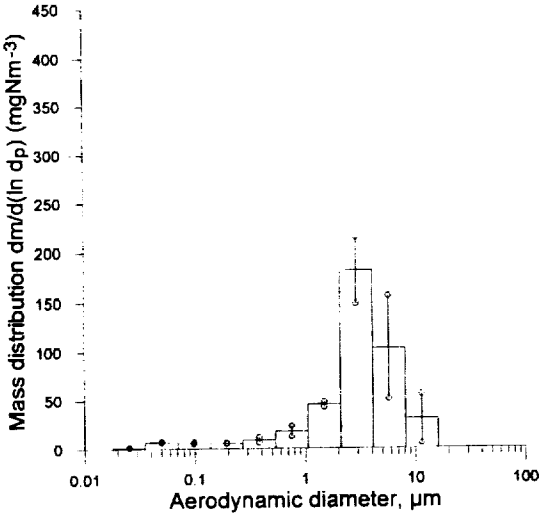

Figure H.29 *Mass distribution of fly ash, all impactor stages. Series 3a, day 1*

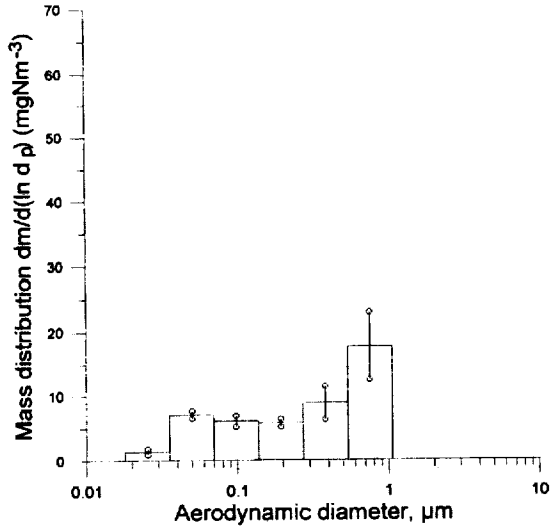

Figure H.30 *Mass distribution of fly ash, impactor stages 1-6. Series 3a, day 1*

Series 8a

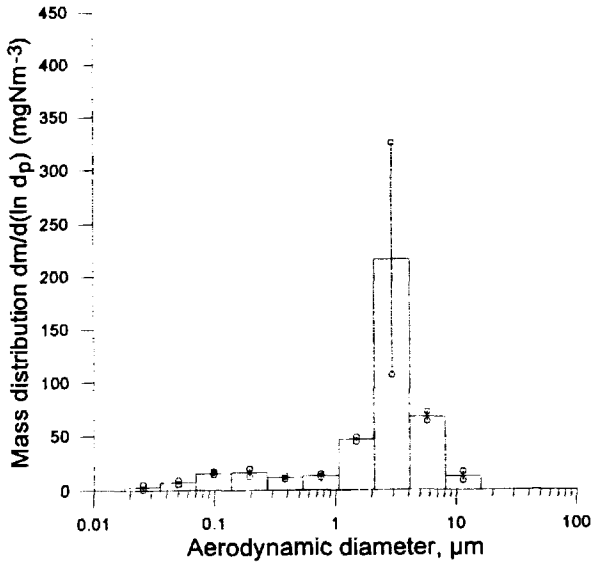

Figure H.31 *Mass distribution of fly ash, all impactor stages. Series 8a*

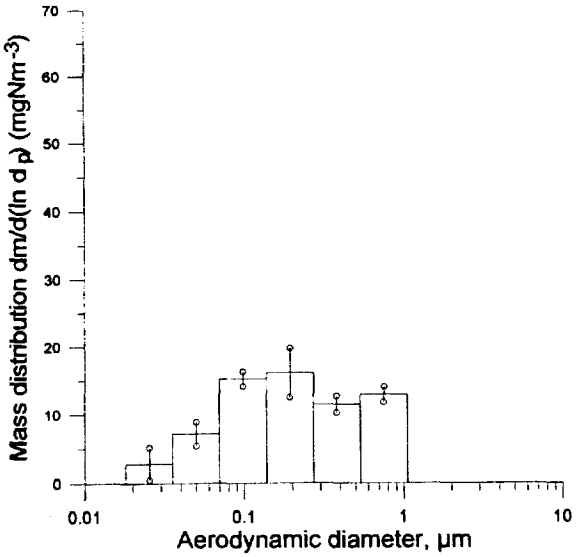

Figure H.32 *Mass distribution of fly ash, impactor stages 1-6. Series 8a*

Series 9a

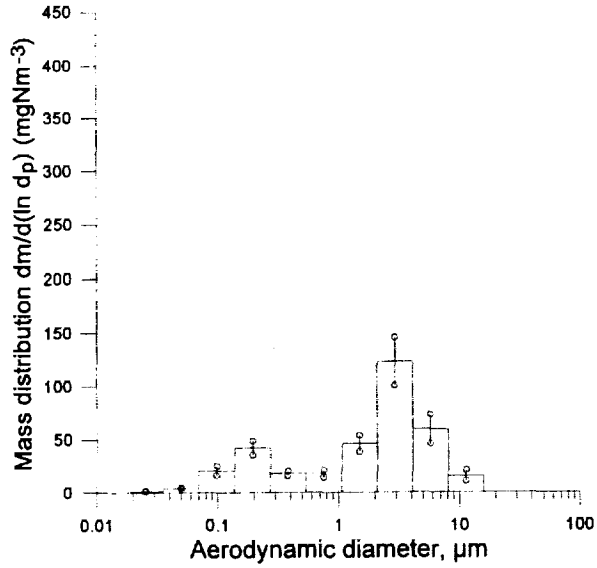

Figure H.33 *Mass distribution of fly ash, all impactor stages. Series 9a*

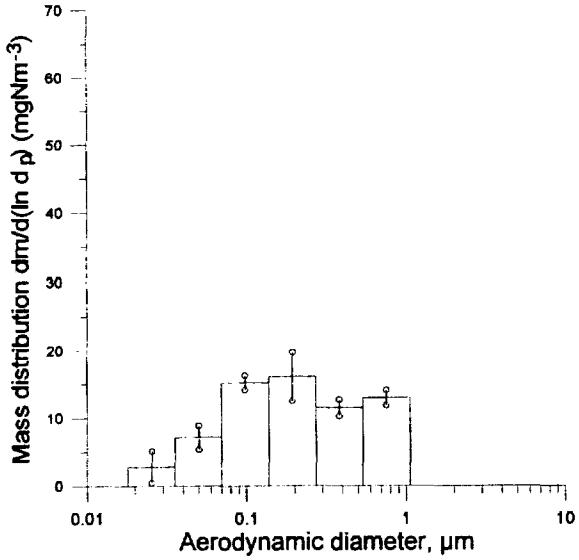

Figure H.34 *Mass distribution of fly ash, impactor stages 1-6. Series 9a*

Appendix I: Results of fly ash EDX-analyses

The composition in all figures and tables of this appendix is calculated as weight percent according to

$$w_i = \frac{m_i}{\sum_j m_j} \cdot 100 \qquad \textbf{(I.1)}$$

where m_j are the masses of all elements identified in the sample. Elements lighter than Na are not detected. Elements in concentrations of less than approximately 0.5 % (w/w) are likewise not detected. Copper foils are used for all series except series 1, where no usable copper foils were obtained. A set of aluminum foils is analyzed for this series, where the aluminum signal is ignored. All diameters listed are aerodynamic diameter corresponding to a particle density of 1 g/cm^3.

Series 1, 50% load, 20% straw.03/21/1996, 11:51-12:20. Set 31. Coal type A

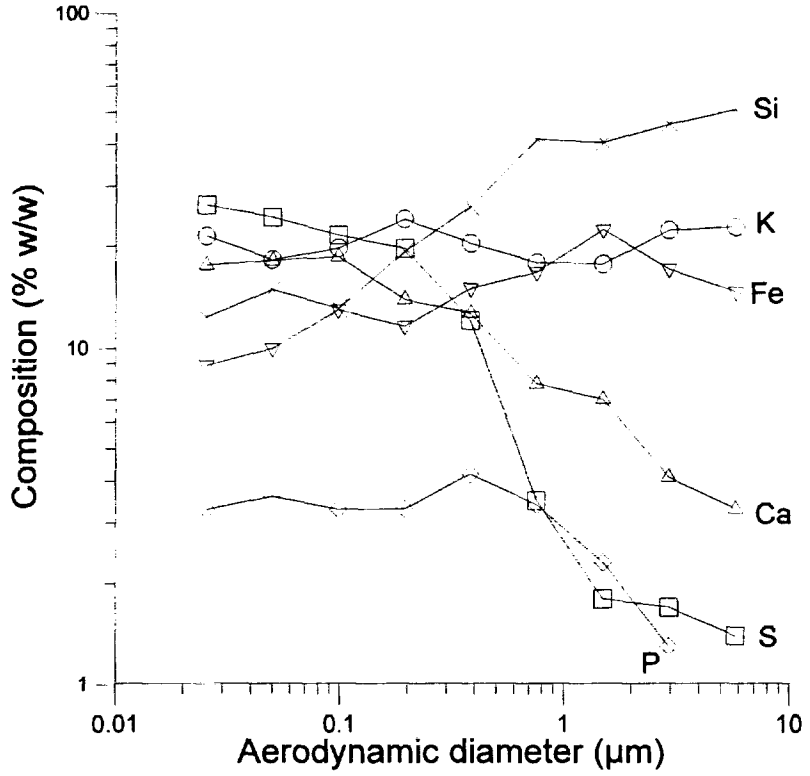

Figure I.1 *EDX-data for series 1, day 2. Coal type A, 50% load, 20% straw. Impactor sample 31. Distribution of main elements in weight % elements detected.*

Table I.1*: Distribution of main elements from EDX analysis. Weight % of elements detected.*

Stage	D_p µm	Na	Mg	Al	Si	P	S	K	Ca	Ba	Ti	V	Fe
1	0.025	0.5	1.0	-	12.4	3.3	26.4	21.4	17.6	7.7	0.2	0.7	8.9
2	0.05	0.4	1.5	-	14.9	3.6	24.3	18.2	18.1	8.3	0.1	0.6	10.0
3	0.1	0.4	1.0	-	13.1	3.3	21.5	19.7	18.6	8.4	0.3	0.7	13.0
4	0.194	0.6	1.5	-	19.2	3.3	19.6	23.9	13.9	5.0	1.1	0.4	11.6
5	0.382	1.0	2.8	-	26.0	4.2	12.1	20.3	12.7	4.3	1.5	0.3	15.0
6	0.75	0.9	4.1	-	41.2	3.4	3.5	17.8	7.8	3.1	1.3	0.4	16.7
7	1.49	0.3	2.8	-	40.3	2.3	1.8	17.6	7.0	3.5	2.0	0.3	22.2
8	2.93	0.5	2.7	-	45.7	1.3	1.7	22.1	4.1	3.4	1.2	0.2	17.0
9	5.8	0.7	2.5	-	50.6	0.8	1.4	22.6	3.3	1.9	1.4	0.3	14.6

Series 2, 75% load, 20% straw. 04/10/1996, 13:20-14:22. Set 28. Coal type A

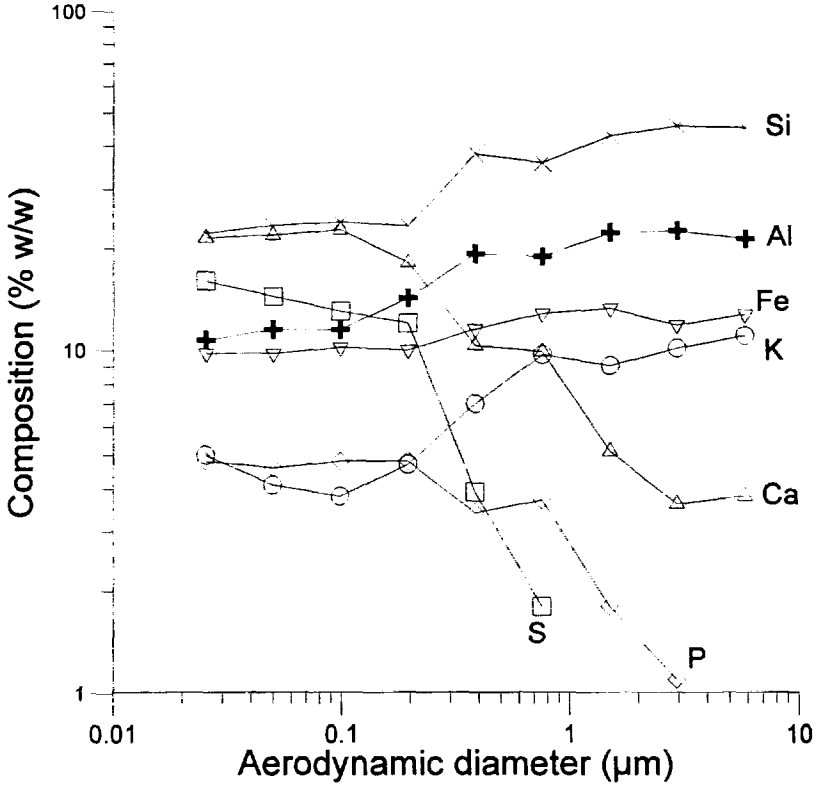

Figure I.2 *EDX-data for series 2, day 1. Coal type A, 75% load, 20% straw. Impactor sample 28. Distribution of main elements in weight % elements detected*

Table I.2*: Distribution of main elements from EDX analysis. Weight % of elements detected.*

Stage	D_p µm	Na	Mg	Al	Si	P	S	K	Ca	Ba	Ti	V	Fe
1	0.025	-	2.2	10.7	22.2	4.8	16.0	5.0	21.5	6.9	0.5	0.5	9.8
2	0.05	-	2.3	11.5	23.4	4.6	14.4	4.1	21.9	6.6	0.8	0.5	9.8
3	0.1	-	2.6	11.5	23.9	4.8	13.0	3.8	22.7	6.2	0.8	0.5	10.2
4	0.194	-	2.6	14.2	23.3	4.8	12.0	4.7	18.1	4.8	1.0	0.5	10.0
5	0.382	-	2.9	19.2	37.7	3.4	3.9	7.0	10.3	3.0	1.1	0.1	11.5
6	0.75	-	2.9	18.9	35.6	3.7	1.8	9.7	9.9	2.6	2.0	0.2	12.8
7	1.49	-	2.4	22.2	42.6	1.8	0.5	9.0	5.1	1.8	1.3	0.1	13.2
8	2.93	-	2.2	22.5	45.4	1.1	0.4	10.1	3.6	1.9	1.0	0.1	11.8
9	5.8	-	1.9	21.3	44.8	0.8	0.8	11.0	3.8	1.4	1.3	0.1	12.7

Series 2, 75% load, 20% straw. 04/11/1996, 10:09-11:07. Set 29. Coal type A

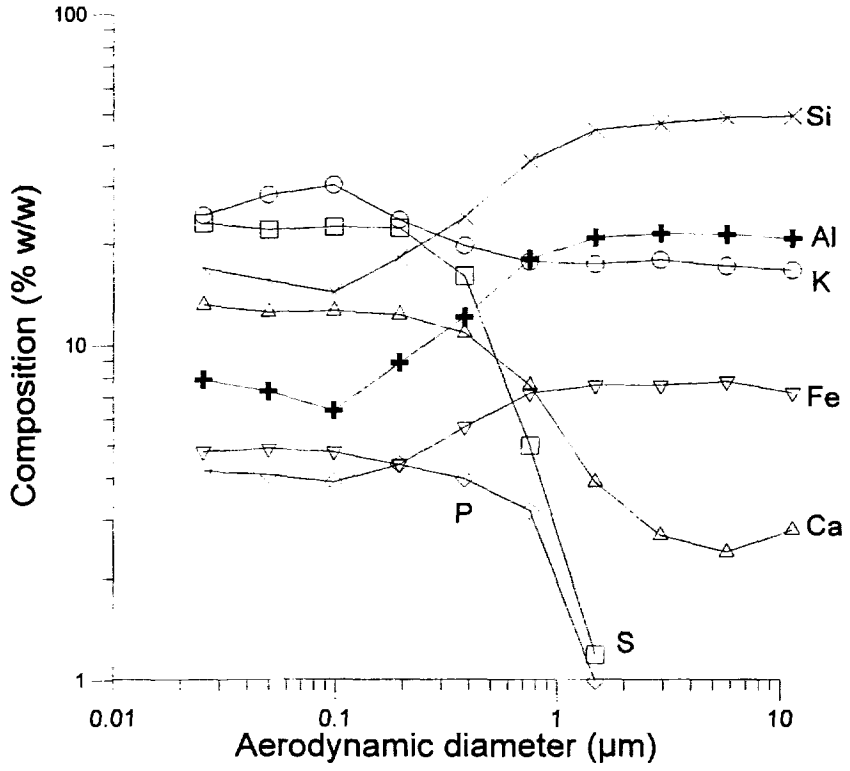

Figure I.3 *EDX-data for series 2, day 2. Coal type A, 75% load, 20% straw. Impactor sample 29. Distribution of main elements in weight % elements detected*

Table I.3*: Distribution of main elements from EDX analysis. Weight % of elements detected.*

Stage	D_p µm	Na	Mg	Al	Si	P	S	K	Ca	Ba	Ti	V	Fe	Cl
1	0.025	1.9	1.4	7.9	16.9	4.2	23.1	24.4	13.1	0.4	1.1	0.3	4.8	0.6
2	0.05	1.7	1.3	7.3	15.5	4.1	22.1	28.2	12.5	0.6	0.8	0.4	4.9	0.9
3	0.1	1.4	1.0	6.4	14.3	3.9	22.5	30.2	12.6	0.0	1.5	0.5	4.8	0.8
4	0.194	1.6	1.4	8.9	18.2	4.4	22.4	23.7	12.3	0.0	1.6	0.3	4.4	0.8
5	0.382	0.9	2.8	12.1	24.2	4.0	16.0	19.8	10.9	0.0	1.5	0.4	5.7	1.8
6	0.75	0.8	2.9	18	35.9	3.2	5.0	17.7	7.6	0.0	1.5	0.2	7.2	0.3
7	1.49	0.2	1.8	20.9	44.7	0.8	1.2	17.4	3.9	0.0	1.4	0.2	7.6	0.0
8	2.93	0.2	1.3	21.5	46.7	0.4	0.4	17.9	2.7	0.0	1.2	0.2	7.6	0.1
9	5.8	0.2	0.9	21.3	48.6	0.0	0.4	17.1	2.4	0.0	1.2	0.2	7.8	0.0
10	11.4	0.3	1.2	20.7	49.1	0.0	0.7	16.6	2.8	0	1.1	0.1	7.2	0.3

Series 3, 100% load, 20% straw. 03/28/1996, 10:08-11:10. Set 27. Coal Type A

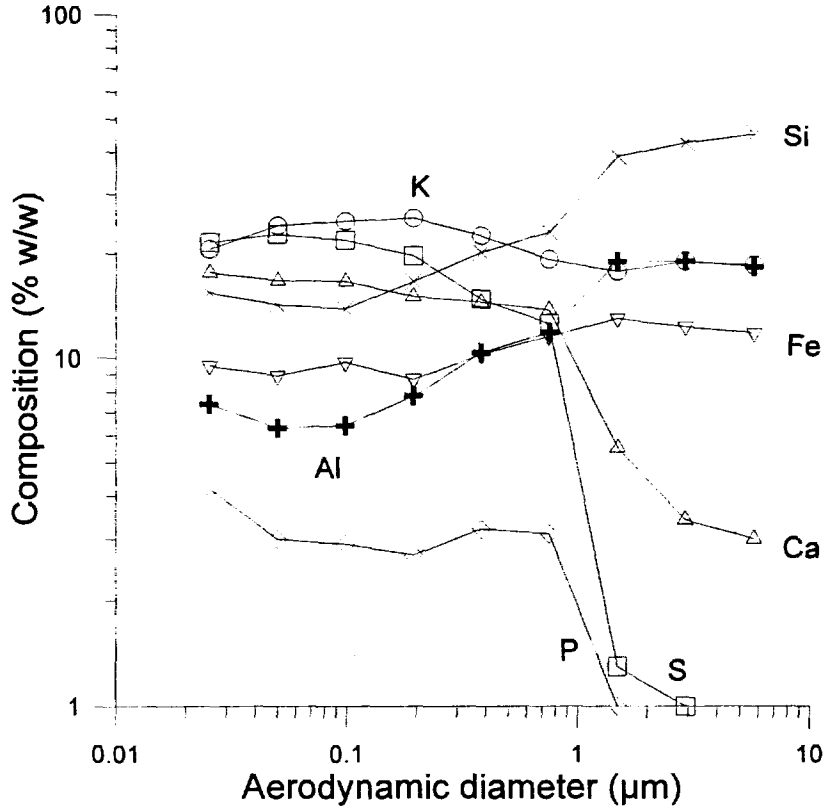

Figure I.4 *EDX-data for series 3, day 2. Coal type A, 100% load, 20% straw. Impactor sample 27. Distribution of main elements in weight % elements detected*

Table I.4*: Distribution of main elements from EDX analysis. Weight % of elements detected.*

Stage	D_p µm	Na	Mg	Al	Si	P	S	K	Ca	Ti	V	Fe
1	0.025	0.6	1.1	7.4	15.4	4.2	21.6	20.6	17.6	1.5	0.5	9.5
2	0.05	1.0	0.7	6.3	14.2	3.0	22.8	24.2	16.7	1.9	0.4	8.9
3	0.1	0.9	0.7	6.4	13.8	2.9	21.9	24.9	16.6	1.7	0.6	9.7
4	0.194	0.7	1.1	7.8	16.6	2.7	19.7	25.4	15	1.7	0.7	8.7
5	0.382	0.6	1.6	10.3	20.1	3.2	14.7	22.5	14.4	2.1	0.4	10.2
6	0.75	0.6	1.7	11.8	23.1	3.1	12.5	19.2	13.7	2.6	0.5	11.5
7	1.49	0.4	1.8	18.9	38.6	1.0	1.3	17.7	5.5	1.9	0	12.9
8	2.93	0.4	1.1	18.9	42.3	0.2	1.0	18.9	3.4	1.6	0	12.2
9	5.8	0.4	0.7	18.2	44.8	0.1	0.9	18.4	3.0	1.8	0	11.7

Series 4, 100% load, 10% straw. 04/18/1996, 09:39-10:37. Set 37. Coal type A

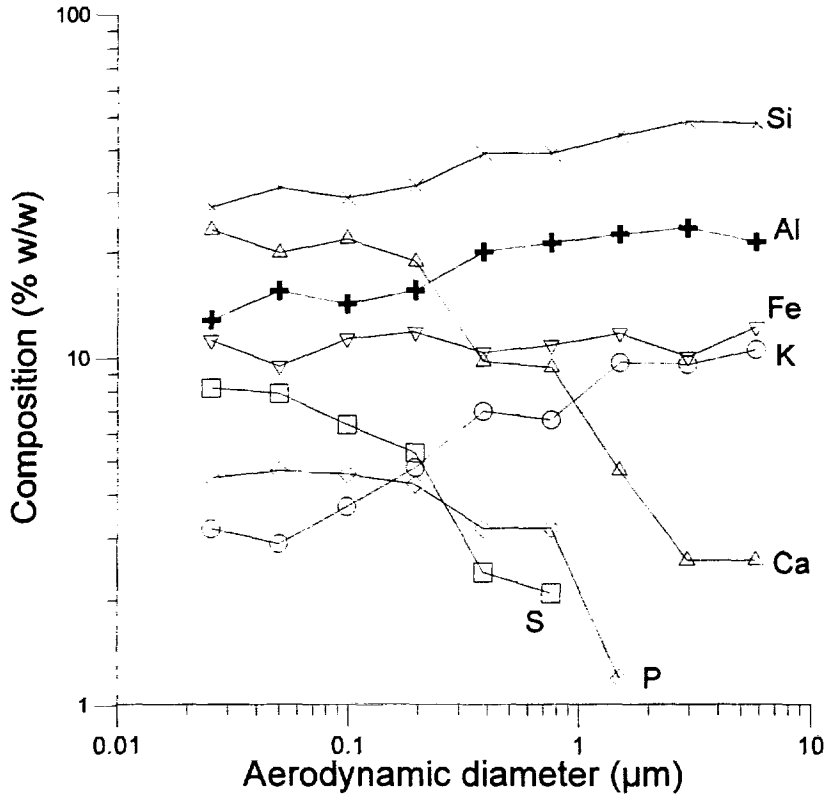

Figure I.5 *EDX-data for series 4, day 2. Coal type A, 100% load, 10% straw. Impactor sample 37. Distribution of main elements in weight % elements detected*

Table I.5: Distribution of main elements from EDX analysis. Weight % of elements detected.

Stage	D_p µm	Na	Mg	Al	Si	P	S	K	Ca	Ba	Ti	V	Fe
1	0.025	0.0	1.4	12.9	27.2	4.5	8.2	3.2	23.3	6.3	1.0	0.7	11.3
2	0.05	0.0	2.1	15.6	31	4.7	7.9	2.9	20.0	5.0	0.8	0.5	9.5
3	0.1	0.0	1.6	14.3	28.9	4.6	6.4	3.7	21.9	5.7	0.9	0.6	11.4
4	0.194	0.0	1.9	15.6	31.3	4.3	5.3	4.8	18.8	4.4	1.4	0.5	11.9
5	0.384	0.4	3.1	20.1	38.9	3.2	2.4	7.0	9.8	3.7	1.0	0.1	10.4
6	0.75	0.3	2.8	21.3	38.9	3.2	2.1	6.6	9.4	3.2	1.4	0.0	10.9
7	1.49	0.1	2.1	22.6	44.0	1.2	0.3	9.7	4.7	1.8	1.6	0.1	11.8
8	2.93	0.1	2.0	23.6	48.4	0.3	0.2	9.6	2.6	1.9	1.0	0.1	10.1
9	5.8	0.2	1.6	21.5	47.8	0.2	0.5	10.6	2.6	1.1	1.4	0.2	12.3

Series 5, 100% load, 0% straw. 04/25/1996, 10:13-11:33. Set 38. Coal type A

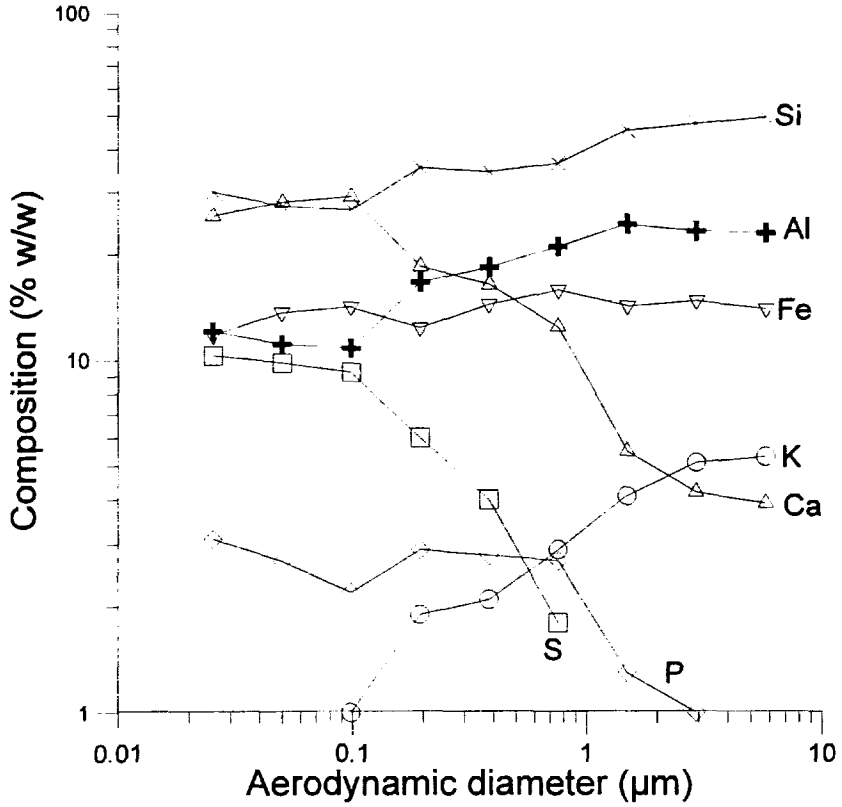

***Figure I.6** EDX-data for series 5, day 2. Coal type A, 100% load, 0% straw. Impactor sample 38. Distribution of main elements in weight % elements detected*

***Table I.6**: Distribution of main elements from EDX analysis. Weight % of elements detected.*

Stage	D_p µm	Na	Mg	Al	Si	P	S	K	Ca	Ba	Ti	Fe
1	0.025	0.0	2.1	12.1	30	3.1	10.3	0.9	25.6	3.1	1.1	11.8
2	0.05	0.0	1.5	11.1	27.3	2.7	9.8	0.9	28.0	3.6	1.5	13.7
3	0.1	0.0	1.5	10.8	26.6	2.2	9.2	1.0	29.0	3.8	1.7	14.2
4	0.194	0.2	2.7	16.7	35.2	2.9	6.0	1.9	18.5	2.9	0.7	12.4
5	0.382	0.2	3.2	18.4	34.2	2.8	4.0	2.1	16.5	3.4	0.8	14.5
6	0.75	0.3	3.2	21.0	36.2	2.7	1.8	2.9	12.5	3.4	0.4	15.9
7	1.49	0.4	2.0	24.2	45.2	1.3	0.4	4.1	5.5	2.4	0.3	14.3
8	2.93	0.0	2.2	23.1	47.2	1.0	0.3	5.1	4.2	1.9	0.3	14.8
9	5.8	0.0	1.9	22.8	49.1	0.6	0.5	5.3	3.9	1.7	0.2	14

Series 6, 75% load, 0% straw. 05/08/1996, 10:38-12:05. Set 41. Coal type A

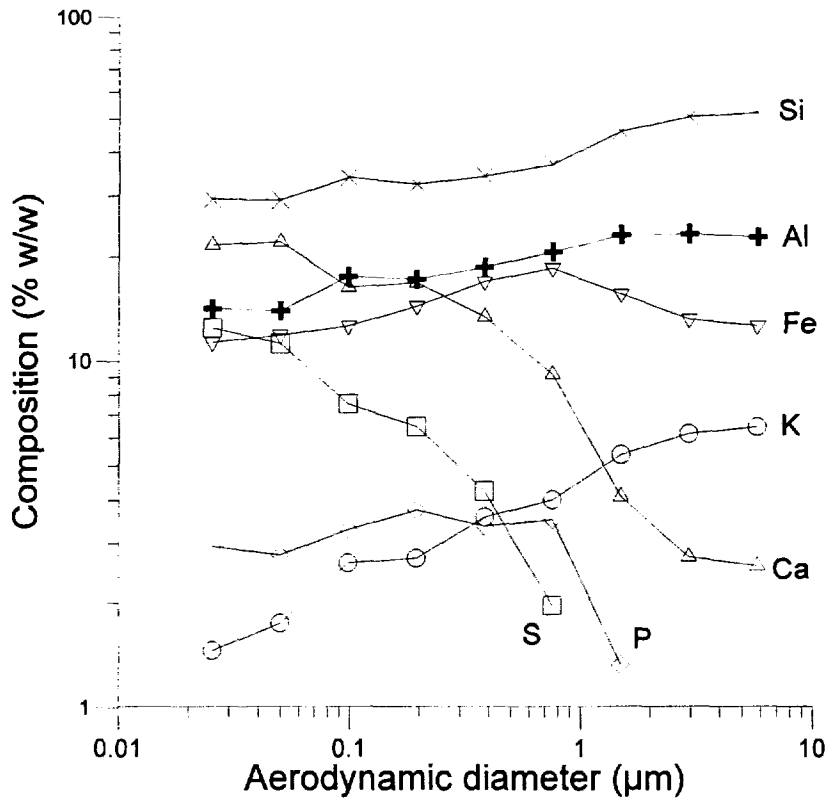

***Figure I.7** EDX-data for series 6, day 1. Coal type A, 75% load, 0% straw. Impactor sample 41. Distribution of main elements in weight % elements detected*

***Table I.7**: Distribution of main elements from EDX analysis. Weight % of elements detected.*

Stage	D_p µm	Mg	Al	Si	P	S	K	Ca	Ti	V	Fe
1	0.0	1.4	14.1	29.3	2.9	12.4	1.5	21.6	3.4	2.0	11.3
2	0.1	1.5	13.9	29.1	2.8	11.2	1.8	22.1	3.7	2.0	11.9
3	0.1	2.0	17.5	33.8	3.3	7.5	2.6	16.3	3.1	1.3	12.6
4	0.2	1.9	17.2	32.3	3.7	6.5	2.7	16.8	3.5	1.2	14.3
5	0.42	1.8	18.6	34.0	3.4	4.2	3.6	13.4	3.2	1.0	16.9
6	0.8	1.9	20.7	36.7	3.5	2.0	4.0	9.1	3.0	0.7	18.5
7	1.5	1.4	23.1	45.9	1.3	0.7	5.4	4.1	2.1	0.4	15.6
8	2.9	1.0	23.3	50.6	0.3	0.7	6.2	2.7	1.8	0.2	13.2
9	5.8	1.0	22.9	51.8	0.0	0.8	6.5	2.6	1.8	0.2	12.6

Series 7, 50% load, 0% straw. 05/01/1996, 11:00-12:30. Set 39. Coal type A

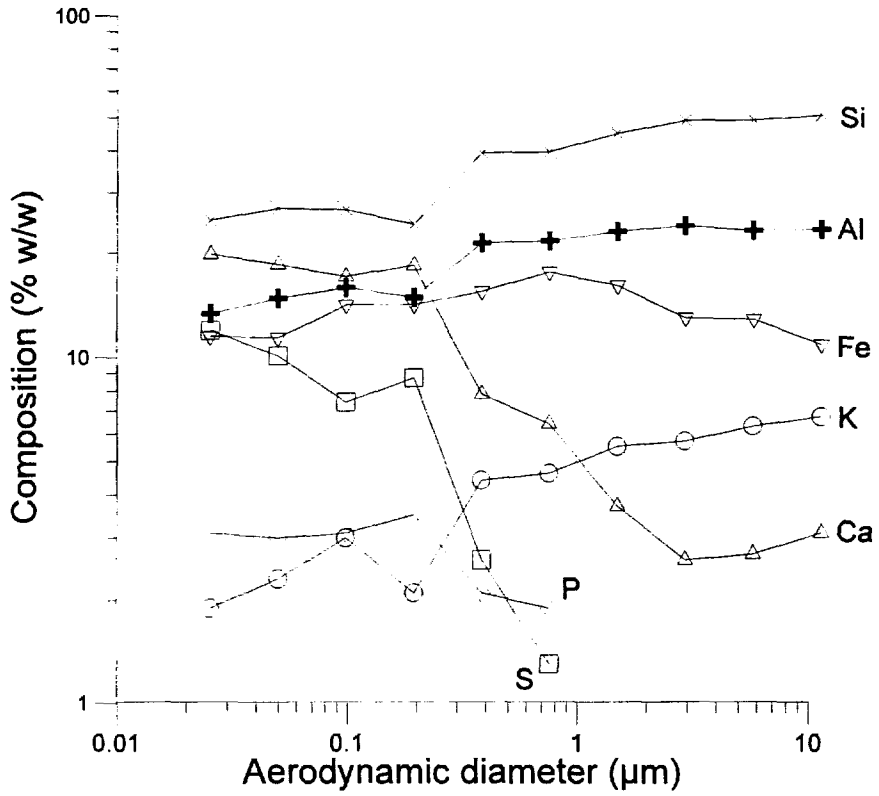

Figure I.8 *EDX-data for series 7, day 1. Coal type A, 50% load, 0% straw. Impactor sample 39. Distribution of main elements in weight % elements detected*

Table I.8*: Distribution of main elements from EDX analysis. Weight % of elements detected.*

Stage	D_p µm	Na	Mg	Al	Si	P	S	K	Ca	Ba	Ti	V	Fe
1	0.025	0.0	2.6	13.4	24.9	3.1	12.0	1.9	19.8	9.1	0.7	1.1	11.5
2	0.05	0.0	2.7	14.8	26.9	3.0	10.1	2.3	18.5	8.7	0.7	1.0	11.4
3	0.1	0.0	2.6	15.9	26.7	3.1	7.4	3.0	17.1	7.6	1.5	0.9	14.2
4	0.194	0.0	3.0	14.9	24.2	3.5	8.7	2.1	18.4	8.7	1.3	0.9	14.2
5	0.382	0.0	2.5	21.3	39.1	2.1	2.6	4.4	7.8	3.1	1.5	0.3	15.5
6	0.75	0.0	2.5	21.6	39.4	1.9	1.3	4.6	6.4	3.0	1.6	0.2	17.6
7	1.49	0.0	2.0	23.0	44.8	0.8	0.8	5.5	3.7	1.3	1.7	0.2	16.1
8	2.93	0.0	2.0	23.9	48.9	0.4	0.6	5.7	2.6	1.9	1.1	0.1	13
9	5.8	0.2	2.0	23.2	49.1	0.3	0.6	6.3	2.7	1.9	0.9	0.0	12.9
10	11.4	0.1	1.8	23.3	50.7	0.2	0.9	6.7	3.1	1.6	0.9	0.0	10.9

Series 8, 70% load, 0% straw. 05/15/1996, 10:24-11:22. Set 43. Coal type B

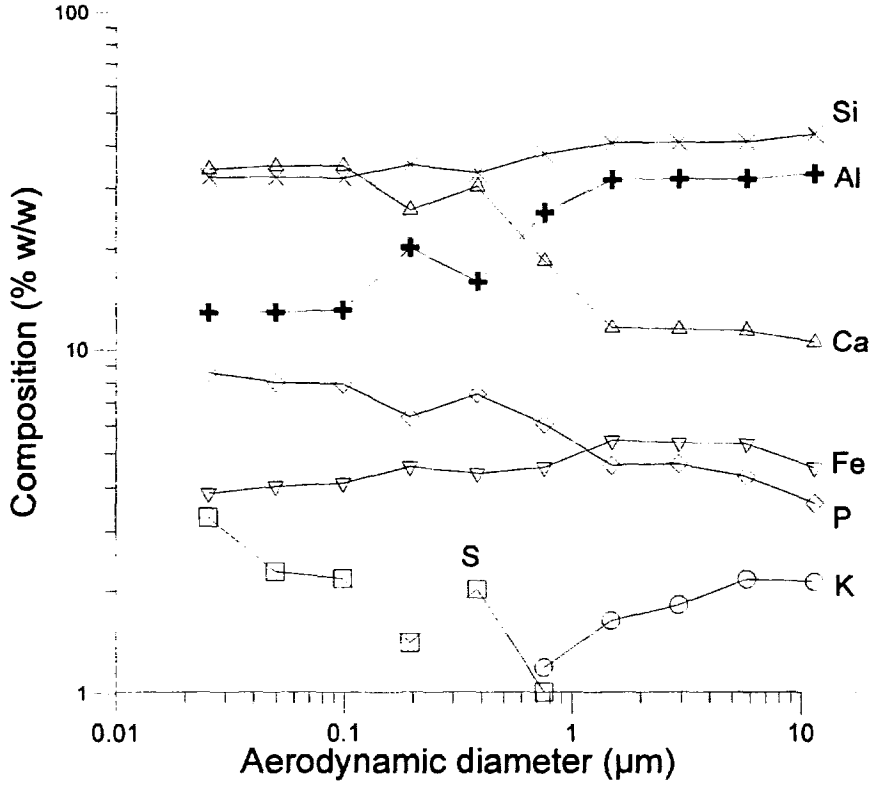

Figure I.9 *EDX-data for series 8, day 1. Coal type B, 70% load, 0% straw. Impactor sample 43. Distribution of main elements in weight % elements detected*

Table I.9*: Distribution of main elements from EDX analysis. Weight % of elements detected.*

Stage	D_p µm	Mg	Al	Si	P	S	K	Ca	Ti	V	Fe
1	0.03	1.9	12.9	32.2	8.6	3.3	0.0	33.9	3.5	0	3.8
2	0.1	1.9	12.9	32.1	8.0	2.3	0.0	34.7	3.6	0.5	4.0
3	0.1	1.7	13.1	31.9	7.9	2.2	0.0	34.6	3.9	0.5	4.1
4	0.2	1.7	20.2	35.1	6.4	1.4	0.8	25.9	3.8	0.3	4.6
5	0.4	1.9	15.9	33.1	7.4	2.0	0.6	30.3	4.1	0.3	4.4
6	0.8	1.7	25.5	37.6	6.1	1.0	1.2	18.4	3.8	0.2	4.6
7	1.5	1.2	31.6	40.6	4.6	0.0	1.6	11.6	3.1	0.3	5.4
8	2.9	1.1	31.8	40.6	4.7	0.0	1.8	11.5	3.2	0.1	5.3
9	5.8	1.0	31.7	40.7	4.3	0.0	2.2	11.4	3.4	0.1	5.3
10	11.4	0.7	32.8	43.0	3.6	0.0	2.1	10.5	2.6	0.2	4.5

Series 3a, 100% load, 20% straw.01/29/1997, 7:46-9:11. Sample S1. Coal type A

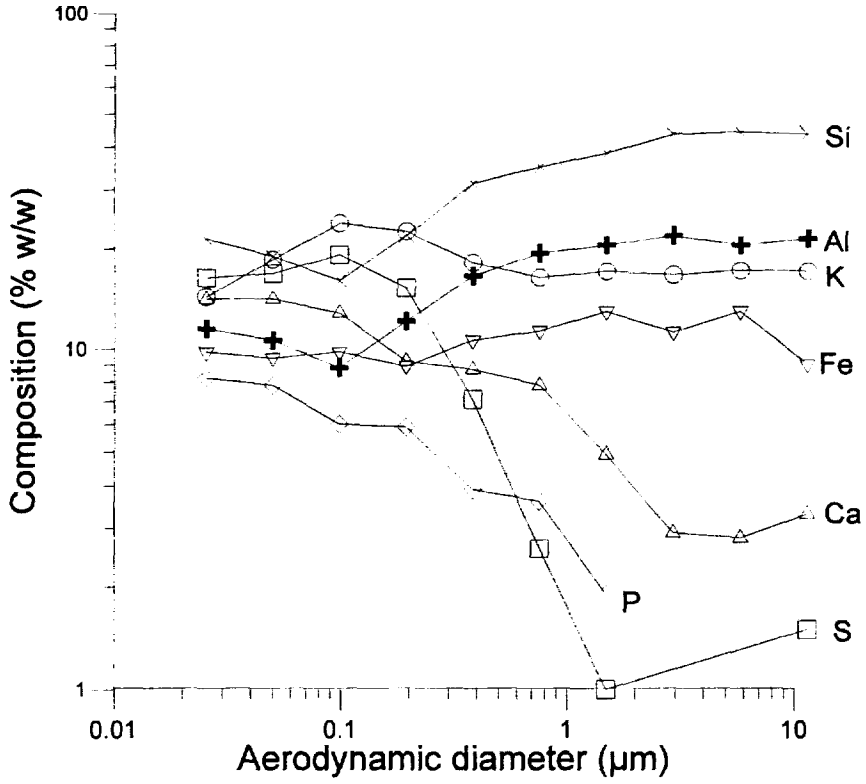

Figure I.10 *EDX-data for series 3a, day 1. Coal type A, 100% load, 20% straw. Impactor sample S1. Distribution of main elements in weight % elements detected*

Table I.10*: Distribution of main elements from EDX analysis. Weight % of elements detected.*

Stage	D_p µm	Na	Mg	Al	Si	P	S	K	Ca	Ba	Ti	V	Fe
1	0.025	0.0	1.3	11.5	21.4	8.2	16.3	14.3	14.1	0	2.1	0.8	9.4
2	0.050	0.2	1.0	10.6	18.9	7.8	16.8	18.5	14.1	0	0.1	0.6	10
3	0.098	0.0	0.5	8.8	16.0	6.0	19.1	23.8	12.8	0	2.3	0.9	9.8
4	0.194	0.6	1.5	12.1	21.9	5.9	15.2	22.5	9.2	0	1.8	0.5	8.9
5	0.382	0	1.2	16.5	31.2	3.9	7.1	18.1	8.7	0	2.2	0.6	10.6
6	0.750	0.1	1.9	19.3	34.8	3.6	2.6	16.3	7.8	0	2.2	0.2	11.3
7	1.49	0.2	1.5	20.4	38.1	1.9	1.0	17.0	4.9	0	2.1	0.0	12.9
8	2.93	0.3	1.5	21.8	43.3	0.7	0.3	16.6	2.9	0	1.5	0.0	11.2
9	5.80	0.0	1.1	20.4	43.7	0.3	0.2	17.1	2.8	0	1.5	0.0	12.9
10	0.0	0.3	21.3	43.2	0.4	1.5	17.0	3.3	3.3	0	4.0	0.1	9.0

Series 8a, 100% load, 0% straw. 02/05/1997, 9:52-11:25.Sample S4. Coal type C

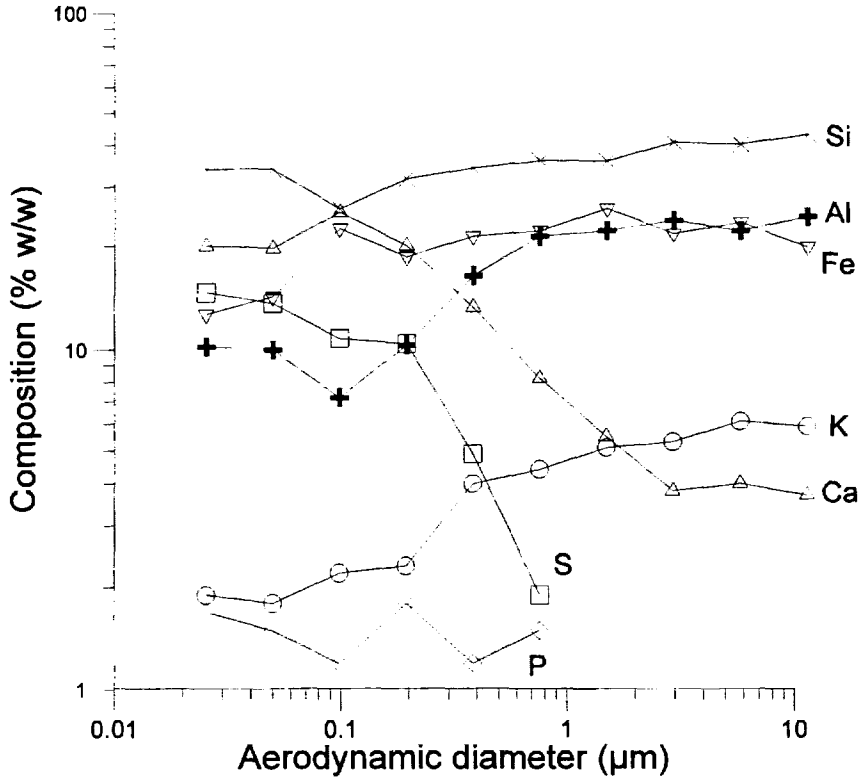

Figure I.11 *EDX-data for series 8a, day 1. Coal type C, 100% load, 0% straw. Impactor sample S4. Distribution of main elements in weight % elements detected*

Table I.11*: Distribution of main elements from EDX analysis. Weight % of elements detected.*

Stage	D_p µm	Na	Mg	Al	Si	P	S	K	Ca	Ba	Ti	V	Fe
1	0.025	0.0	1.9	10.2	33.8	1.7	14.7	1.9	20.0	0	2.3	0.9	12.7
2	0.05	0.0	2.1	10.0	33.8	1.5	13.7	1.8	19.7	0	2.1	1.0	14.3
3	0.1	0.0	1.3	7.2	25.7	1.2	10.8	2.2	25.1	0	3.0	1.1	22.5
4	0.194	0.0	1.7	10.3	31.6	1.8	10.4	2.4	20.0	0	2.4	0.8	18.6
5	0.382	0.0	1.7	16.4	34.0	1.3	4.9	4.0	13.3	0	2.6	0.6	21.3
6	0.75	0.0	2.0	21.3	35.8	1.5	1.9	4.4	8.2	0	2.5	0.3	22.1
7	1.49	0.0	1.7	22.1	35.6	0.9	0.8	5.1	5.5	0	2.4	0.3	25.7
8	2.93	0.0	1.4	23.7	40.6	0.6	0.5	5.4	3.8	0	2.1	0.2	21.7
9	5.8	0.0	1.2	22.1	40.1	0.3	0.4	6.1	4.0	0	2.4	0.2	23.4
10	11.4	0.0	1.1	24.3	42.7	0.0	0.9	5.9	3.7	0	1.6	0.1	19.8

Series 9a, 100%load, 20% straw.02/07/97 11:51-12:20.Sample S13. Coal type C.

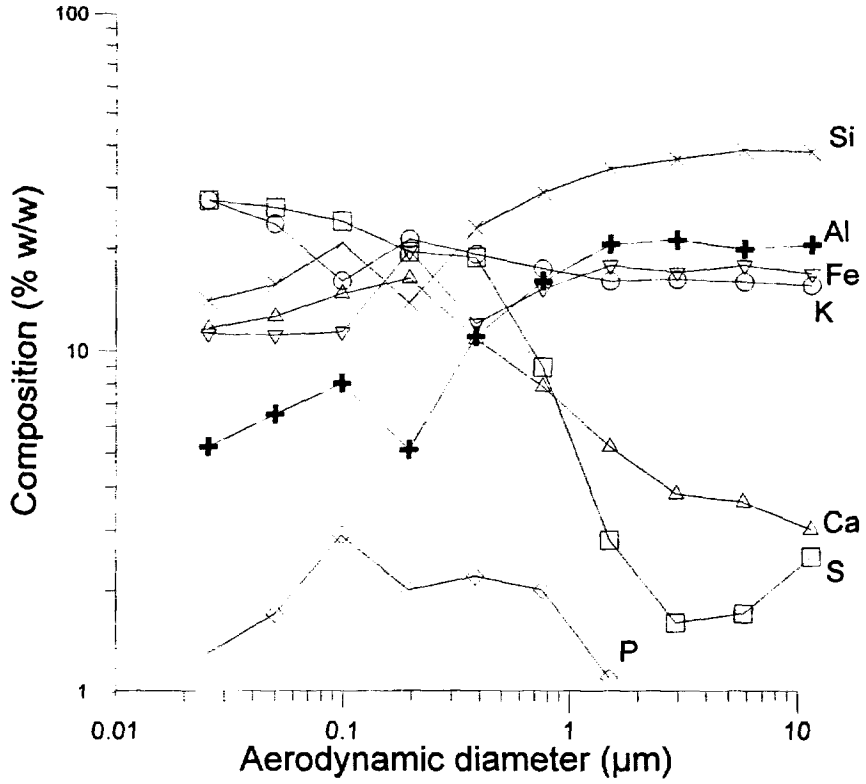

Figure I.12 *EDX-data for series 9a, day 1. Coal type C, 100% load, 20% straw. Impactor sample S13. Distribution of main elements in weight % elements detected*

Table I.12*: Distribution of main elements from EDX analysis. Weight % of elements detected.*

Stage	D_p µm	Na	Mg	Al	Si	P	S	K	Ca	Ba	Ti	V	Fe
1	0.025	0.0	0.0	5.2	14.0	1.3	27.5	27.5	11.6	0	1.2	0.5	11.2
2	0.05	0.0	0.3	6.5	15.7	1.7	26.2	23.5	12.6	0	1.7	0.7	11.1
3	0.1	0.0	0.6	8.0	20.7	2.9	23.9	16.0	14.7	0	1.6	0.4	11.3
4	0.194	0.0	0.2	5.13	13.8	2.0	19.5	21.2	16.3	0	1.8	0.6	19.6
5	0.382	0.0	1.2	11.0	22.9	2.2	18.8	19.2	10.8	0	1.5	0.4	12.0
6	0.75	0.0	1.3	16.0	28.9	2.0	8.9	17.4	7.8	0	0.5	15.2	22.1
7	1.49	0.0	0.7	20.5	34.0	1.1	2.8	16.0	5.2	0	2.1	0.0	17.8
8	2.93	0.6	0.9	21.1	36.3	0.7	1.6	16.2	3.8	0	1.8	0.0	17.0
9	5.8	0.0	0.5	19.8	38.5	0.2	1.7	15.9	3.6	0	2.0	0.0	17.8
10	11.4	0.9	1.0	20.4	38.1	0.3	2.5	15.5	3.0	0	1.4	0.0	16.8